

COMPUTING WITH HYBRID MATERIAL OSCILLATORS

by

Yan Fang

B.S. in IC Design and Integrated System, Xidian University, 2010

M.S. in Electrical Engineering, University of Pittsburgh, 2013

Submitted to the Graduate Faculty of
Swanson School of Engineering in partial fulfillment
of the requirements for the degree of
Doctor of Philosophy in Electrical Engineering

University of Pittsburgh

2018

UNIVERSITY OF PITTSBURGH
SWANSON SCHOOL OF ENGINEERING

This dissertation was presented

by

Yan Fang

It was defended on

May 24, 2018

and approved by

Anna C. Balazs, PhD, Professor, Department of Chemical and Petroleum Engineering

Kartik Mohanram, PhD, Associate Professor, Department of Electrical and Computer Engineering

Zhi-Hong Mao, PhD, Professor, Department of Electrical and Computer Engineering

Donald M. Chiarulli, PhD, Professor, Department of Computer Science

Samuel J. Dickerson, PhD, Assistant Professor, Department of Electrical and Computer Engineering

Copyright © by Yan Fang

2018

In Memory of
Prof. Steven P. Levitan

COMPUTING WITH HYBRID MATERIAL OSCILLATORS

Yan Fang, PhD

University of Pittsburgh, 2018

The evolution of computers is driven by advances not only in computer science, but also in materials science. As the post-CMOS era approaches, research is increasingly focusing on flexible and unconventional computing systems, including the study of systems that incorporate new computational paradigms into the materials, enabling the computer and the material to be the same entity.

In this dissertation, we design a coupled oscillator system based on a new hybrid material that can autonomously transduce chemical, mechanical, and electrical energy. Each material unit in this system integrates a self-oscillating gel, which undergoes the Belousov-Zhabotinsky (BZ) reaction, with an overlaying piezoelectric (PZ) cantilever. The chemo-mechanical oscillations of the BZ gels deflect the piezoelectric layer, which consequently generates a voltage across the material. When these BZ-PZ units are connected in series by electrical wires, the oscillations of these coupled units become synchronized across the network, with the mode of synchronization depending on the polarity of the piezoelectric. Taking advantage of this synchronization behavior, we demonstrate that the network of coupled BZ-PZ oscillators can perform specific computational tasks such as pattern matching in a self-organized manner, without external electrical power sources. The results of the computational modeling show that the convergence time for stable synchronization gives a distance measure between the “stored” and “input”

patterns, which are encoded by the connection and phases of BZ-PZ oscillators. In addition, we demonstrate two methods to enrich the information representation in our system. One is to employ multiple BZ-PZ oscillator networks in parallel and to process information encoded in different channels. The other is to introduce capacitors into a BZ-PZ network that modify the dynamical behavior of the systems and increase the information storage. We analyze and simulate the proposed coupled oscillator systems by using linear stability analysis and phase models and explore their potential computational capabilities. Through these studies, we establish experimentally realizable design rules for creating “materials that compute”.

TABLE OF CONTENTS

1.0	INTRODUCTION.....	1
1.1	MOTIVATION	1
1.2	PROBLEM STATEMENT	3
1.3	RESEARCH CONTRIBUTIONS	4
1.4	DISSERTATION ORGANIZATION.....	6
2.0	BACKGROUND	7
2.1	OSCILLATOR BASED COMPUTING.....	7
2.1.1	Oscillator Neural Network.....	9
2.1.2	Pattern Matching.....	11
2.2	CHEMICAL MATERIAL OSCILLATORS.....	16
2.2.1	Belousov–Zhabotinsky Reaction	16
2.2.2	BZ Oscillating Gel	17
2.3	DISCUSSION.....	19
3.0	PHASE MODELS FOR COUPLED OSCILLATORS	20
3.1	MATHEMATIC MODEL	20
3.1.1	PPV Model.....	21
3.1.2	Izhikevich’s Model.....	22
3.1.3	Combined Simplified Model.....	24

3.1.4	Oscillator Examples.....	25
3.2	EXPERIMENTS AND SIMULATION	29
3.2.1	Oscillator Behavior Analysis	30
3.2.2	Performance Speedup	34
3.2.3	System Level Simulation	36
3.3	DISCUSSION.....	41
4.0	PATTERN RECOGNITION WITH BZ-PZ OSCILLATORS	42
4.1	THEORETICAL MODEL OF BZ-PZ OSCILLATOR NETWORK	42
4.1.1	Overview.....	42
4.1.2	Model Description.....	44
4.1.3	Phase Dynamics	49
4.2	SYSTEM CONFIGURATION FOR PATTERN RECOGNITION	51
4.3	PERFORMANCE AND ROBUSTNESS.....	56
4.3.1	Distance Metric and Convergence Time	57
4.3.2	Cross-Pattern Test.....	60
4.3.3	Recognition Performance Under Noise	63
4.3.4	Effect of Gel Heterogeneities on Synchronization	66
4.4	SYNCHRONIZATION MODE STABILITY.....	69
4.5	MATERIALS AND FEASIBILITY.....	73
4.5.1	BZ Gel Parameters	73
4.5.2	Piezoelectric Cantilever Parameters	74
4.5.3	Feasibility of System Fabrication	75
4.6	DISCUSSION.....	75

5.0	MULTIPLE BZ-PZ NETWORKS IN PARALLEL	77
5.1	MULTI-CHANNEL BZ-PZ NETWORKS	78
5.2	DETECTING DEFECTS IN QR CODE.....	84
5.3	DISCUSSION.....	87
6.0	BZ-PZ OSCILLATOR NETWORK WITH CAPACITORS	89
6.1	MODIFIED PHASE MODEL	92
6.2	THEORETICAL ANALYSIS	96
6.2.1	Stability Analysis	99
6.2.2	Synchronization in the Three-group Networks	102
6.2.3	Co-existence of Three-group Synchronization Modes	106
6.2.4	The Rate of Synchronization	109
6.2.5	States of Partial Synchronization.....	113
6.3	PATTERN RECOGNITION.....	117
6.3.1	Pattern Matching Experiments on Grayscale Images.....	117
6.3.2	Pattern Recognition Test on COIL Dataset	122
6.4	DISCUSSION.....	128
7.0	CONCLUSION AND FUTURE WORK	130
7.1	SUMMARY	130
7.2	CONCLUSIONS	132
7.3	FUTURE WORK.....	134
	BIBLIOGRAPHY	136

LIST OF TABLES

Table 3.1 RMSE of simulations based on different methods	35
Table 5.1 Channel Representation of Color.....	78
Table 6.1 Configuration and Representation of Different Groups of BZ-PZ units	118

LIST OF FIGURES

Figure 2.1 Oscillatory Neural Network Structure	10
Figure 2.2 Associative Memory Model for Handwritten Digits	11
Figure 2.3 Coupled oscillator based associative memory module.....	12
Figure 2.4 Coupled oscillator system. (a) Voltage controlled ring oscillator; (b) Oscillators coupled together through one common node with DoM detection circuit; (c) Simulation of a three-oscillator cluster by sweeping one frequency, the scatter plot of 1-DoM is against the curve fit of a quadratic model.	15
Figure 2.5 Pattern formed by the concentric waves in BZ reaction (Source: Flickr; Photo by Stephen Morris; Chemistry by Michael Rogers).....	16
Figure 3.1 Ring oscillator model. (a) Simple schematic model; (b) Output waveform and (PPV) at node v3.	27
Figure 3.2 Malkin's approach for PRC. (x-axis: phase, y-axis: amplitude) and output waveform at node v3 and PRC obtained from backwards integral.	28
Figure 3.3 Winfree's approach for PRC, (a) Stimuli Amplitude=0.1, PRC Amplitude=0.2; (b) Stimuli Amplitude=0.05, PRC Amplitude=0.1.....	29
Figure 3.4 Comparing simulations of three coupled oscillators with natural frequencies $\lambda = [1.0, 0.95, 1.05]$, $\varepsilon=0.4$ and 0.2 . (a) Wrapped phase waveform of final stage; (b) Evolution of phase differences between oscillators.	30
Figure 3.5 Degree of synchronization as inverted Euclidean distance, initial frequencies for a range $\lambda_{2,3}=[0.8 \text{ to } 1.2]$ and a fixed frequency of $\lambda_1=1.0$, Left column: $\varepsilon=0.4$, Right column: $\varepsilon=0.2$; Row 1: Winfree's approach, Row 2: Malkin's approach, Row 3: Analytical PPV, Row 4: Direct simulation with oscillator equations.	33
Figure 3.6 Simulations of different numbers of coupled oscillators. All oscillators but two are kept at frequency 1, while the last two are swept.....	34
Figure 3.7 Speed-up (factor) of simplified phase model over direct simulation for different PPV/PRC methods.	36

Figure 3.8 Pattern matching simulation for handwritten digit recognition and DoM from oscillator clusters.....	37
Figure 3.9 (a) Test image with four regions; (b) Segmentation results of each region from oscillator network. Each sub square is the original image with segmented region labeled as white pixels.....	39
Figure 3.10 Using 5x5 Gabor filter to filter the “Car” image. (a) Test image; (b) Gabor filter bank; (c) Results from Oscillator Cluster; (d) Results from digital 2-D convolution.	40
Figure 4.1 Two BZ-PZ oscillator units connected with electrical wires. Each piezoelectric cantilever consists of two identical layers of a polarized piezoelectric material; the internal and external surfaces are covered with thin electrodes connected in parallel. Periodic volumetric changes in the self-oscillating BZ gels cause rhythmic bending of the piezoelectric plates. The vector of polarization in piezoelectric bending plates is oriented perpendicular to the plate surface (not shown). The colors orange and blue are used to distinguish the two parts of a bimorph piezoelectric plate. The red and black solid lines show the electric wires connected to the external and internal electrodes, respectively. The green-colored cubes depict the BZ gels.....	42
Figure 4.2 Multiple BZ-PZ oscillator units connected in serial (left) and parallel (right). $\varepsilon_1, \varepsilon_2, \dots, \varepsilon_n$ are the force polarities of the n connected units. The orange and blue rectangles depict the two layers of a bimorph PZ plate. The green rectangles depict the self-oscillating BZ gels. The red and black lines show the electrical connections to the respective external and internal electrodes in the PZ plates.....	44
Figure 4.3 The connection function $H(\theta)$ used in the equations of the phase dynamics, (4-8,9). The connection function is periodic at $\theta \in [0,1]$	50
Figure 4.4 Schematics indicating how to transpose a black and white image onto the serially connected network of the BZ-PZ oscillators. Here, we store a binary image of the digit ‘0’ that contains 60 pixels. The force polarity of an oscillator is set to +1 for a white pixel and to -1 for a black pixel. Note that assigning $\varepsilon_3 = -1$ is achieved through flipping the red and black connector wires.	52
Figure 4.5 Illustration of the pattern recognition task. The three different BZ-PZ oscillator networks, which store the respective images for the digits ‘0’, ‘1’, and ‘2’, are initialized with the same distorted ‘1’ input image. The phase differences of the oscillations in the networks converge to the respective stored patterns in the course of synchronization. The blue and red lines distinguish between the two groups of oscillators that converge to the phase difference of 0 and 0.5, respectively. The convergence is the fastest in the network exhibiting the best match between the input and stored pattern, i.e., in the network that stores the digit ‘1’.	55
Figure 4.6 The stored 10x10 pattern and an example of the input pattern set used in Test 1. The set is generated by flipping an increasing number of pixels until the input pattern is	

transformed into the mirror pattern. The difference between the stored pattern and an image from the set is characterized by the Hamming distance, which is the sum of the element-wise differences between two binary vectors.	58
Figure 4.7 The average convergence time obtained in Test 1 (blue line), and the Hamming distance between the stored and input images (orange line) as functions of the number of flipped bits. The error bars show the range of convergence times obtained from 100 runs at a given number of flipped bits, which were selected at random from all the bits in the system.	59
Figure 4.8 An example of the 10×10 stored and input patterns used in Test 2. The input patterns are generated using the same strategy of flipping bits as in Test 1.	60
Figure 4.9 The average times of convergence to the stored patterns p_1 (blue line) and p_2 (orange line) obtained in Test 2 as functions of the number of flipped bits. The error bars are obtained as described in Figure 4.7.	61
Figure 4.10 The average times of convergence to the stored patterns p_1 (blue line) and p_2 (orange line) obtained in Test 2 as functions of the number of flipped bits. The two stored patterns are more similar to each other's mirror patterns than the stored patterns in Figure 4.8. The observed peaks are similar to the one in Figure 4.6, the result of Test 1.	63
Figure 4.11 The images used in Test 3. The top row (a) shows the 10×6 binary images of the ten digits used as the stored patterns. Rows (b) and (c) show the respective distorted image of the digit '3' and '8' that are obtained by flipping 1, 5, 10, 15, 20, 25, 30 pixels that are randomly selected.	64
Figure 4.12 The accuracies of the recognition Test 3 for the input patterns of all the digits that are distorted with various levels of noise. The bars are colored according to the noise level. The horizontal axis indicates the input patterns.	65
Figure 4.13 The difference between the average convergence times of the winner and of the runner-up in all the hit cases in Test 3 for the digits shown in Figure 4.12. The error bars show the standard deviation obtained for each bar. The results indicate how fast the correct, recognized winner leads the runner-up. The other notations are the same as in Figure 4.12.	66
Figure 4.14 The phase dynamics for the uniform distribution $\Delta T / T_0 \in [-\sigma, \sigma]$ for various values of σ	68
Figure 4.15 The convergence time at random $\Delta T / T_0 \in [-\sigma, \sigma]$ as a function of the distribution width σ . The convergence threshold is 0.1.	69
Figure 4.16 The phase difference ψ between the two groups of oscillators obtained by numerical solution of (4-15) at $n=46$	71

- Figure 5.1 Schematics of the four BZ-PZ networks used for recognition of colored patterns. After decomposition of input image, the networks perform simultaneous matching operations in the corresponding information channels. The convergence time (given in number in cycles) is determined for each channel separately. 77
- Figure 5.2 Pattern matching in color channels with multiple BZ-PZ networks. The first row shows the colored “smiley face” as the stored pattern, and its decomposed binary pattern images in the B/W, Red, Green and Blue channels, respectively. The second and third rows present the two test input patterns with different types of image variation, and their decomposed patterns in each channel. On the bottom of each row, the convergence time for each channel is shown. 79
- Figure 5.3 Pattern matching with varying input patterns. (a) Nine color image patterns show the process of turn green “left eye” into blue pixel by pixel. The first one is the stored pattern, and the rest eight patterns are the input patterns; (b) Similar test with the process that remove “left eye” object. We plot convergence time in each channel as a function of the number of changed pixels. (c) Convergence time in Blue channel in test (a). (d) Convergence time in B/W channel in test (b). (e) Convergence times in Green channel for both test (a) and (b). Note that the green channel responds in exactly the same manner to test (a) and (b), resulting in the same plot of the convergence time (e). 83
- Figure 5.4 Pattern matching of QR code in multiple color channel. The black/white binary QR code pattern of “Hello World” and randomly colored version as stored pattern are shown in black frame. An example of test input patterns with 10 defect pixels (marked with “x”) are placed on the top right. The bar graph on the bottom gives the averaged convergence time of the repeated simulation of matching operations. The error bars give the maximum and minimum. Each input pattern is labeled at x-axis according to its number of defect pixels, with the three color bars corresponding to convergence time in RGB channels. Note that B/W channel detects no channel in this test and its convergence time is 0, which is not shown. 86
- Figure 6.1 Schematics of the BZ-PZ oscillator network with capacitors connected to each unit. 91
- Figure 6.2 Connect Function and its derivative; (a) The connection function $H(\theta)$ in phase model of BZ-PZ oscillator networks, Eq. (6-7). The function is periodic at $\theta \in [0,1]$. (b) The plot of the derivative of $H(\theta)$ in one period. 95
- Figure 6.3 The evolution of phase differences between all the BZ-PZ units and the first reference unit, initialized with random phases. The legends of plot show the colors that represent different group of units with corresponding parameters (a) original BZ-PZ network with no capacitors; (b)-(d) BZ-PZ networks consist of multiple groups of units with different capacitance. 97
- Figure 6.4 Plots of final stable state ψ_1 and ψ_2 against C_2 at $n_2 = 10, 30$, and 50 represented in colors shown in plot legend. (a)(b): fixed $n_1 = 25$ (c)(d): $n_1 = 50 - n_2$. The filled

disk marks denote the stable state values obtained by the numerical simulations using the phase model, Eq. (6-11). The circle marks at the end of each curve indicate the boundary of the synchronization domain. 103

Figure 6.5 Solutions of Eq. (6-9) and (6-10) plotted as the respective blue- and red-colored lines in coordinates ψ_1 and ψ_2 at $\{n_\alpha\} = \{25, 25, 50\}$, $\{\varepsilon_\alpha\} = \{+1, +1, -1\}$, and (a) $C_2 = 1$ and (b) $C_2 = 10$. The streamlines are displayed in grey. At point $\{\psi_1, \psi_2\}$, the streamline shows direction of the vector $\{\Phi_1(\psi_1, \psi_2), \Phi_2(\psi_1, \psi_2)\}$, where Φ_1 and Φ_2 are the left-hand-sides of Eqs. (6-9) and (6-10), respectively. 106

Figure 6.6 The two co-existing stable modes of synchronization in the three-group system with the number of the BZ-PZ units containing the capacitors (a) $n_2 = 1$, (b) $n_2 = 10$, and (c) $n_2 = 25$. The first mode (solid lines) is typically found when Eq. (6-8) is solved under random initial conditions. The second mode (dashed lines) is found when the initial conditions for Eq. (6-8) are chosen in the vicinity of the synchronization state Figure 6.7. 108

Figure 6.7 Evolution of the three-group system towards the second mode of synchronization as obtained by solving Eq. (6-8) with the initial conditions corresponding to the synchronization state perturbed by adding a random phase shift within $[-0.1, 0.1]$. As in Figure 6.6, the number of the BZ-PZ units containing the capacitors (a) $n_2 = 1$, (b) $n_2 = 10$, and (c) $n_2 = 25$ 108

Figure 6.8 The relaxation times T_k , $k = 1, 2, \dots, 5$, as functions of the capacitance C_2 for the three-group networks with the number of BZ-PZ units containing the capacitors (a) $n_2 = 1$, (b) $n_2 = 10$, and (c) $n_2 = 25$. The solid and dashed lines mark the two modes of synchronization. The line colors label the relaxation modes: $\{T_k\} = \{\text{cyan, red, blue, green, magenta}\}$ 110

Figure 6.9 The times of synchronization as functions of C_2 obtained by simulations of the three-group networks with the configuration (a) $\{n_\alpha\} = \{25, n_2, 50\}$, (b) $\{n_\alpha\} = \{50 - n_2, n_2, 50\}$. In all cases, $\{\varepsilon_\alpha\} = \{+1, +1, -1\}$, $\{C_\alpha\} = \{0, C_2, 0\}$. (c) and (d): The normalized relaxation times (lines) and synchronization times (symbols) for the same network configurations as in (a) and (b), respectively. 111

Figure 6.10 The two types of partial synchronization behaviors observed in the numerical simulations of the network with configuration $\{n_\alpha\} = \{25, 25, 50\}$, $\{\varepsilon_\alpha\} = \{+1, +1, -1\}$, and $\{C_\alpha\} = \{0, 10, 0\}$. In (a) and (b), all phases are plotted relative to the unit 1, $\varphi_i(t) - \varphi_1(t)$. In (c) and (d), all phases are plotted relative to the unit 26, $\varphi_i(t) - \varphi_{26}(t)$ 115

Figure 6.11 The state of partial synchronization observed in the numerical simulations of the network with configuration $\{n_\alpha\} = \{25, 25, 50\}$, $\{\varepsilon_\alpha\} = \{+1, +1, -1\}$, and $\{C_\alpha\} = \{0, 10, 0\}$. In (a) and (b), all phases are plotted relative to the unit 1, $\varphi_i(t) - \varphi_1(t)$. In (c) and (d), all phases are plotted relative to the unit 26, $\varphi_i(t) - \varphi_{26}(t)$	116
Figure 6.12 Matching operation of grayscale image pattern by using a BZ-PZ network with capacitors.....	119
Figure 6.13 Average convergence time of the BZ-PZ network that perform pattern matching on the distorted black/white image pattern with extra gray pixels.....	120
Figure 6.14 Average convergence time of the BZ-PZ network that perform pattern matching on the distorted gray image pattern with extra black white pixels.....	121
Figure 6.15 Images of objects selected from COIL dataset. (a) Ten object categories; (b) Example images of one object. The grayscale images are pictures taken after every 5-degree rotation. Each object has 72 pictures.....	123
Figure 6.16 The preprocessing stages for pattern storage.....	124
Figure 6.17 The convergence time matrices of pattern matching on COIL dataset.	125
Figure 6.18 The convergence time matrices of pattern matching on COIL dataset with object rotation. Objects are rotated in the input patterns for (a) 15°, (b) 25°, (c) 50° respectively.....	127

ACKNOWLEDGMENTS

This dissertation is dedicated to my previous advisor, Dr. Steven P. Levitan, who unfortunately passed away in 2016. He was such a great mentor that guided me to find the purpose of my life.

I would like to thank my current advisors, Dr. Anna C. Balazs and Dr. Samuel J. Dickerson, for their constant support and unlimited patience. I would like to thank Dr. Donald M. Chiarulli, Dr. Zhi-Hong Mao and Dr. Kartik Mohanram for their help and advice in my dissertation defense. In addition, I would like to say thank you to Dr. Victor V. Yahsin, who helped me so much in my research and gave me previous suggestions. Also, I extend my gratitude to Joni D. Carlin and Sandra Weisberg for their assistance. This work could not have been done without their help.

A lot of thanks to Natalie S. Janosik, my loyal friend and Padawan, for her endless support and trust. I want to send my sincere appreciation to my parents, Jian Fang and Qiwen Yan, for their eternal love and care. Finally, I would love to express my unlimited gratitude to my beloved, Xiaoyue Hu, for giving me selfless support and love in the most difficult time in my life.

I want to give my love to all of you, to the scientific research that drives our brilliant civilization forward, and to the vast and beautiful world that gave us life and keeps us guessing.

*“Imagination is more important than knowledge. For knowledge is limited,
whereas imagination encircles the world.”*

—— Albert Einstein

1.0 INTRODUCTION

1.1 MOTIVATION

Although the performance and size of computing systems have been continuously improving for decades, the traditional use of stored-program architecture and integrated circuits based composition has not changed too much. As the CMOS technology approaches the limits of scaling, computers based on high performance processors and monolithic memory is coming to the end of its usefulness due to the power consumption and the need to provide more human-centric interfaces for sensing and actuation [1][2]. Especially in the field such as wearable device, robotics, or biomedical applications, more compliant and flexible computing systems are in demand because of inconvenience of deploying traditional computer.

From the standpoint of materials, material and robotic scientists also share a similar vision from the material perspective. They propose the development of a new generation of truly smart material systems that can change their appearance and shape autonomously by tightly integrating sensing, actuation, and computation into composites [3]. For example, these artificial intelligent materials can be applied to airfoils that change their aerodynamic profile, vehicles with camouflage abilities, bridges that detect and repair damage, or robotic skins and prosthetics with a realistic sense of touch [3]. Currently, the most promising approach for these materials is to embed sensors, actuators, and microprocessors with certain density into the continuous

material systems, and the integrated digital hardware locally enable the function of signal processing, computing, and communication [3].

However, the massive implantation of microprocessors with high density in material systems may cause large power consumption and high manufacturing cost. Thus, thinking from the perspective of the computer science domain, we can imagine new computing platforms, or “fabrics”, in the future that may not be similar to the current hardware that consists of multiple electronic components, but rather, will resemble actual fabrics that lie in close contact with the human body or other flexible surfaces. Furthermore, these “soft” computing platforms will also be capable of integrating functions of sensing, computing, and communication.

Clearly, this requests the development of new materials that are lightweight and mechanically compliant or deformable, and also be sensitive and responsive to applied force like touch and motion. Meanwhile, these materials can perform a certain degree of computing, which potentially enrich the life of the human wearing this fabric. Thus, the future vision is to transform computing platforms away from desktops or even mobile devices, to computational fabrics built with new material systems that implementing new computational paradigms.

Other paradigms such as “fabrics” of electronic computing devices have been studied for decades, from programmed logic arrays, seas-of-gates, field-programmable-gate-arrays to “smart pixels.” These computing fabrics can be viewed as networks of combinational logic with periodic restoring storage that are interconnected by communications channels. Recently, researchers have looked at the coupled arrays of oscillators as replacements for Boolean logic to perform pattern matching and image recognition tasks [4]. This work has shown very positive early results, while also limited by the system I/O problems of gathering sensory data (light, temperature, pressure) from external environment.

Concurrently, with this evolution in computing, materials scientists invented a new type of soft oscillating material called Belousov–Zhabotinsky (BZ) gel [5][6], and developed an understanding of its unique abilities of autonomously oscillate, couple, and communicate with each other [7][8][9]. Moreover, these gels are responsive to environmental conditions which can enable the sensing of light [10], heat [11], and pressure [12]. Although with a limited speed, the material systems based on BZ gel would not need external transduction to receive information from environment. Therefore, there exists a unique opportunity to combine the BZ gel based material systems and oscillator based computing into a new thrust into materials that compute.

1.2 PROBLEM STATEMENT

The main issue that this dissertation addresses is the development of integrated sensing, computing, and communicating systems by using non-linear oscillating chemical materials to perform spatio-temporal processing and recognition tasks. The detailed questions we address are the following:

- From the perspective of material science, how to design the basic structure of this material based computing system? If we use a chemical oscillating material like BZ-PZ gel, how can we connect and couple the basic components? How should we organize the material system components so that it would be capable of computing? What periphery components are necessary for our design?
- From the computer engineering aspect, which computing paradigm can be used to create our material system? If we follow our previous experience on oscillator based computing, what is the architecture that implements the computing task suitable for this problem?

- The chemical reaction tends to be very slow, how can we speed up the processing of information and simultaneously strengthen the coupling between oscillators? What is the input and output of encoded information? Furthermore, how is information represented inside the system?
- It is important that we simulate and analyze the system since the dynamics model of nonlinear chemical reaction is complicated and time-consuming for computer-based simulation. Which mathematic tool or method can we use to reduce the computational complexity?
- From the algorithmic level, how can we define the computational task to demonstrate the capability of the new material system? What types of data set can we used for demonstration?

1.3 RESEARCH CONTRIBUTIONS

The contribution that our work makes to the area of the “materials that compute” can be summarized as the following:

- We propose a new material system that can compute based on coupled hybrid chemo-mechanical oscillators. In this system, we design coupled oscillator networks with programmable dynamic stable states that can be used to store binary patterns. This system can perform pattern recognition tasks by measuring synchronization time of coupled oscillator networks [13].
- We study the mathematics methods for the analysis of nonlinear coupled oscillators and provide phase model of the hybrid material oscillators utilized in our system. This phase

model reduces the complexity of the theoretical model and simplifies the behavioral analysis of oscillators [14].

- We conduct computational experiments and simulation of our system on the pattern recognition tasks. The experiment results indicate that this new material system composed of the BZ-PZ oscillator networks are capable of performing pattern recognition tasks. The convergence time to the stable synchronization provides a robust measure of the degree of match between the input and stored patterns [13].
- We propose a multi-channel BZ-PZ device that employs multiple BZ-PZ oscillator networks. Such a system can perform pattern matching on complex multi-dimensional data, such as colored images. By decomposing a colored image into sets of binary vectors, we use each BZ-PZ network, or “channel”, to store distinct information about the color and the shape of the image and detect defects in different features. Our simulations reveal that the proposed system can detect remarkably subtle differences in spatial features between the input and stored patterns and showed its potential in cryptography or steganography [15].
- We introduce capacitors into a single BZ-PZ network. Our numerical simulation indicates that the capacitors modify the strength of coupling between the oscillators in the network, modify the modes of synchronization, and results in additional stable states. We notice the splitting of phases in the synchronization modes caused by the capacitors can significantly enrich the information representation and storage [16].
- We analyze the proposed BZ-PZ oscillator network with capacitors by formulating the phase dynamics equations and performing linear stability analysis. The combined theoretical analysis tool can be used to predict and validate both modes and rate of

synchronization under complex system configurations. We applied BZ-PZ oscillator network with capacitors to the recognition task on a grayscale image dataset, COIL (Columbia Object Image Library), with ten object categories and demonstrate that the sum of convergence time from different oscillator groups can be used as the distance metric for this dataset.

1.4 DISSERTATION ORGANIZATION

The remainder of this dissertation proposal is organized as follows: In [Chapter 2](#), we provide the theoretical background for this dissertation. We introduce the previous works on oscillator based computing and oscillator neural networks, which inspired our design in this work. Then we give a short introduction to BZ gels and provide relative mathematic models. In [Chapter 3](#), we study the phase models of coupled oscillators, which can be used to describe the oscillation behavior effectively and accelerate the simulation of coupled oscillator systems. In [Chapter 4](#), we describe the design of our new material computing system in detail, including the hybrid BZ-PZ oscillator and coupled networks. We discuss the storage and input of patterns with BZ-PZ network and focus on the application in pattern recognition. In [Chapter 5](#), we propose the multiple BZ-PZ Networks in parallel and apply it in detecting defects of colored patterns. We demonstrate the multi-channel mechanism and apply the proposed system to the defects detection of colored QR-code. In [Chapter 6](#), we introduce the BZ-PZ oscillator network with capacitors. We discussed the theoretical analysis and numerical simulations of our system in detail and test it in the pattern recognition task with the COIL dataset.

2.0 BACKGROUND

In this chapter, we provide background information from both computer science and material science related to this work -- oscillator based computing and the Belousov–Zhabotinsky (BZ) gel.

2.1 OSCILLATOR BASED COMPUTING

Pursuing high-density, low-power, high-speed computing systems for the post-CMOS era drives researchers to exploit the potential of emerging nano-device technologies. Nonetheless, with the constraint of building computing systems with traditional Boolean logic, it is difficult for these new technologies to outperform prevailing CMOS technology in computing speed or power dissipation [2][17]. Thus, investigations of nanotechnology to replace the CMOS transistor for Boolean computing structures with a more energy efficient device have been largely unsuccessful. However, because some of these devices possess characteristics of multi-state response that differ from traditional CMOS transistors, it is possible to effectively utilize them in non-Boolean information processing systems for applications like neural computing, computer vision, and pattern recognition.

Based on recent advances in emerging nano-devices such as spin torque oscillators (STO) [18][19], resonate body transistor oscillators (RBO) [20], and vanadium oxide oscillators (VO₂)

[21], systems built from coupled nano-oscillators have become promising candidates for next generation computing structures used in intelligent information processing [22]. Inspired by the interaction between neural oscillation that occurs at different time scales in biological systems, Hoppensteadt and Izhikevich developed an associative memory model of coupled oscillators using phase locked loops and provided examples of how this dynamic system performs recognition by forming attractor basins at the minima of a Lyapunov energy function [23]. Locally coupled oscillator arrays inspired by visual cortex can also perform image segmentation and scene grouping [24].

Besides biologically inspired systems, pattern matching or nearest neighbor searching is another effective and useful application of oscillator based computing. Similar to an associative or content addressable memory, pattern matching is performed between an input vector and a pool of stored vectors, where one or several closest vectors are required to be retrieved. The distance metric for vector comparison in pattern matching can be obtained by observing how well oscillators synchronize with each other.

The essential idea of utilizing coupled oscillator systems to perform computation lays in the energy transfer in a dynamical system. Initialized with input information, a number of oscillators interact and exchange energy with each other, making the whole dynamical system converge from a perturbed state to a stable state. This process brings several advantages to oscillator based pattern matching. First, it provides a higher level multi-dimension norm like the Euclidean distance between sets of input vectors, compared to the Hamming distance computed with exclusive-OR Boolean operations. Second, it is suitable for high dimension large data sets due to its scalability and the fact that the degree of match spans all of the dimensions of an input vector without any arithmetic calculations [25]. Third, with the high frequency of new devices

like STOs, the systems can converge quickly. Although systems built from these nano-devices have not been realized to date, prototypes using traditional circuits have been built and simulated [26]. Further, simulations of systems using nano-oscillators have shown promising results [27].

In general, the configuration of oscillator based computing systems, such as network topology, input pattern representation, detection of output results and “degree of match”, has numerous varieties; and, the design of these circuits can be tailored by specifications from system designers. Recently, research has been conducted not only from the perspective of devices and circuits [26][28], but also at the level of algorithms and architectures [25][27].

In this section, we give a brief introduction to Izhikevich’s Oscillator Neural Network and the oscillator computing paradigm of pattern matching for image processing as an example.

2.1.1 Oscillator Neural Network

Hoppensteadt and Izhikevich study weakly connected networks of neural oscillators that behave as an associative memory [31]. They propose a canonical model for oscillatory dynamic systems represented by the equation below:

$$\frac{dz_i}{dt} = (\rho_i + i\omega_i)z_i + d_i z_i |z_i|^2 + \varepsilon \sum_{j=1}^n C_{ij} z_j \quad (2-1)$$

Where:

- $z = x + iy$ Complex oscillator variable
- ρ_i Damping of oscillators
- ω_i Natural frequencies of oscillators
- d_i Nonlinear factor, ensures stable amplitude
- ε Coupling parameter, typically small (weakly coupled)

- C_{ij} Coupling matrix, represent coupling strength between two oscillators similar to the weight matrix in previous models

This dynamic model was proven to be able to form attractor basins at the minima of a Lyapunov energy function by adjusting the coupling matrix though a Hopfield rule [32]. In other words, a network that consists of oscillators described by this canonical model can learn patterns as represented by phase difference and perform the functions of an associative memory. The memorized patterns are programmed by the coupling matrix. The initial phase is determined by an input pattern. When the system converges to stable state, the phase differences among oscillators represent the output pattern of associative memory. The structure of network is depicted in Figure 2.1.

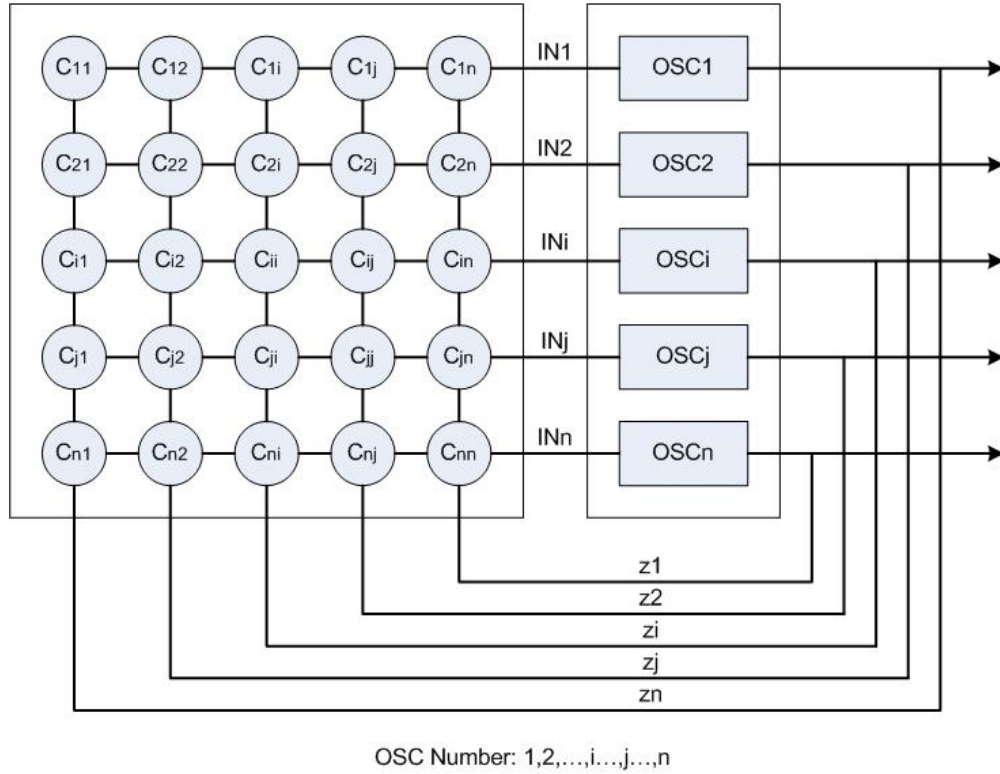


Figure 2.1 Oscillatory Neural Network Structure

The oscillator cluster (OSC1, OSC2, OSC3, ..., OSCn) are coupled by a matrix of multipliers and adders that contain the coupling coefficients, shown as the C_{ij} box. From the list term of the equations above, the outputs are fed back to the network for the recurrent evolution process until the network state is completely stabilized at an attractor.

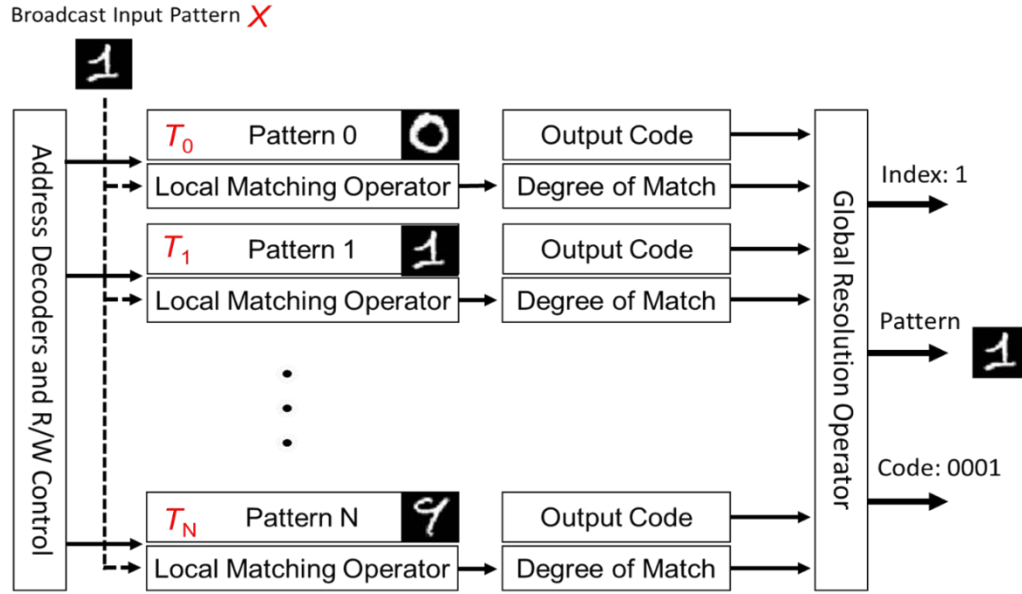


Figure 2.2 Associative Memory Model for Handwritten Digits

2.1.2 Pattern Matching

Pattern matching is basically a nearest neighbor search operation and the patterns can be images, features, or vectors, depending on different applications. Figure 2.2 shows an abstract view of a “content addressable” associative memory [33]. Here, a set of associative storage words constitute a single large memory. The set of pattern vectors to be matched (e.g., handwritten digits) are first stored in the memory as template pattern vectors. In this paper, we define “templates” as the stored pattern vectors of associative memory. Depending on the application,

codes that correspond to the templates are also stored. Matching operations proceed by broadcasting (on a bus) input vectors to all words in the memory. Then, each word performs a local comparison or match operation. This local match operation is relative, generating a “degree of match” between the input pattern vector and the local template stored in the word. Next, the degree of match from each word is compared by a global resolution function, and the best matching result is output.

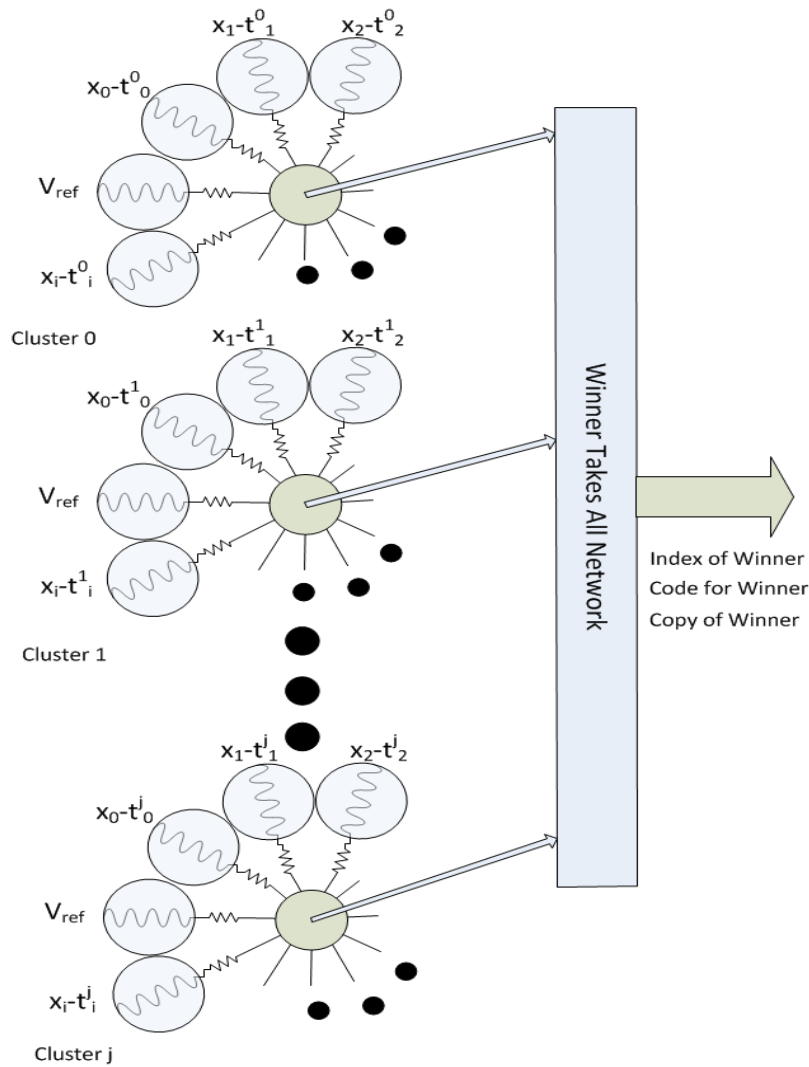


Figure 2.3 Coupled oscillator based associative memory module.

Figure 2.3 shows the architecture of a single Associative Memory module composed of coupled oscillators. The module contains multiple clusters of oscillators connected to each other with a “star” structure around a summing node. Each cluster has a template memory, T^j , that holds a vector of t_i^j values (j is the index of the template vectors). The template memory can be either digital or analog. For digital memories we would need D/A converters to provide the template values to the oscillator clusters for comparison. Once the templates are loaded, comparisons happen between every oscillator cluster and the input pattern vector, X . This process starts from initializing the frequencies or phases of each oscillator with the difference between element values of X and T^j . The degrees of match (DoM) between the input pattern and the stored templates are then determined by how well a cluster of oscillators synchronizes. If X and T^j are similar to each other, the oscillators’ final frequencies or phases are the same or close to each other. Otherwise, the oscillator cluster will generate a more chaotic desynchronized signal. In other words, the coupled oscillator system behaves like a kernel that gives the distance measure between two vectors, which is very similar to squared Euclidean distance. In the other chapters, we will see the way of measuring DoM is various depends on different oscillator systems. For example, it may not only be the voltage from the common node, but also the convergence time of the whole network.

This oscillator based associative memory system is compatible with different types of oscillators. For instance, recently a low power design for this computing paradigm was implemented with Spin Hall Effect STO CMOS and interface circuits [34]. Here we use ring oscillators for demonstration because they can be efficiently implemented with CMOS techniques and their behavior was analyzed in previous work [35]. Figure 2.4(a)(b) gives an example of the circuit design of a coupled ring oscillator cluster for pattern matching. For these

oscillators, the frequency of each oscillator is adjusted by two input control voltages and the coupling node is the output node of the third inverter. The frequency control voltages, V , and \bar{V} are the pair-wise difference of vectors, $|X - T^j|$. The oscillators are coupled to each other through a common node, where the coupling components could be resistor or capacitor, where larger resistors would give weaker coupling strength. The output signal of the common node is amplified and rectified to form a DoM detection circuit. Other DoM detection techniques and circuits can be found in [26]. In general, the design of the DoM detection circuit is a function of the frequency and wave-shape of the oscillators and the coupling circuit. Fig. 2.4(c) shows how close the distance metric is to the squared Euclidean distance for an optimized design. In this three-oscillator system, one oscillator's frequency, F_3 , is swept while the other two remain fixed. The scatter plot of $(1 - DoM)$ is generated by the DoM detection circuit in Fig. 2.3(b). It is compared against the quadratic curve fit model $(1-F_3)^2$. In this diagram, frequencies are normalized to 1.

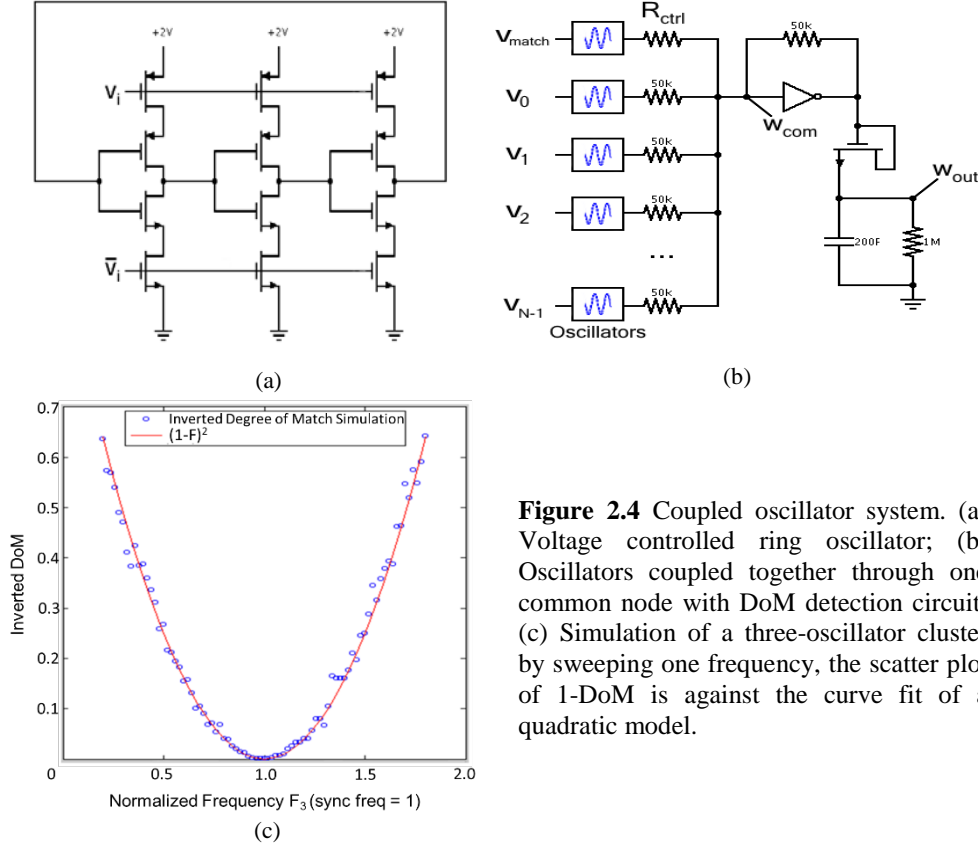


Figure 2.4 Coupled oscillator system. (a) Voltage controlled ring oscillator; (b) Oscillators coupled together through one common node with DoM detection circuit; (c) Simulation of a three-oscillator cluster by sweeping one frequency, the scatter plot of 1-DoM is against the curve fit of a quadratic model.

In an image processing pipeline for object recognition, pattern matching can serve as the nearest neighbor search classifier in the back-end. Experiment results of matching operation performed by oscillator clusters on the classification of MNIST dataset are provide in one of my journal papers [4]. There are also other oscillator computing paradigms that had been designed to play different roles in image processing applications. For example, oscillators can be used to perform the convolution operation [36], which is widely exerted in object recognition models like convolutional neural networks [29] and the HMAX model [30]. Another oscillator computing paradigm for image segmentation can be applied in the image preprocessing [37].

2.2 CHEMICAL MATERIAL OSCILLATORS

In this section, we give a brief introduction of the Belousov–Zhabotinsky (BZ) gel oscillators, which is a vital component in the hybrid material system designed in our work. Such type of hydrogel can periodically swell and de-swell, driven by the BZ oscillating chemical reaction. This self-powered chemo-mechanical oscillation enable BZ gel to actuate.

2.2.1 Belousov–Zhabotinsky Reaction



Figure 2.5 Pattern formed by the concentric waves in BZ reaction (Source: Flickr; Photo by Stephen Morris; Chemistry by Michael Rogers)

Belousov–Zhabotinsky (BZ) reaction is a family of oscillating chemical reactions that exhibit constantly periodic change in the concentration of some reactants, resulting oscillation in non-

equilibrium thermodynamics [38][39]. During these reactions, transition-metal ions (e.g. Ce^{+3}) catalyze the oxidation of itself and some organic reductants by bromic acid. When the concentration of oxidized catalyze ions (e.g. Ce^{+4}) reach a threshold, the bromic acid starts to decompose and the oxidized catalyze is reduced. These oxidation reactions and reduction reactions dominate alternatively, arising the oscillation of the concentration of multiple ions (Br^+ , BrO_2^+ , Ce^{+4}). The BZ reaction can last several thousand oscillatory cycles without constantly refueling reactant, and thus makes it much easier for human eyes to observe the formation of temporal and spatial complex patterns in chemical reactions. In BZ reaction, concentration waves can propagate in reaction-diffusion systems with oscillatory or excitatory local chemical kinetics [40][41]. Figure 2.5 shows the pattern formed by the concentric waves.

2.2.2 BZ Oscillating Gel

Ryo Yoshida developed a type of self-oscillating polymer gels by converting the chemical oscillation of the BZ reaction to automatic swelling–deswelling mechanical changes of gels [5][6]. This self-oscillating polymer is created by attaching the catalyze $\text{Ru}(\text{bpy})_3^{2+}$ to the polymer chains of NIPAAm. The poly(NIPAAm- co - $\text{Ru}(\text{bpy})_3^{2+}$) gel has a phase transition temperature because of thermosensitive constituent NIPAAm, while the oxidation and reduction of $\text{Ru}(\text{bpy})_3^{2+}$ change both the temperature and diameter of poly gel particles. In the presence of the reactants, this polymer gel undergoes spontaneous cyclic swelling–deswelling changes without any on–off switching of external stimuli.

The kinetics of the BZ reaction can be described by a modification of the Oregonator model [42], formulated in terms of the dimensionless concentrations of the key reaction

intermediate u (HBrO_2 , the activator), and the oxidized metal-ion catalyst v (Ru^{3+} in the case considered here). The modified model [7][43] accounts for the dependence of the BZ reaction rates on the volume fraction of polymer ϕ , and on the total concentration of catalyst grafted to the network. The reaction rates F_{BZ} and G_{BZ} are determined as follows:

$$F_{\text{BZ}}(u, v, \phi) = (1 - \phi)^2 w r - u^2 - (1 - \phi) f v \frac{u - q(1 - \phi)^2}{u + q(1 - \phi)^2} \quad (2-3)$$

$$G_{\text{BZ}}(u, v, \phi) = \varepsilon_{\text{BZ}} [(1 - \phi)^2 w r - (1 - \phi) v] \quad (2-4)$$

The reaction rates depend on the dimensionless concentrations of the reduced catalyst Ru^{2+} and the radical BrO_2^* denoted by r and w , respectively. The concentration r is calculated as $r = c_{\text{Ru}} \phi_0^{-1} \phi - v$, where c_{Ru} and ϕ_0 are the catalyst concentration and volume fraction of polymer in the undeformed gel, respectively. The concentration of the radical w is found as $w = \mu_{\text{BZ}} (r^2 + 2u / \mu_{\text{BZ}})^{1/2} - \mu_{\text{BZ}} r$, where μ_{BZ} is a dimensionless parameter. Finally, the stoichiometric factor f and the dimensionless parameters q and ε_{BZ} have the same meaning as in the original Oregonator model [42].

We assume that the chemical composition of the BZ substrate and the volume fraction of polymer in the undeformed gel are the same as used in the experiments described in [7], so the corresponding dimensionless parameters are estimated to be $\varepsilon_{\text{BZ}} = 0.212$, $q = 9.52 \times 10^{-5}$, $\mu \approx 7 \times 10^2$, and $\phi_0 = 0.16$. The stoichiometric parameter f and the catalyst content c_{Ru} are the adjustable parameters in the study, and we assume them to be $f = 1$ and $c_{\text{Ru}} = 3$.

The osmotic pressure of the polymer in gel is calculated according to the Flory-Huggins theory,

$$\pi_{\text{FH}} = -[\phi + \log(1 - \phi) + \chi(\phi)\phi^2] \quad (2-5)$$

Here, $\chi(\phi)$ describes the polymer-solvent interactions. It is calculated as $\chi(\phi) = 0.338 + 0.518\phi$, which is known to describe the PNIPAAm-water interaction at 20°C [44].

2.3 DISCUSSION

This Chapter first introduces the background of previous work in oscillator-based computing, including the oscillator neural network and a computing paradigm for pattern matching in our preliminary work. Then we provide a brief introduction to the BZ reaction and the mathematic model of the BZ oscillating gel.

3.0 PHASE MODELS FOR COUPLED OSCILLATORS

The simulation and analysis of these oscillator computing paradigms are usually difficult and time-consuming. In this Chapter, we try to address the problem by studying the phase models of oscillators, which can be used to effectively describe the oscillator behavior and efficiently speedup the simulation of systems.

3.1 MATHEMATIC MODEL

In this section, we try to address the problem by studying the phase models of oscillators, which can be used to effectively describe this behavior. We first review phase models proposed in previous work, including the PPV model [45][35], Winfree's and Malkin's approaches summarized by Izhikevich [46]. By discussing the relation between these models and combining their advantages, we develop our own phase model for the simulation oscillator-based computing systems.

3.1.1 PPV Model

We start with the Phase Projection Vector (PPV) model, since it is derived from the demand for a theoretical analysis of oscillator circuits perturbed by noise and therefore is easier to understand from an electrical engineering perspective compared to the other models [45].

The PPV model starts with the general differential equation of an oscillator,

$$\dot{\mathbf{x}}(t) = \mathbf{f}(\mathbf{x}(t)) + \mathbf{P}(t) \quad (3-1)$$

where $\mathbf{x}(t)$ is the vector of oscillation states and $\dot{\mathbf{x}}(t)$ is their derivatives. In real circuits, these states are usually the voltages or currents of nodes. $\mathbf{P}(t)$ represents an external perturbation on the oscillation, which can be noise, signal injection, or in this case, a coupling term from other oscillators. \mathbf{f} is the nonlinear function that describes the oscillation and t is time. We assume the perturbation is small and it only changes the phase of the oscillators. Then, the response solution from this equation can be written as,

$$\mathbf{x}_c(t) = \mathbf{x}_s(t + \alpha(t)) \quad (3-2)$$

where $\mathbf{x}_s(t)$ is the oscillator's natural response without any perturbation, namely $\mathbf{P}(t) = 0$, while $\mathbf{x}_c(t)$ is the response with perturbation. $\alpha(t)$ represents the time shift of phase that is caused by the perturbation. Hence equation (3-1) reveals the phase relation between the natural response and the perturbed response of the oscillator. According to the PPV model, $\alpha(t)$ can be obtained by solving the equation,

$$\dot{\alpha}(t) = \Gamma(t + \alpha(t))\mathbf{P}(t) \quad (3-3)$$

where $\Gamma(t)$ is the perturbation projection vector (PPV) that describes the perturbation response of the oscillator. The PPV can be thought of as the time-varying sensitivity of the induced time shift to the given injected perturbation [35]. The theoretical derivation and proof of the PPV method

can be found in [45]. The PPV, $\Gamma(t)$, is usually a periodic function that can be obtained either numerically or analytically. After acquiring $\Gamma(t)$, we know the time shift of phase $\alpha(t)$ from the solution of equation (3-3) and thus can solve equation (3-2). This model is referred as analytical PPV in this paper.

This model actually does not predict the “phase change” but a time shift function of oscillation response. Thus, it is difficult for us to use this model to directly predict the frequency shift in a coupled oscillator system. The next models we introduce provide us further insight.

3.1.2 Izhikevich’s Model

In [46], the phase model of weakly coupled nonlinear oscillators is explored from an abstract view by unifying some earlier models. Differing from the PPV model, this model assumes all the oscillators share the same free-running frequency, so the “phase” of nonlinear coupled oscillators can be normalized and defined as,

$$\theta(t) = t + \varphi(t) \quad (3-4)$$

Taking the derivative of both sides, we have,

$$\dot{\theta}(t) = 1 + \dot{\varphi}(t) \quad (3-5)$$

In equations (3-4,5), $\theta(t)$ is the defined phase, a periodic function with period $T = 1$. $\varphi(t)$ is called the phase deviation, caused by the coupling from other oscillators. We can notice that when there is no coupling term, the phase term is simply time, t , and the free-running frequency is normalized to 1. The derivative $\dot{\varphi}(t)$ represents the change of phase deviation, namely the frequency shift, due to the coupling effect.

In order to map this model to various nonlinear oscillators, the key point lies in the phase deviation $\varphi(t)$, described by:

$$\dot{\phi}(t) = Q(\theta(t))P(t) \quad (3-6)$$

which has a similar form to equation (3-3). $P(t)$ is the same external injection signal to the oscillators (i.e., the coupling term). The function $Q(\theta)$ is called the phase response curve or phase resetting curve (PRC), representing how sensitive the phase deviation is in response to $P(t)$ at a specific phase $\theta(t)$. Thus (3-5) can also be written as,

$$\dot{\theta}(t) = 1 + Q(\theta(t))P(t) \quad (3-7)$$

The mechanisms of phase and frequency interactions of coupled oscillators revealed by this equation was discovered multiple times in the early studies of oscillator phase models and some researchers named it PRC in different ways and exploited different methods to derive and utilize it. A theorem first proposed by Malkin in 1949 and later abstracted by Hoppensteadt in 1997 indicates that $Q(\theta)$ can be computed by solving the linear adjoint equation,

$$\dot{Q}(t) = -J[f(x(t))]^T Q \quad (3-8)$$

where $J[f(x(t))]^T$ is the transposed Jacobian matrix of the oscillation function f . This theorem is identical to Kuramoto's approach [47], where the gradient of phase plays the role of PRC. In Winfree's work [48], PRC was experimentally approached by applying a pulse stimulus with amplitude A . Then a function called the linear response or sensitivity function $Z(\theta)$ was measured by observing the phase shift caused by the stimuli, and PRC is $Z(\theta)$ divided by amplitude A .

$$PRC(\theta) \approx (Z(\theta))/A \quad (3-9)$$

This method is flexible and intuitive. However, being experimental, it suffers from more variation and inaccuracy. Nonetheless, it is useful when the nonlinear oscillator equations is not differentiable or continuous.

3.1.3 Combined Simplified Model

From the previous models discussed above, if we pair equations (3-1,4), (3-2,5), and (3-3,6) and compare them, we can notice that they have the same pattern because the intrinsic method behind these models is the same, which is to quantify how the oscillation is affected by the external perturbation. However, these models use different methods to calculate this term, either an analytical derivation or a numerical measurement. In addition, the PPV model studies the oscillation variables themselves while Izhikevich's model focuses on the "phase" of nonlinear oscillators.

From the view of solving the practical problem we are addressing, the pattern matching operation is performed by frequency shifting or frequency locking of oscillators caused by coupling. The elements of the pattern vectors are represented by frequencies and the degree of match is evaluated by how well the oscillators synchronize. Thus, for the purpose of predicting the frequencies of coupled oscillators, we introduce the phase definition idea from Izhikevich's model into the PPV model.

We assume we have n oscillators with different frequencies: $\omega_0, \omega_1, \omega_2 \dots \omega_{n-1}$. Since equations (3-4) and (3-5) require that oscillators run at the natural frequencies normalized to 1, we scale these frequencies to 1, $\lambda_1, \lambda_2 \dots \lambda_{n-1}$, where $\lambda_i = \frac{\omega_i}{\omega_0} = \frac{T_0}{T_i}$. So for an arbitrary oscillator i , in the PPV model, equation (3-2) can be changed into the phase form similar to (3-4):

$$\theta_i(t) = \lambda_i(t + \alpha(t)) = \lambda_i t + \varphi_i(t) \quad (3-10)$$

with

$$\varphi_i(t) = \lambda_i(\alpha(t)) \quad (3-11)$$

which indicates the relation of phase deviation in Izhikevich's model and time shift of phase in the PPV model. Taking the derivative of (3-10) we get,

$$\dot{\theta}_i(t) = \lambda_i + \lambda_i \alpha(t) \quad (3-12)$$

substituting with (3-3) we have,

$$\dot{\theta}_i(t) = \lambda_i + \lambda_i \Gamma(\theta_i(t)) P_i(t) \quad (3-13)$$

where $\Gamma(\theta_i(t))$ is still the PPV in (3-3) but determined by the phase, instead of time. This equation transfers the PPV from a time domain to the phase domain and replaces the simulation time span into the number of oscillation cycles. $P_i(t)$ is the coupling term here in this model, defined as:

$$P_i(t) = \sum_{j=0}^n g_{ij} x_s(\theta_j(t)) \quad (3-14)$$

where g_{ij} is the pair-wise coupling coefficient and j is the index of other oscillators in the system. Therefore, solving (3-13) can provide the frequency and phase response of a coupled oscillator system. In our simplified model, the PPV function is also equivalent to the PRC function obtained from other methods. In the next section we give examples of these methods. We note that it is useful to have several methods available because some methods might prove inaccurate or fail to converge for specific nonlinear oscillator systems.

3.1.4 Oscillator Examples

In this section we use ideal ring oscillators as an example and demonstrate three different methods to obtain their PPV/PRC function. A simple ring oscillator consists of three inverters and RC circuits, shown in Figure 3.1(a) with its analytical model given in [35], presented as below. The voltage derivatives of the three nodes are,

$$\dot{v}_i(t) = \frac{f(v_{ip}(t)) - v_i(t)}{RC}, i = 1, 2, 3 \quad (3-15)$$

where i^p is the previous node of i and $f(v(t))$ is the simplified response of an inverter:

$$f(v) = \begin{cases} +1, & \text{if } v > 0 \\ -1, & \text{otherwise} \end{cases} \quad (3-16)$$

By normalizing the standard frequency and period to 1, we can write the voltage state response of three nodes as,

$$v_1(t) = \begin{cases} 1 - \psi e^{-\gamma t}, & 0 \leq t \leq 1/2 \\ -1 + \psi e^{-\gamma(t-\frac{1}{2})}, & 1/2 \leq t \leq 1 \end{cases}$$

$$v_2(t) = v_1\left(t - \frac{2}{3}\right), v_3(t) = v_1\left(t - \frac{1}{3}\right) \quad (3-17)$$

where $\psi = \frac{1+\sqrt{5}}{2}$, $\gamma = 6\ln(\psi)$. Because the frequency here is 1, $RC = 1/\gamma$. Similarly, the PPV equation can be analytically solved as,

$$\Gamma_1(t) = \Gamma_3\left(t - \frac{2}{3}\right), \Gamma_2(t) = \Gamma_3\left(t - \frac{1}{3}\right)$$

$$\Gamma_3(t) = \gamma^{-1} \frac{1+\psi^3}{4-2\psi^3} (\psi + 2 \left[-u(t) + (-1 + 2\psi^{-1})u(t - \frac{1}{2}) \right]) e^{\gamma t} \quad (3-18)$$

Figure 3.1(b) shows the waveform of oscillation response and PPV of node v_3 . From this plot we see that the PPV function for ring oscillators is periodic and non-linear.

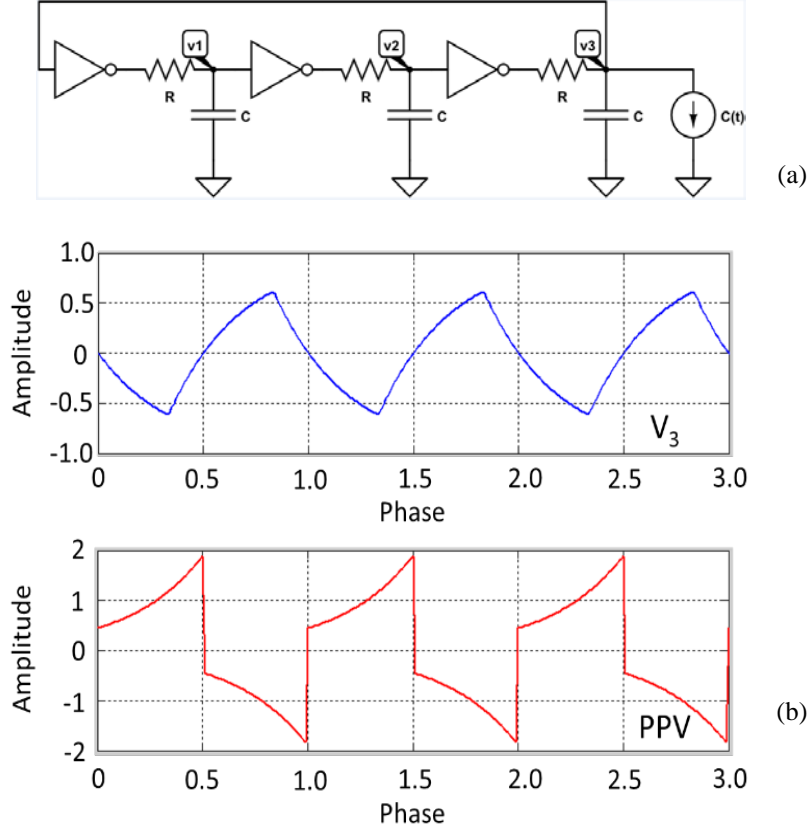


Figure 3.1 Ring oscillator model. (a) Simple schematic model; (b) Output waveform and (PPV) at node v3.

Sometimes it is difficult to obtain the state response and PPV function directly from the ODE. For these cases we can obtain the corresponding PRC by applying Malkin's approach numerically. Solving equation (3-8) is actually very similar to the analytical derivation of PPV in [49]. However, when the analytical method does not work, we can use a technique called backward integration to obtain the Jacobian matrix [46]. Figure 3.2 shows the results of PRC from this method with a backwards integral of 4 cycles. The last cycle of PRC curve is inaccurate due to the special integral technique and usually should be discarded. The PRC in the first cycle is the one used.

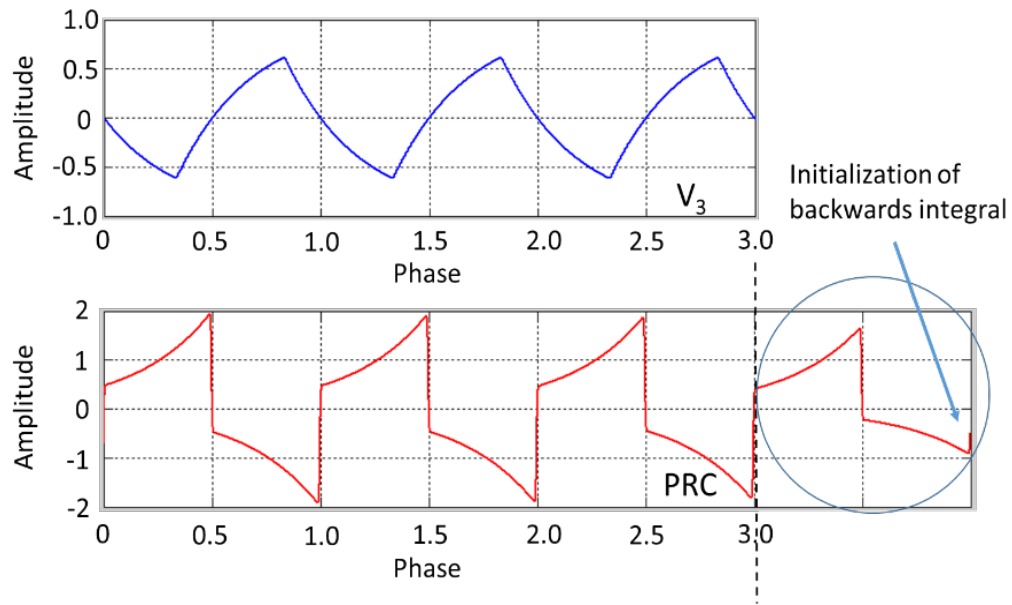


Figure 3.2 Malkin’s approach for PRC. (x-axis: phase, y-axis: amplitude) and output waveform at node v_3 and PRC obtained from backwards integral.

In a few cases when a system’s Jacobian matrix does not exist, Winfree’s approach can be the only choice, especially for those nonlinear oscillators with complex mathematical models, even though this method is “experimental” and tends to be inaccurate. As an example, we apply Winfree’s method for the ring oscillator by adding a pulse stimulus with small amplitude and measuring the phase resetting curve step by step. Figure 3.3 illustrates the PRC generated by Winfree’s method with different stimuli amplitudes. The glitches in the curve show the problems of this approach.

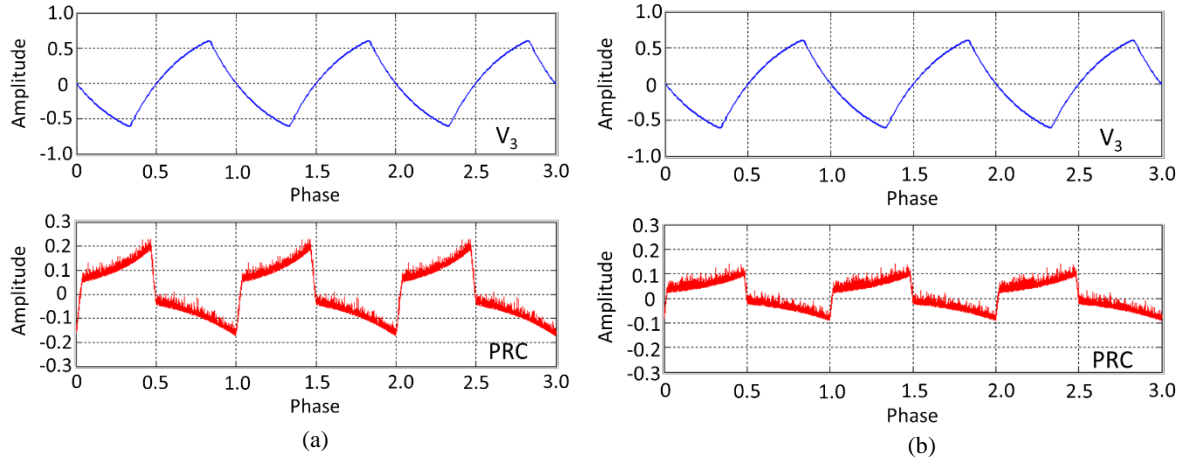


Figure 3.3 Winfree's approach for PRC, (a) Stimuli Amplitude=0.1, PRC Amplitude=0.2; (b) Stimuli Amplitude=0.05, PRC Amplitude=0.1.

However, it is worth noting that the PRC amplitude here is proportional to the stimuli amplitude by factor of 2, which not only corresponds to equation (3-9), but also fits the PPV/PRC amplitude of the previous two methods in Figure 3.1 and Figure 3.2. These three examples for phase deviation of the ring oscillator indicate that PPV and PRC functions are identical to each other and enhance the foundation of our model.

3.2 EXPERIMENTS AND SIMULATION

In this section, we apply our simplified phase model to coupled oscillator systems and analyze their synchronization behavior. We also compare the performance and efficiency of the models obtained by the different approaches as well as accuracy and speedup compared to the direct simulation of the oscillator systems.

As we discussed in the previous section, a weakly coupled system, such as shown in Figure 2.4, can be simply described by equations (3-13) and (3-14). In this structure the coupling strengths between oscillators are identical. Thus, for each oscillator at node v3 in Fig. 4 we have,

$$\dot{\theta}_i = \lambda_i + \varepsilon \lambda_i \Gamma_{node3}(\theta_i) \sum_{j=0}^n v_{node3}(\theta_j), i, j \in [1, n] \quad (3-19)$$

where ε is the coupling coefficient.

3.2.1 Oscillator Behavior Analysis

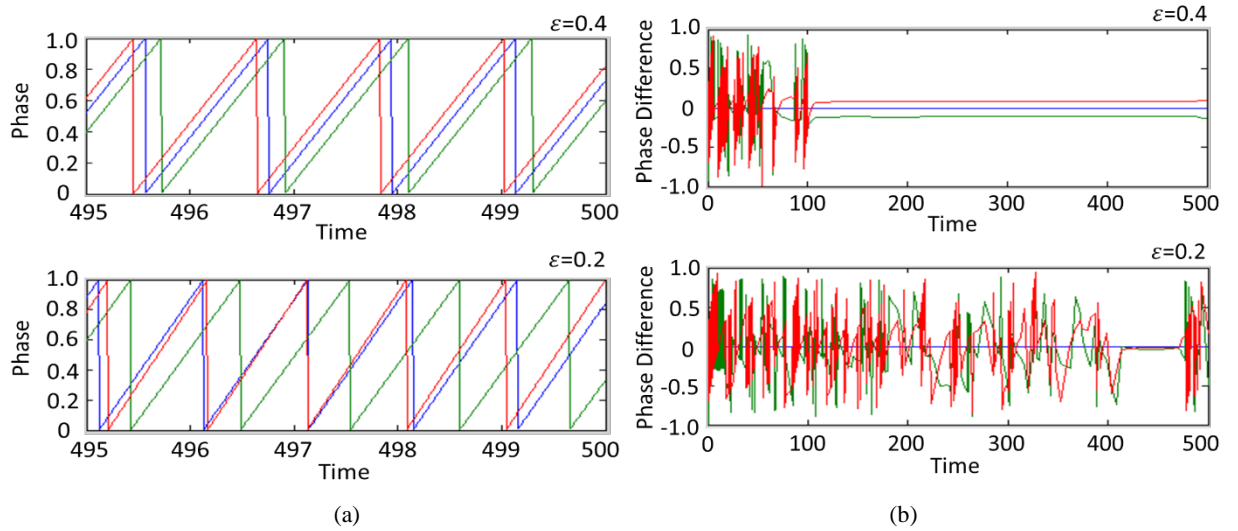


Figure 3.4 Comparing simulations of three coupled oscillators with natural frequencies $\lambda = [1.0, 0.95, 1.05]$, $\varepsilon=0.4$ and 0.2. (a) Wrapped phase waveform of final stage; (b) Evolution of phase differences between oscillators.

We start with a three oscillator system ($n = 3$). It is convenient for us to predict the final frequency of each oscillator by solving (3-19) numerically. If $\dot{\theta}_1 = \dot{\theta}_2 = \dot{\theta}_3$, the system is synchronized and frequency locked. We use Matlab to run a simulation of equation (3-19). Figure 3.4 illustrates an example of locking and non-locking systems. For these examples, we set the initial frequencies to be: $\lambda = [1, 0.95, 1.05]$ but use two different ε , 0.2 and 0.4. In the left

diagram Fig 3.4(a), we give a zoom-in observation of wrapped phases in the final steps of simulation, where $\varepsilon = 0.4$ results the locked final frequencies $[0.8717, 0.8717, 0.8717]$ while $\varepsilon = 0.2$ generates desynchronized final frequencies $[0.9644, 0.9298, 1.0263]$. Figure 3.4(b) shows the phase differences between three oscillators. In the first case, the phase difference is constant while it is unstable in the second case.

From these simulation results, it is worth noting that the conditions for frequency locking are determined by the coupling coefficient ε and the scaling ratio between each oscillators' free running frequency λ_i , not the absolute value of the frequencies. This interesting phenomenon is important for the design of future oscillator based computing systems. It implies that devices with high frequencies can provide wider bandwidth for information coding. Also, even when the oscillators fail to lock with each other, their frequencies are pulled closer to each other. It is based on this observation that we say that the degree of synchronization can provide a metric to measure the distance or similarity of each oscillator's initial frequency (and thus input) as discussed below.

To verify this point, we run the simulation multiple times by fixing the first oscillator's frequency and sweeping the frequency of the other two from 0.8 to 1.2. We use degree of synchronization, $1 - \{(f_2 - f_1)^2 + (f_3 - f_1)^2\}$, as the function to evaluate how well the oscillators synchronize. With this function, we measure how close these final frequencies are to the reference oscillator for comparison between the phase model and direct simulations, and thus to verify the capability of our phase model in simulation of oscillator based computing. Note that f_1, f_2, f_3 here are the coupled frequencies based on normalized phase. In this test, we use the three different methods to obtain the PPV/PRC, as we did in Section 3. In addition, we directly simulate the coupled oscillator with oscillator equation (3-15) as a performance standard. Figure

3.5 demonstrates all the models with 3D plots of the degree of synchronization for the two cases of $\varepsilon = 0.4$ and $\varepsilon = 0.2$. When the coupling strength is weak, the surface is smooth and the initial frequencies are easier to differentiate, while stronger coupling gives us more nonlinear features and a wider locking range. The flat area on the top of the surface indicates the highest degree of synchronization, giving us the frequency locking range for the simulation sweeps. Hence, a very strong coupling system may lack differentiation for pattern matching or nearest neighbor searching. But for clustering operations like image segmentation, stronger coupling strength can provide better resistance to noise. Due to the fast simulation speed, our model is also very suitable for simulating systems with large numbers of coupled oscillators. To understand how the number of oscillators can influence the synchronization, we run the simulations with the same two dimensional frequency sweeping but different numbers of oscillators. Since we cannot show a plot of higher dimensional frequency sweeping, we keep the frequencies of all but two of the oscillators fixed to 1 and sweep the last two.

Figure 3.6 shows the results for $n=3, 4, 8$, and 16 . In these simulations, we use the analytical PPV as the PPV/PRC function. From these results we can notice that larger numbers of oscillators with the same frequency gives a wider frequency locking range. Namely, the effective coupling strength to those oscillators with different frequencies becomes stronger because the system's stable state is close to the state of the majority of the oscillators. This could either be an advantage or disadvantage in the design of oscillator based systems, depending on the application and computation required.

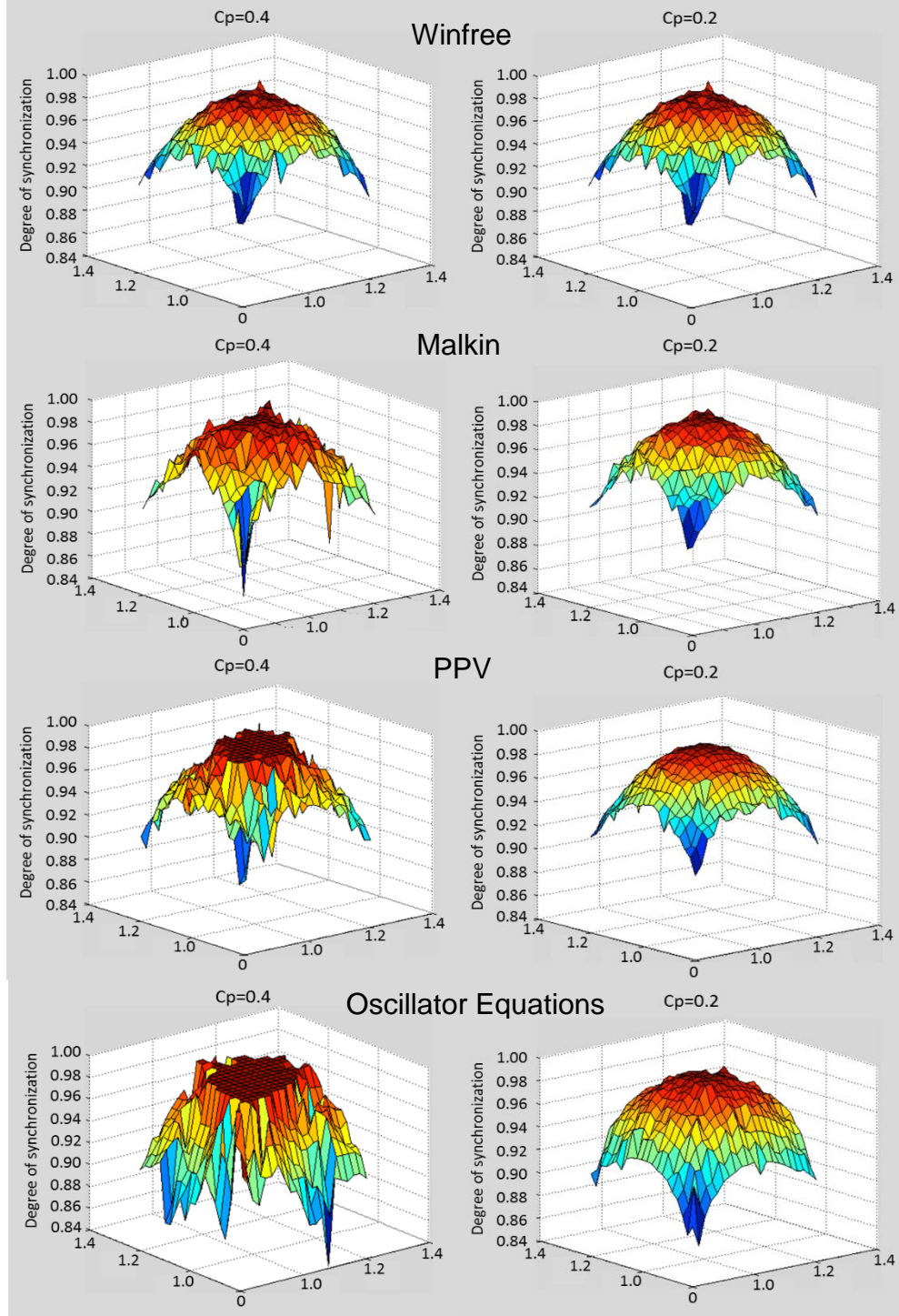


Figure 3.5 Degree of synchronization as inverted Euclidean distance, initial frequencies for a range $\lambda_{2,3}=[0.8 \text{ to } 1.2]$ and a fixed frequency of $\lambda_1=1.0$, Left column: $\epsilon=0.4$, Right column: $\epsilon=0.2$; Row 1: Winfree's approach, Row 2: Malkin's approach, Row 3: Analytical PPV, Row 4: Direct simulation with oscillator equations.

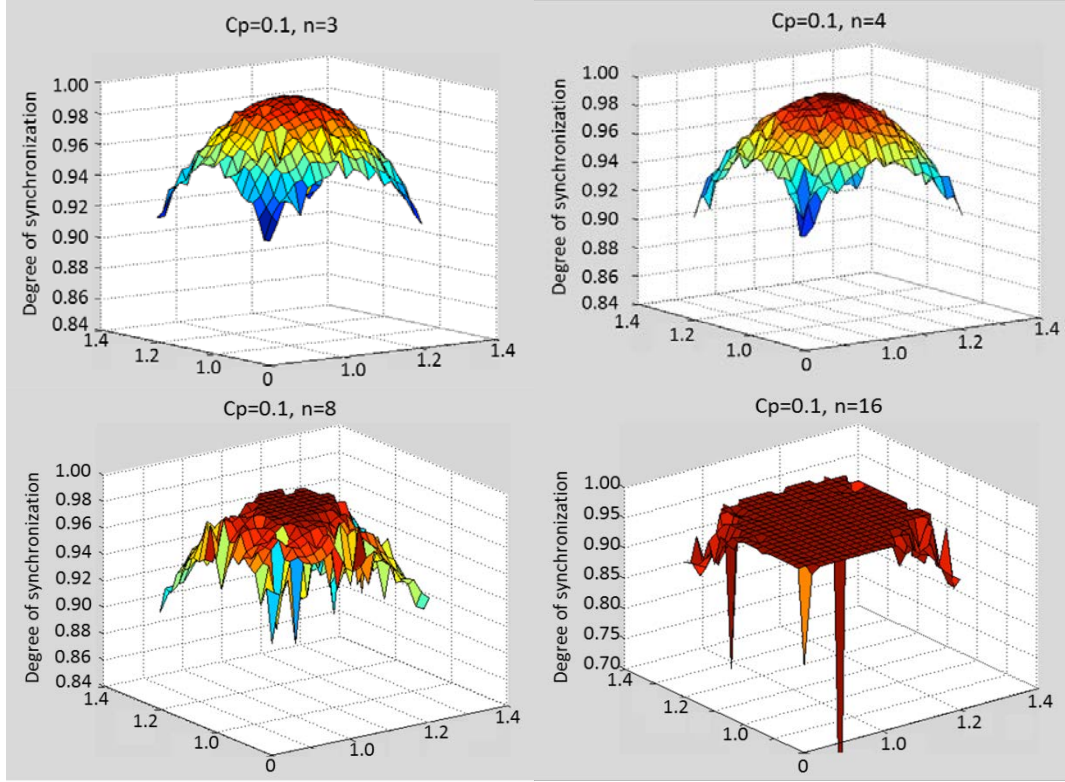


Figure 3.6 Simulations of different numbers of coupled oscillators. All oscillators but two are kept at frequency 1, while the last two are swept.

3.2.2 Performance Speedup

For performance comparisons of our phase model, we calculate the root mean square error between the direct simulation of the oscillators in each case of Figure 3.6 and the analytical PPV. As we can see in Table 1, the error is relatively small compared with the absolute value of degree of synchronization. This shows that our phase model is compatible with different methods for PPV/PRC and robust to the variations between these methods. Compared to the direct oscillator simulation, the analytical PPV generates the smallest error while Winfree's experimental method gives the largest error, and Malkin's numerical method lies in the middle.

Table 3.1 RMSE of simulations based on different methods

Comparing	Winfree's	Malkin's	Analytical PPV
Oscillator, $\varepsilon = 0.2$	127e-04	133e-04	121e-04
Oscillator, $\varepsilon = 0.4$	276e-04	297e-04	271e-04
Analytical PPV, $\varepsilon = 0.2$	58e-04	63e-04	/
Analytical PPV, $\varepsilon = 0.4$	128e-04	142e-04	/

We next evaluate the efficiency of our model by comparing simulation speed to the direct simulation of the oscillator network. The speedup here is defined by the ratio of real time for simulation of two methods (both in Matlab) for the same length of simulation time. Since we always initialize the systems with random phases, we run the test of each configuration 100 times and average the speedup for evaluation. The results in Figure 3.7 only serve as an approximation of the efficiency of our model because the simulation of coupled oscillator systems is affected by multiple factors, such as the oscillator model, initial states, and the convergence process. Nevertheless, we still observe very promising speedups from our simplified phase model, similar to [35]. The speedup comes from the fact that the differential equations of the original oscillators are nonlinear but the simplified phase models are linear equations with much simpler periodic functions. A second advantage is that in the phase domain, simulation is done by fractions of cycles, rather than time steps, so that run time is frequency invariant. This is an advantage in

simulation when compared to the regular PPV model where the user must optimize the time step for accurate simulation vs. performance.

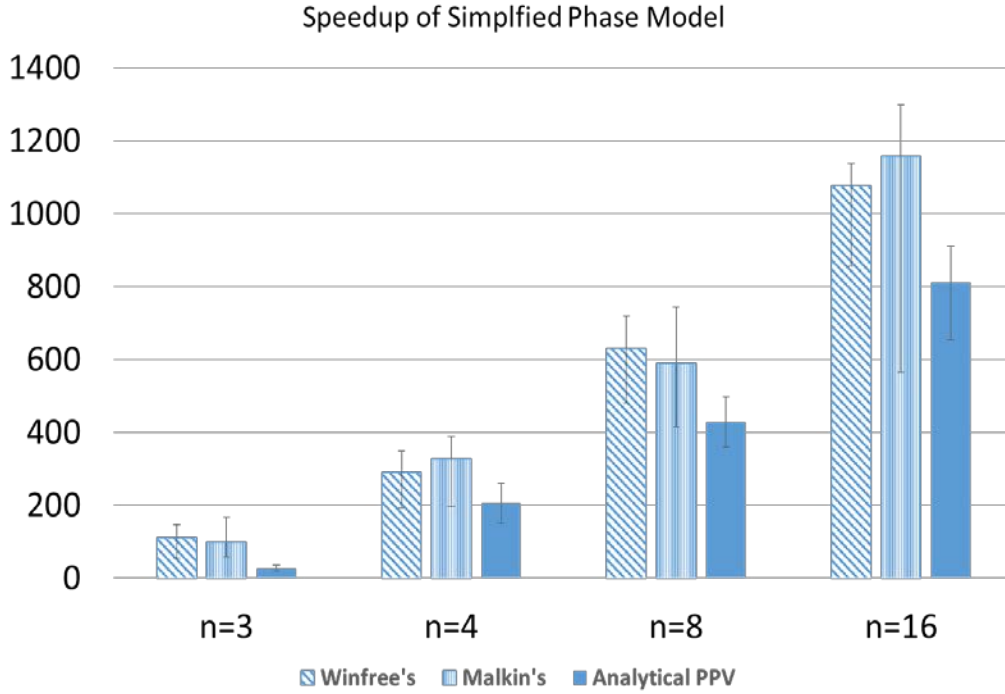


Figure 3.7 Speed-up (factor) of simplified phase model over direct simulation for different PPV/PRC methods.

3.2.3 System Level Simulation

In order to illustrate the utility of our model for system level evaluation, we give three examples of the oscillator computing paradigms discussed in Chapter 2. The first example application is a simple pattern matching task that we discussed in section 2.1.1. The goal is to recognize a handwritten digit image from the MNIST dataset, as illustrated in Figure 3.8. In this task, the stored templates are 10 averaged grayscale images from 10000 classified handwritten images in the training dataset of MNIST [50]. The image size is 784 pixels (28x28) and the pixel intensities

range from 0 to 1. Each template is the pixel-wise mean of all the images in the corresponding digits binarized with a threshold of 0.4. In our previous work, we directly used the square Euclidean distance rather than the simulation of oscillators [4]. The system was evaluated on the MNIST handwritten digit dataset and achieved 94% accuracy.

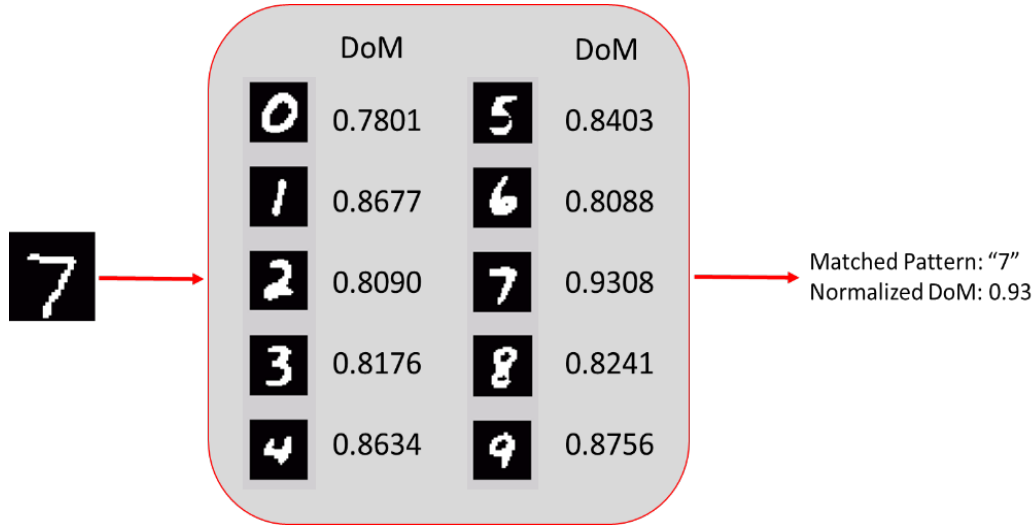


Figure 3.8 Pattern matching simulation for handwritten digit recognition and DoM from oscillator clusters.

For this simulation example, the test input pattern is a “7” randomly picked from the test dataset. We partition the 784 pixels of each image into 49 vectors of 16 pixels each and use our oscillator clusters to perform pattern matching based on these shorter vectors. The reason we partition the image vectors comes from our experiences with oscillator circuits and the challenge we foresee to practical implementations of large scale associative memories. By partitioning each vector, we can overcome the challenges of coupling a large number of oscillators in a symmetric network. For this task, we use a cluster of 17 ring oscillators like the model shown in Fig. 2.1, simulated with the analytic technique for our phase model. One oscillator that is initialized with frequency = 1 serves as the reference oscillator, meanwhile the remaining

oscillators are used to process the vector differences. The normalized oscillator frequencies range from 1 to 1.5 and the coupling coefficient is set to 0.01. Each oscillator cluster performs a 16-pixel length matching operation. Each comparison between the test image and one template requires 49 such operations, thus the total number of operations for this task is 490. Figure 3.8 gives the normalized degrees of match between the input image and the 10 templates with the correct classification. The average simulation speedup for each operation is about 780 compared to simulation with the original oscillator equations.

The second system simulation example is the image segmentation mentioned in Section 2.1.2 [37]. In this test, we generate a 16x16 grayscale image that is composed of 4 regions with different intensity ranges, as shown in Figure 3.9(a). The objective of this test is to separate each region from the others. Each region is composed of 64 randomly placed pixels with intensities from one quarter of the 0~1 range. All 256 pixels have unique intensities and thus the intensity histogram is a uniform distribution, which is difficult for those segmentation algorithms that are solely based on intensity histograms. We apply the oscillator structure given in Figure 2.4 to this task, setting the oscillator coupling strength to 0.2 and initializing the oscillator frequencies in the range of 1~2 with associated pixel intensities. When the system evolves to a stable state, the oscillators cluster into four groups by frequency, corresponding to four image regions. The central frequencies of the oscillators in these four regions shown in Figure 3.9(b) are [1.121 1.367 1.634 1.891] and the frequency band of each group is around 0.2. Thus we can obtain each segmented region by band-pass filtering the output signals of the oscillators in an associated frequency range. Figure 3.9(b) shows the segmentation results of the four regions with corresponding region numbers. This result indicates that the oscillator network is clustering the pixels based on both intensity and locality. In this simulation, the estimated speedup is about 300

for each oscillator and its neighbors compared to using the direct simulation using oscillator equations.

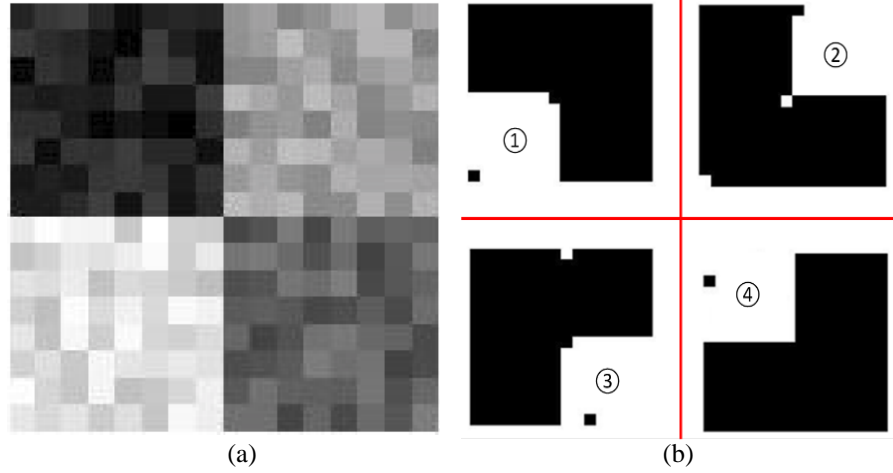


Figure 3.9 (a) Test image with four regions; (b) Segmentation results of each region from oscillator network. Each sub square is the original image with segmented region labeled as white pixels.

Our third example is a convolution operation for image filtering [36]. Figure 3.10 illustrates the process of our simulation. The test image is a 100x100 pixel grayscale “car” image (Figure 3.10 (a)). To test our oscillator based convolution model, we perform a 2-D convolution between the test image and a 5x5 Gabor filter bank with four directions (0, 45, 90, and 135 degrees). Figure 3.10 (b) displays grayscale images of these filters. Gabor filters are commonly used for edge detection and feature extraction in image processing. As we discussed in Section 2.2, the convolution of two vectors can be implemented by three oscillator clusters. In this case, each pixel in the output image is computed by the pair-wise multiplication between an image patch and a filter mask. We use three 26-oscillator clusters (each cluster has one oscillator for reference) to compute the values of $(A-B)^2$, A^2 , and B^2 . The frequency range is 1~1.5 with a relatively small coupling coefficient of 0.002. The filtered images from the oscillator system and

a 2-D convolution function in Matlab are respectively depicted in Figure 3.10 (c) and (d). We can notice that the simulation result of oscillator based convolution is very similar to the result of the Matlab function. In this operation, the approximate speedup of each operation is about 1120 compared to the direct simulation with oscillator equations.

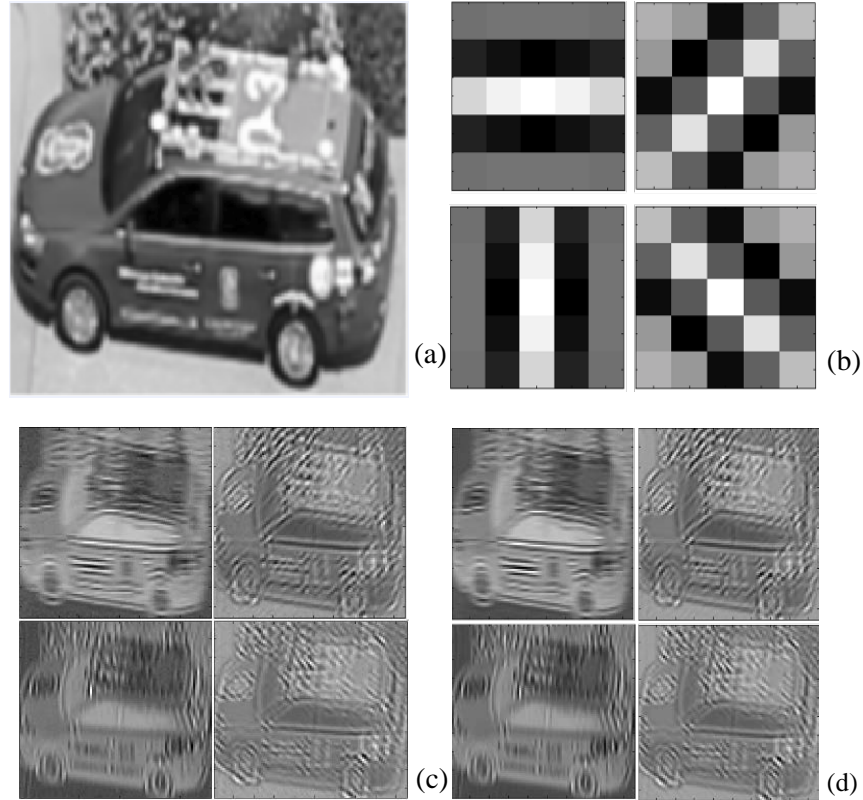


Figure 3.10 Using 5x5 Gabor filter to filter the “Car” image. (a) Test image; (b) Gabor filter bank; (c) Results from Oscillator Cluster; (d) Results from digital 2-D convolution.

These three examples of system level simulation for oscillator based computing have demonstrated that our phase model can greatly improve the simulation efficiency for large oscillator networks, while maintaining acceptable accuracy for the evaluation of these applications.

3.3 DISCUSSION

In this Chapter, we analyze previous oscillator phase models and propose a simplified phase model and apply this model to the analysis of coupled ring oscillators [14]. The results indicate that our model is capable of predicting the frequency and phase of coupled oscillator systems with small errors compared to the direct simulation of the oscillator model. We demonstrate that this model is particularly suitable for simulation and analysis for oscillator based applications such as pattern matching, segmentation, and convolution. The main contribution of our model is in simplifying the nonlinear equations and transferring simulation from the traditional time domain into the phase domain. This provides several orders of magnitude simulation speedup for large size systems.

4.0 PATTERN RECOGNITION WITH BZ-PZ OSCILLATORS

In this Chapter, we introduce the theoretical model of coupled BZ-PZ oscillator network and demonstrate its capability of performing pattern recognition through phased model simulation results. We also discuss the performance and robustness of recognition and analyze the feasibility of this hybrid material oscillator-based computing system.

4.1 THEORETICAL MODEL OF BZ-PZ OSCILLATOR NETWORK

4.1.1 Overview

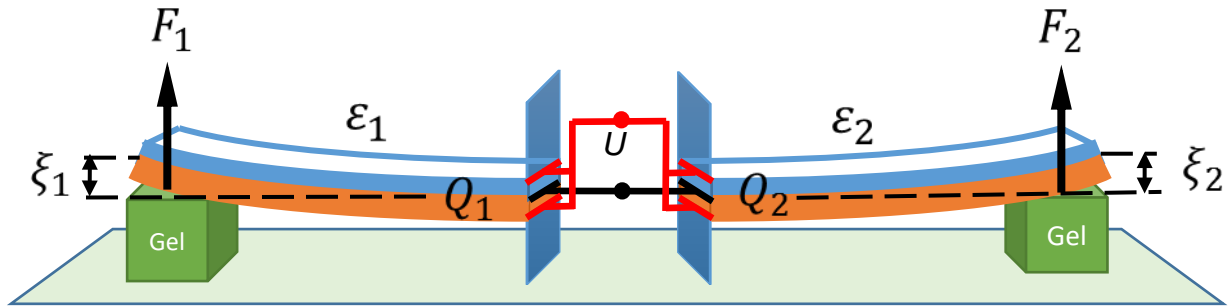


Figure 4.1 Two BZ-PZ oscillator units connected with electrical wires. Each piezoelectric cantilever consists of two identical layers of a polarized piezoelectric material; the internal and external surfaces are covered with thin electrodes connected in parallel. Periodic volumetric changes in the self-oscillating BZ gels cause rhythmic bending of the piezoelectric plates. The vector of polarization in piezoelectric bending plates is oriented perpendicular to the plate surface (not shown). The colors orange and blue are used to distinguish the two parts of a bimorph piezoelectric plate. The red and black solid lines show the electric wires connected to the external and internal electrodes, respectively. The green-colored cubes depict the BZ gels.

The fundamental unit in this system is composed of a polymer gel undergoing the Belousov-Zhabotinsky (BZ) oscillatory reaction and an overlaying piezoelectric (PZ) bimorph cantilever (see Figure 4.1). In these studies, we exploited the inherent properties of the materials to achieve the desired autonomous functionality. Namely, the BZ gels oscillate periodically without the need for external stimuli; the rhythmic pulsations are fueled by the BZ reaction occurring within the polymer network [5]. Moreover, piezoelectrics spontaneously generate a voltage when deformed, and conversely, undergo a deformation in the presence of an applied voltage. By combining these attributes into a “BZ-PZ” unit and then connecting the units by electrical wires, we designed a device that senses, actuates, and communicates without an external electrical power source. Herein, we show that device can also be used to perform computation, ultimately enabling “materials that compute”.

The operation of the simplest BZ-PZ oscillator network is illustrated in Figure 4.1, which depicts two units that are connected through electrical wires. In the course of the chemical oscillations, the BZ gels expand in volume and thereby cause the deflections ξ_1 and ξ_2 of the piezoelectric cantilevers, which give rise to an electric voltage U . Due to the inverse piezoelectric effect, the applied voltage will deflect the cantilevers, which act on the underlying BZ gels and thereby modify the chemo-mechanical oscillations in these gels. Thus, this coupling between the chemo-mechanical energy (from the BZ gels) and the electrical energy (from the deflected PZ cantilevers) enables the following functions: the components’ response to self-generated signals (sensing), the volumetric changes in the gel (actuation), and the passage of signals between the units (communication). Importantly for computation, the communication also leads to the synchronization of the BZ gel oscillators [51].

Using our theoretical and numerical models, we studied the synchronization behavior in BZ-PZ networks, and demonstrated that networks involving just a few of these hybrid oscillators could exhibit a variety of stable modes of synchronization [51]. With multiple BZ-PZ units, the oscillators can be wired into a network of arbitrary topology, formed, for example, from units that are connected in parallel or in series (see Figure 4.2). The resulting transduction between chemo-mechanical and electrical energy creates signals that propagate quickly over long distances, and thus, permits remote coupled oscillators to communicate and synchronize.

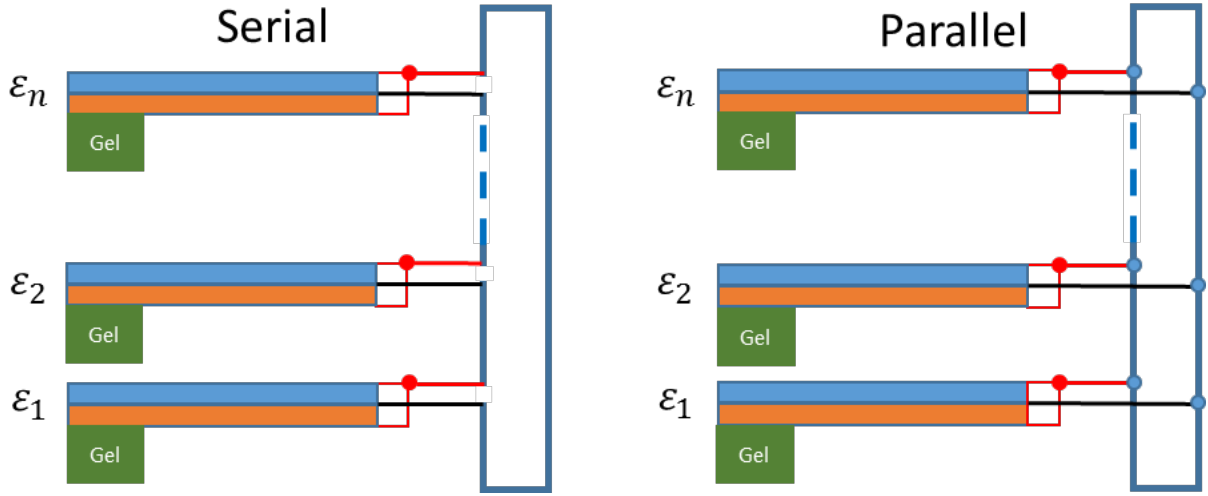


Figure 4.2 Multiple BZ-PZ oscillator units connected in serial (left) and parallel (right). $\epsilon_1, \epsilon_2, \dots, \epsilon_n$ are the force polarities of the n connected units. The orange and blue rectangles depict the two layers of a bimorph PZ plate. The green rectangles depict the self-oscillating BZ gels. The red and black lines show the electrical connections to the respective external and internal electrodes in the PZ plates.

4.1.2 Model Description

The dynamic behavior of the BZ-PZ circuits (such as those in Figure 4.1 and Figure 4.2) can be captured by coupling the equations for the volumetric oscillations of the BZ gels to the equations for the bending elasticity of piezoelectric beams [51]. Each BZ gel is assumed to be

immersed in a solution of BZ reactants under conditions required for the autonomous chemo-mechanical oscillations of the gel. Notably, millimeter-sized pieces of the gel can pulsate autonomously for hours [52]. We emphasize that the chemical energy from the BZ reaction provides the external power source in this system. Namely, this energy powers the mechanical oscillations of the gel that, in turn, prompt the deflection of the PZ cantilever, which generates the electrical voltage. This process does not occur in the absence of the reagents necessary for the BZ reaction (e.g., the chemicals in the solution and the catalyst in the gel). Moreover, the process will stop when the reagents are consumed. Importantly, however, the system can be resuscitated by adding more BZ reagents to the solution [52]. The gel size is taken to be sufficiently small that the diffusion of dissolved reactants throughout the gel occurs faster than variations of the reactant concentrations in the course of the oscillatory BZ reaction. We use a modification of the Oregonator model to describe the kinetics of the BZ reaction in terms of the concentrations of activator, u , oxidized catalyst, v , and volume fraction of polymer, ϕ [7][43]. In a system that consists of n units, the reaction kinetics for the BZ gel in each unit is given by [53][54],

$$(1 - \phi_i) d/dt [u_i (1 - \phi_i)^{-1}] = F_{\text{BZ}}(u_i, v_i, \phi_i) \quad (4-1)$$

$$\phi_i d/dt (v_i \phi_i^{-1}) = G_{\text{BZ}}(u_i, v_i, \phi_i) \quad (4-2)$$

where $i = 1, 2, \dots, n$ labels the units, and F_{BZ} and G_{BZ} are the reaction rates that depend on the concentrations u_i and v_i , and ϕ_i (see section 2.2.2).

In a BZ gel, periodic variations in the concentration of oxidized catalyst, v , due to the BZ reaction affect the polymer-solvent interactions and drive the gel's rhythmic expansion and contraction. Since small gels equilibrate in size faster than the time-scale for one oscillation of the BZ reaction, a gel's dimensions are determined by a balance among the elasticity of the

network, osmotic pressure of the polymer, and force exerted by the cantilever; this balance is expressed as follows [51][55]:

$$c_0 [\lambda_i \lambda_{\perp}^{-2} - \phi_i (2\phi_0)^{-1}] + (h_0 \lambda_{\perp})^{-2} F_i^{(g)} = \pi_{\text{FH}}(\phi_i) + \chi^* v_i \phi_i \quad (4-3)$$

The first term on the left-hand-side (l.h.s.) of (4-3) is the elastic stress within the gel that is proportional to the gel crosslink density, c_0 , and depends on the gel's degrees of swelling in the longitudinal, λ_i , and transverse, λ_{\perp} , directions. The volume fraction of polymer is calculated as $\phi_i = \phi_0 \lambda_i^{-1} \lambda_{\perp}^{-2}$, where ϕ_0 is the polymer volume fraction in the un-deformed gel. The second term in the l.h.s. of (4-3) is the pressure exerted on the gel by the cantilever, with $F_i^{(g)}$ and h_0 being the compression force acting on the gel and the size of the un-deformed gel cube, respectively. For simplicity, in (4-3), we assumed that the gel deformations are uniaxial and thus, λ_{\perp} is set to a constant value. Finally, the right-hand-side of (4-3) provides the osmotic pressure of the polymer that includes the contributions according to the Flory-Huggins theory, π_{FH} , and due to the hydrating effect of the oxidized catalyst. The strength of the hydrating effect is controlled by the interaction parameter χ^* .

The behavior of the piezoelectric cantilevers can be described by quasi-static equations because the frequency of the chemo-mechanical oscillations ($\sim 10^{-2}$ Hz) is much lower than the eigen-frequency of a cantilever ($\sim 10^4$ Hz). Applied to the cantilever in the unit i , these equations provide the deflection, ξ_i , and the electric charge, Q_i , of the piezoelectric plate as linear functions of the bending force, F_i , exerted on the cantilever and the electric potential difference (voltage), U_i , between the electrodes [56] (see Figure 4.1):

$$\xi_i = m_{11} F_i + m_{12} \varepsilon_i U_i \quad (4-4)$$

$$Q_i = m_{12}\varepsilon_i F_i + m_{22}U_i \quad (4-5)$$

The coefficients m_{11} , m_{12} , and m_{22} depend on the cantilever dimensions, material's properties of the piezoelectric, and structure of the plate, discussed in section 4.5.2. The cantilevers are considered to have a parallel bimorph structure, i.e., they consist of two identical layers of a polarized piezoelectric material with the internal and external surface electrodes connected in parallel (see Figure 4.1). The cantilevers are taken to be sufficiently thin that they are deflected by the relatively soft, expanding gels [51].

The vector of polarization in the piezoelectric bending plates is oriented perpendicular to the plate surface. The polarity of the voltage generated by the bending of the plate depends therefore on the mutual orientation of the vector of polarization and the bending force applied to the cantilever's tip in the direction normal to the surface. Equations (4-4) and (4-5) capture the latter effect through the force polarity ε_i , which has a binary value: it is equal to +1 if the direction of the vector of polarization coincides with that of the applied force, or -1 if the polarization and force are in opposite directions.

Within a BZ-PZ unit, the chemo-mechanical oscillations in the BZ gel, (4-1,2,3), and bending of the piezoelectric cantilever, (4-4,5), are coupled through the forces and displacements since $F_i^{(g)} = F_i$ and $\xi_i = (\lambda_i - \lambda^*)h_0$, where λ^*h_0 is the spatial offset between the gel and cantilever. In an isolated unit, the force $F_i^{(g)}$ acting on the gel depends only on the size of this gel, λ_i . It is assumed that the cantilever remains in contact with the gel throughout the entire cycle of gel swelling and de-swelling so that $\xi_i \geq 0$ in an isolated unit. Wiring multiple BZ-PZ units into a network leads to interactions among all the piezoelectric cantilevers and hence, the force acting on a given gel depends on the degrees of swelling (sizes) of all the gels in the system.

We assume that the connected units are identical and differ only in their force polarity. Then, the interaction between the BZ-PZ units depends only on the network topology. The strength of interaction can be determined by using (4-4) and (4-5), as demonstrated in ref [51] for the serial and parallel circuits in Figure 4.2.

Given that U_i is the voltage across the i th unit, then for units connected in series, the sum of the voltages over all n units is equal to zero, i.e., $\sum_{i=1}^n U_i = 0$. In addition, for the serial connection, the charge on each unit is equal to the total charge in the system, i.e., $Q_i = Q$. With these relationships, we calculate that bending force acting on the cantilever i can be written as

$$F_i = F_i^{(0)} + \kappa [F_i^{(0)} - \varepsilon_i n^{-1} \sum_{j=1}^n \varepsilon_j F_j^{(0)}] \quad (4-6)$$

Here, $F_i^{(0)} = m_{11}^{-1} \xi_i$ is Hook's law for a bending elastic plate, and $\kappa = m_{12}^2 (m_{11} m_{22} - m_{12}^2)^{-1}$ is the coupling strength coefficient, which is small and depends only on material properties of the cantilevers [51].

For units connected in parallel, the system obeys the following constraints: $U_i = U$ and $\sum_{i=1}^n Q_i = 0$. In this case, the bending force acting on each cantilever is

$$F_i = F_i^{(0)} + \kappa \varepsilon_i n^{-1} \sum_{j=1}^n \varepsilon_j F_j^{(0)} \quad (4-7)$$

Equations (4-6,7) show that the bending force on a given cantilever contains contributions from all BZ-PZ units in the network. The cross-terms on the right-hand-sides of (4-6,7) correspond to pairwise interactions, which depend on the force polarities, and are relatively weak since κ is small. The pairwise interactions in the serial and parallel circuits have the same magnitudes but are opposite in signs.

4.1.3 Phase Dynamics

To facilitate our investigation of the synchronization in the BZ-PZ oscillator networks, we employ the phase model described in section 2.3. This technique allows us to significantly simplify the analysis of the dynamics of the oscillator networks because the interaction between weakly coupled oscillators only results in the time-dependent deviation of phase in each oscillator. If known, the function that describes the oscillator phase response can be utilized to simulate a coupled oscillator system in the phase domain and thus, reduce the complexity of the simulation as compared to the original nonlinear oscillator equations, (4-1,2,3,4,5). For networks of identical BZ-PZ oscillators, this function was determined numerically in [51]. It was shown that the phase dynamics in the serially connected network (see Figure 4.2 and (4-6)) is described by the following equation

$$\kappa^{-1} d\varphi_i/dt = H(0) - n^{-1} \sum_{j=1}^n \varepsilon_i \varepsilon_j H(\varphi_j - \varphi_i) \quad (4-8)$$

For the parallel connection (see Figure 4.2 and (4-6)) , the phase dynamics equation is

$$\kappa^{-1} d\varphi_i/dt = n^{-1} \sum_{j=1}^n \varepsilon_i \varepsilon_j H(\varphi_j - \varphi_i) \quad (4-9)$$

The oscillation phase normalization in (4-9) is such that $0 \leq \varphi_i \leq 1$, $i = 1, 2, \dots, n$. The function $H(\varphi_j - \varphi_i)$ (connection function) characterizes the rate of the phase shift for the oscillator i due to the interaction with the oscillator j at their relative phase difference of $\varphi_j - \varphi_i$. The connection function $H(\theta)$ is periodic at $\theta \in [0, 1]$, and determined by the intrinsic properties of the oscillators described by (4-1,2,3).

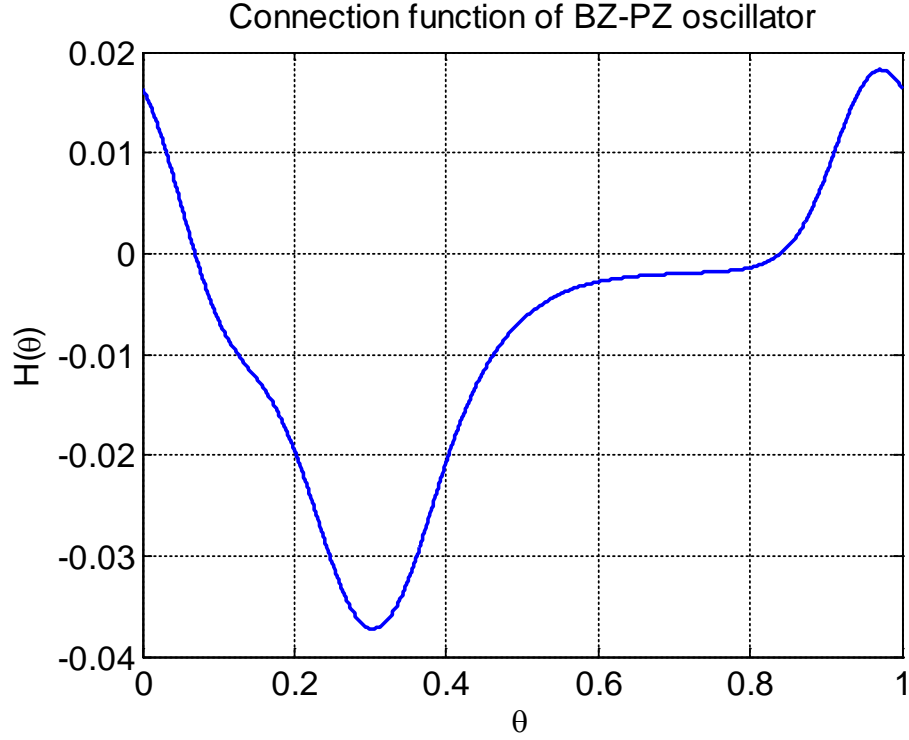


Figure 4.3 The connection function $H(\theta)$ used in the equations of the phase dynamics, (4-8,9). The connection function is periodic at $\theta \in [0,1]$.

Figure 4.3 shows the plot of the connection function obtained in [51]. It is evident that the phase response of a BZ-PZ oscillator to an external action is quite complicated. The interaction between the oscillators can cause both positive and negative phase shifts depending on the phase difference, and this results in a variety of stable phase synchronization modes exhibited by the BZ-PZ oscillator networks [51]. For any set of initial phases for the individual oscillators, the system dynamics converges to one of the stable synchronization modes.

4.2 SYSTEM CONFIGURATION FOR PATTERN RECOGNITION

The coupled BZ-PZ oscillator networks can achieve both in-phase and anti-phase synchronization, depending on the initial phases, connection type, and force polarity of each oscillator unit [51]. By specifying these conditions, the network can exhibit particular modes of synchronization. Below, we discuss how the synchronization dynamics in the BZ-PZ could be employed for pattern recognition tasks.

Inspired by the Oscillator Neural Network model [31], we propose a similar computing paradigm for networks of coupled BZ-PZ oscillators. We specifically focus on BZ-PZ oscillators that are connected in series. Figure 4.4 illustrates how we transcribe a black and white image into this serially connected network. Each oscillator unit represents one pixel of the image and we specify the polarity of the PZ cantilever in each unit according to the color of the image. In particular, we assign the polarity the value of +1 for a white pixel and -1 for a black pixel. Rastering through the n pixels in the image (going from left to right), we assign a value of the polarity to each of the n oscillators according to the color of the pixel. In the device, the desired force polarities can be achieved by flipping the connecting wires; this changes the sign of the voltage generated by a BZ-PZ unit.

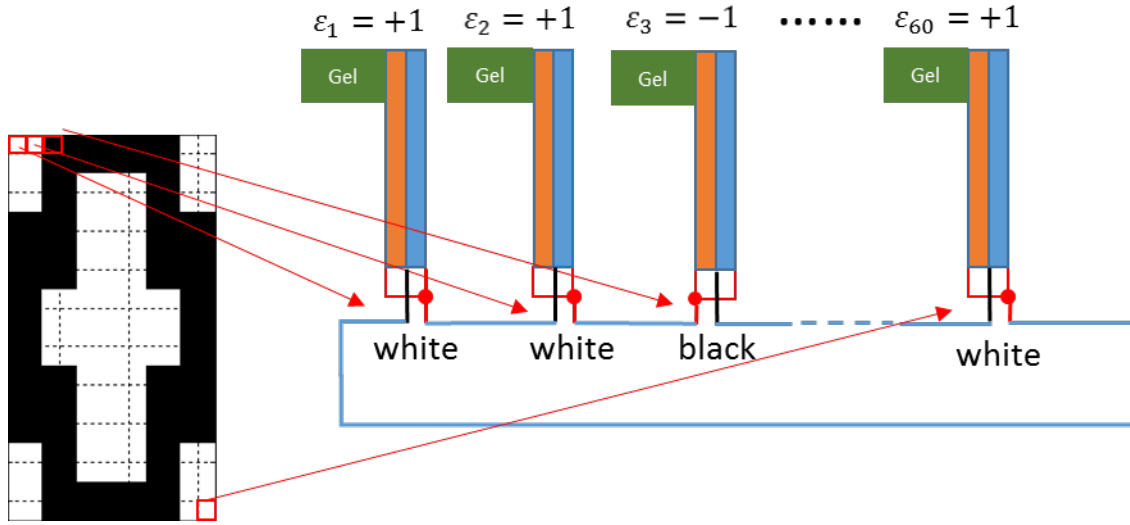


Figure 4.4 Schematics indicating how to transpose a black and white image onto the serially connected network of the BZ-PZ oscillators. Here, we store a binary image of the digit ‘0’ that contains 60 pixels. The force polarity of an oscillator is set to $+1$ for a white pixel and to -1 for a black pixel. Note that assigning $\varepsilon_3 = -1$ is achieved through flipping the red and black connector wires.

Our rationale for the above procedure is based on our findings for the synchronization of three BZ-PZ oscillators connected in series [51]. For a serial circuit of three oscillators having different force polarities, *e.g.*, $\{+1, +1, -1\}$, the only stable mode of synchronization corresponds to the in-phase synchronization (no phase difference) of the $+1$ units, which, in turn, are synchronized anti-phase (phase difference 0.5) with the -1 unit. Note that all phases are normalized to vary between 0 and 1. Based on extensive numerical simulations and a linear stability analysis (section 4.4), we conjecture that multiple BZ-PZ units connected in series exhibit a stable synchronization mode characterized by the in-phase synchronization of all the oscillators that have the same polarity, and the anti-phase synchronization with oscillators of different polarity.

There is an important difference between the ONN model and the BZ-PZ network shown in Figure 4.4. Namely, in the ONN model, the coupling weights of oscillators are real numbers assigned according to the Hebbian learning rule that makes storing multiple patterns possible [32]. In contrast, the force polarity factors in our oscillator network can only be a binary value, $+1$ or -1 , so that each oscillator network is expected to store a single pattern. Hence, in this work, we define the pattern recognition task as retrieving one pattern that is closest to the pattern stored in the system from multiple input patterns.

To initiate the recognition process, an input pattern is used to initialize the phase φ of each oscillator in the network, with $\varphi = 0$ for a black pixel and $\varphi = 0.5$ for a white pixel (see Figure 4.4). Notably, the dynamics of the BZ gels are chemo-, photo- and mechano-responsive [11][55] and hence, the initial variations in phase among the units can be introduced by local applications of chemical stimulation, light or pressure.

After the initialization, the system evolves the phases into some stable state, transforming the input pattern to some other pattern. As detailed below, our simulations reveal that an input pattern evolves to the stored pattern, which is defined by the set of force polarities. Importantly, the rate of convergence of the input image to the stored image depends on the similarity between the two images. “Convergence” means that the oscillators representing the black pixels in the stored pattern establish the in-phase synchronization amongst themselves, and the anti-phase synchronization with the oscillators that represent the white pixels. As detailed in the SI, we confirm the stability of the state of synchronization imposed by the stored pattern by using a linear stability analysis.

Figure 4.5 illustrates the pattern recognition task performed by three different BZ-PZ oscillator networks, which store the respective images for the digits ‘0’, ‘1’, and ‘2’. The

networks are simultaneously initialized with the same distorted ‘1’ test image. Namely, the test image is used to set the initial phases of the pixels, as noted above. In the panels on the left, we show the temporal evolution in the systems by plotting the phase differences between the first oscillator and all the other oscillators (in the given system) as a function of time. The phase differences are plotted in the range from 0 to 0.5, which correspond to the in-phase and anti-phase synchronization, respectively. In the panels on the right, the first image represents the initial input pattern and the temporal evolution of the networks is displayed through a sequence of images for the first 60 units of time; the interval between the images is equal to 10 time units. The unit of time is $\kappa^{-1}T_0 \sim 5 \text{ min}$, where $\kappa \approx 0.2$ is the strength of coupling (see eq. (6)) and $T_0 \sim 1 \text{ min}$ is the period of oscillation of the un-coupled oscillators. Figure 4.5 reveals two important results. First, all these three networks converge to their own stored pattern. Second, the network that stores the number ‘1’ converges faster than the other two systems. In other words, the network storing the image ‘1’ provides the best match between the input and stored pattern, and hence, is the “winner” in the recognition task.

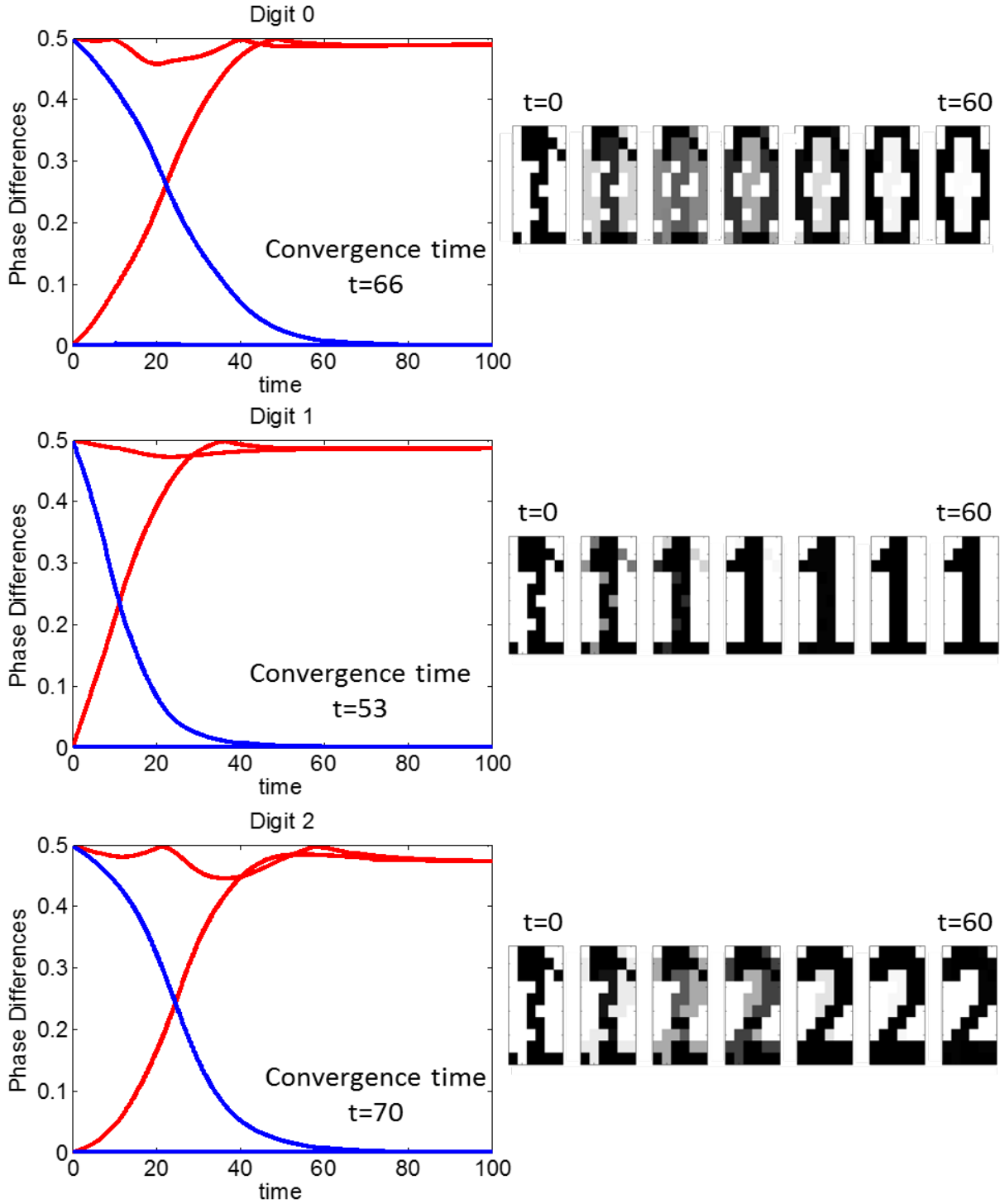


Figure 4.5 Illustration of the pattern recognition task. The three different BZ-PZ oscillator networks, which store the respective images for the digits '0', '1', and '2', are initialized with the same distorted '1' input image. The phase differences of the oscillations in the networks converge to the respective stored patterns in the course of synchronization. The blue and red lines distinguish between the two groups of oscillators that converge to the phase difference of 0 and 0.5, respectively. The convergence is the fastest in the network exhibiting the best match between the input and stored pattern, i.e., in the network that stores the digit '1'.

The results shown in Figure 4.5 suggest that the convergence time can serve as an DoM that measures the differences between the input pattern and each stored pattern. Hence, a system consisting of multiple BZ-PZ oscillator networks can recognize patterns by detecting the shortest convergence time among the networks [4][26]. To support this hypothesis, we conducted multiple computational tests discussed in the next section.

As noted above, the initial input patterns can be introduced into the network by setting the phases of oscillation in the individual BZ gels through chemical, optical or mechanical techniques [11]. Another method for storing patterns is to take the advantage of the coupled oscillator network dynamics. Since each oscillator network evidently converges to the pattern set by the force polarities, we can set the oscillator force polarities with the input pattern vectors in the same way as we set the stored patterns. Once the network phases become stable to the phases corresponding to the input test pattern, we switch the force polarities to the stored pattern and then measure the convergence time to this stored pattern.

4.3 PERFORMANCE AND ROBUSTNESS

In this section, we discuss various computer simulations designed to analyze the synchronization of coupled BZ-PZ oscillators connected in series, and demonstrate that the convergence time of coupled oscillator networks does indeed provide a robust measure of pattern recognition.

We conduct the following three sets of computer simulations focused on measuring and comparing the convergence times obtained with different test patterns and stored patterns. First, we explore how the convergence time of a network is related to the difference between the input pattern and the stored pattern (Test 1). Second, we test the capability of two independent

networks to discriminate between two stored patterns with the “cross-pattern” test (Test 2). Finally, we apply the coupled oscillator network to the recognition task for images of the digits 0 to 9 and analyze the recognition performance and robustness (Test 3).

For all these tests, we define the convergence time of synchronization as the number of time units, $\kappa^{-1}T_0$, needed for the coupled oscillators to reach the stable state of synchronization that represents the stored pattern. Specifically, in this stable state, the phase difference values of oscillators are separated into two groups representing the black and white pixels, with each oscillator’s phase being within 1% of the group average.

4.3.1 Distance Metric and Convergence Time

In Test 1, we first demonstrate that the time for convergence depends on the similarity between the stored and input patterns. For this purpose, we compare the convergence time to the Hamming distance, which is the sum of the element-wise differences between two binary vectors. This parameter is a quantitative measure of the total difference between given images of the same size. Note that the phase dynamics and synchronization mode for the mirror (bit complement) pattern are indistinguishable from those for the original pattern; this can be seen from (4-9), where the r.h.s. of the equation does not change when the sign of all the force polarities are altered simultaneously. Therefore, we effectively consider a stored pattern and its mirror pattern in a single network.

To vary the Hamming distance between a given stored pattern and an input, we start with the copy of the stored pattern and generate input patterns by flipping an increasing number of pixels until the input pattern is transformed into the mirror pattern. In this procedure, the input

patterns are gradually less similar to the stored pattern and more similar to the mirror pattern, as illustrated in Figure 4.6. For the stored pattern shown in Figure 4.6, the Hamming distance between the stored and mirror patterns is 99. The Hamming distance between the input pattern and one of the stable states of the system changes consecutively as 1, 2, ..., 49, 50, 49, ..., 2, 1.

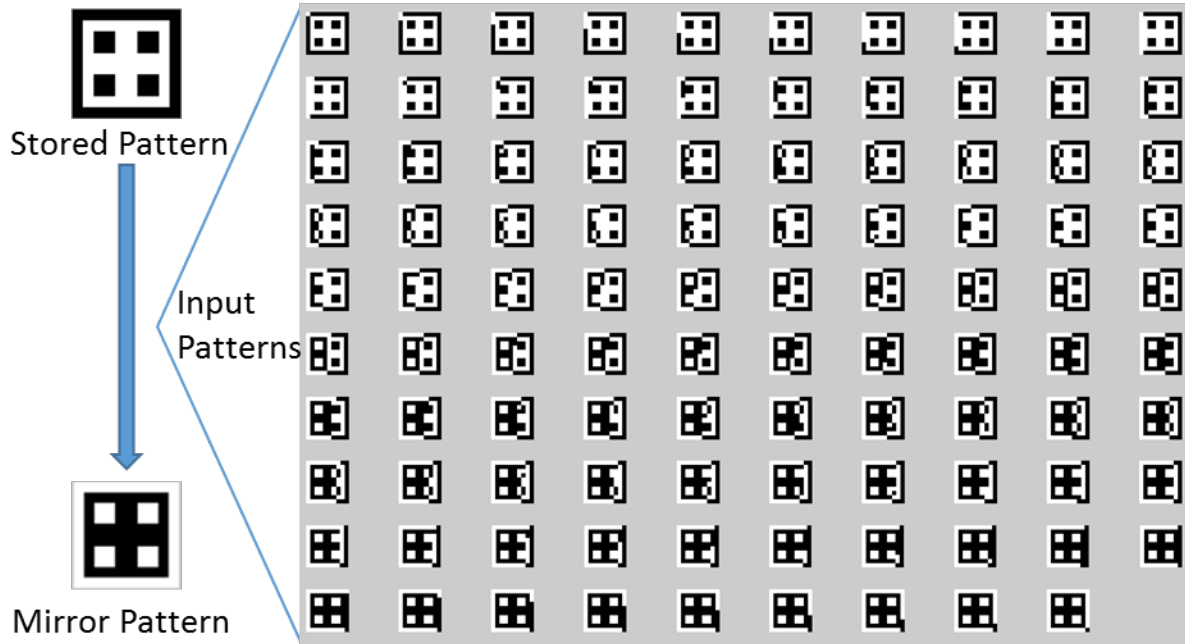


Figure 4.6 The stored 10x10 pattern and an example of the input pattern set used in Test 1. The set is generated by flipping an increasing number of pixels until the input pattern is transformed into the mirror pattern. The difference between the stored pattern and an image from the set is characterized by the Hamming distance, which is the sum of the element-wise differences between two binary vectors.

The images in Figure 4.6 represent only one particular sequence of input patterns characterized by the above set of Hamming distances to the stable states. In Test 1, for a given Hamming distance, the bits to be flipped are selected randomly, and the convergence time is averaged over 100 runs, so that 99×100 input patterns were tested for convergence. The comparison between the obtained convergence time and Hamming distance is shown in Figure 4.7. Figure 4.7 clearly indicates that the time for the coupled oscillator network to

synchronize follows the trend of the difference between input and stored patterns, so that the convergence time decreases with a decrease in the Hamming distance. (The convergence time decreases after 50 bits have been flipped because, as noted above, the phase dynamics and synchronization mode for the mirror and stored pattern are indistinguishable.) In other words, the convergence time provides a robust measure of the degree of match between the input and stored patterns.

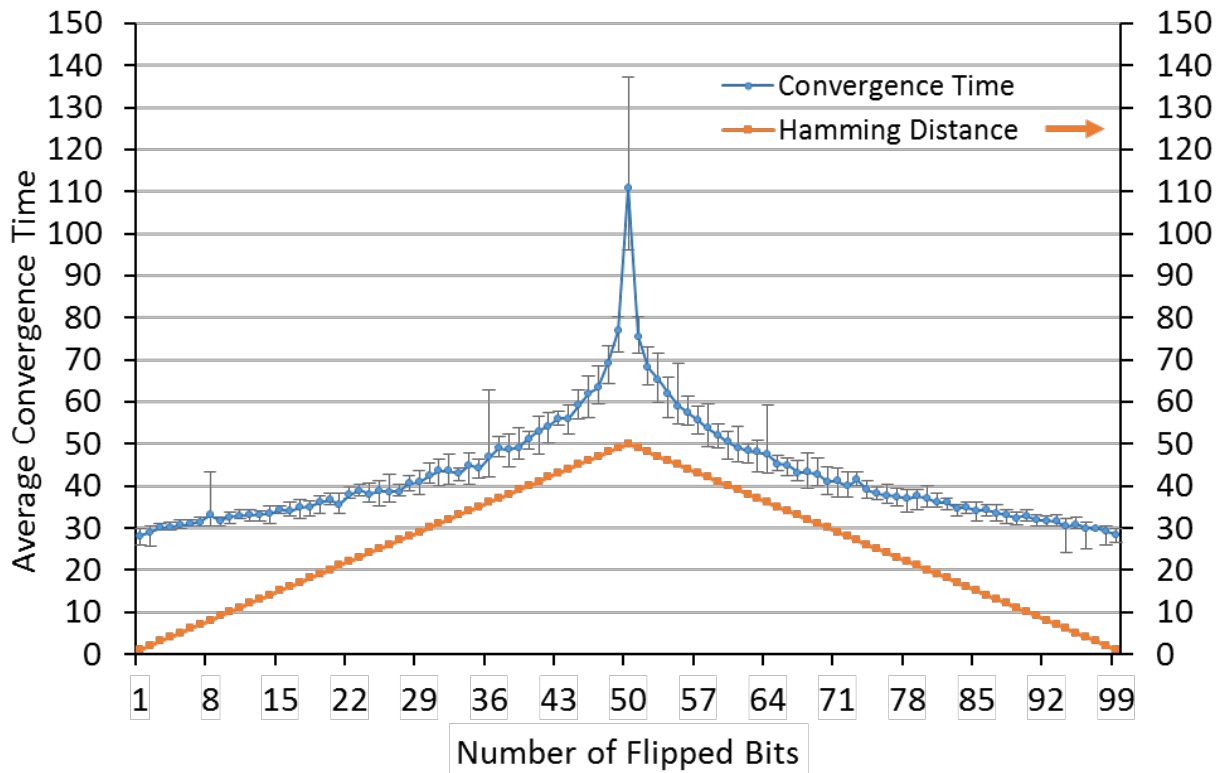


Figure 4.7 The average convergence time obtained in Test 1 (blue line), and the Hamming distance between the stored and input images (orange line) as functions of the number of flipped bits. The error bars show the range of convergence times obtained from 100 runs at a given number of flipped bits, which were selected at random from all the bits in the system.

4.3.2 Cross-Pattern Test

In the cross-pattern simulations, Test 2, we explore the ability of our system to discriminate between two distinct patterns. In this test, we choose the two patterns, p_1 and p_2 shown in Figure 4.8, and store them in two oscillator networks. They share some bit values at certain pixel positions and differ at the others. We label p_0 as the set of pixels where p_1 and p_2 share the same values, and p_x as the set of pixels where they differ from each other. To generate the input patterns, we employ the same strategy of flipping bits as in Test 1. Specifically, we select pixel positions from p_x and set them to the value in p_2 so that the input pattern gradually evolves from p_1 to p_2 . As in Test 1, for each number of pixels, the random selection is repeated 100 times.

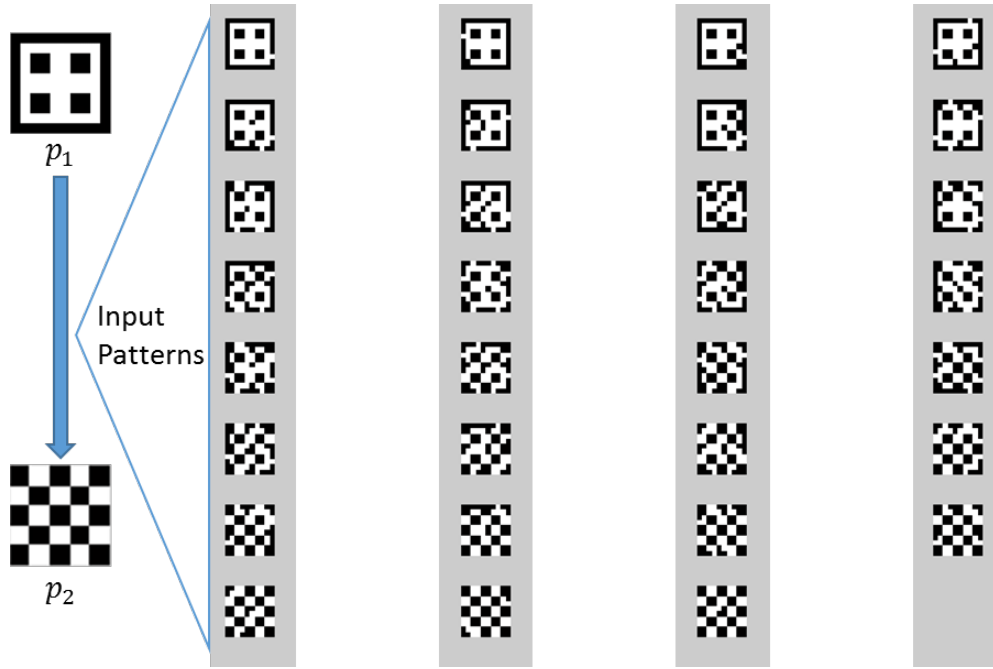


Figure 4.8 An example of the 10×10 stored and input patterns used in Test 2. The input patterns are generated using the same strategy of flipping bits as in Test 1.

Every input pattern is applied to both networks (p_1 and p_2) so that their convergence times can be compared. The number of different bits, the size of $p_x p_X$, is 32; thus, we generate 31 sets of input patterns. Figure 4.9 presents the comparison of convergence times to the stored patterns $p_1 p_1$ and $p_2 p_2$. As the input patterns evolve from $p_1 p_1$ to $p_2 p_2$, the convergence time to $p_1 p_1$ increases while the convergence time to $p_2 p_2$ decreases. The results indicate that we can use the convergence time to determine which stored pattern is close to the input pattern. It is only when the input pattern is equally similar to both stored patterns (within a few bits) that the system fails to identify which one is closer.

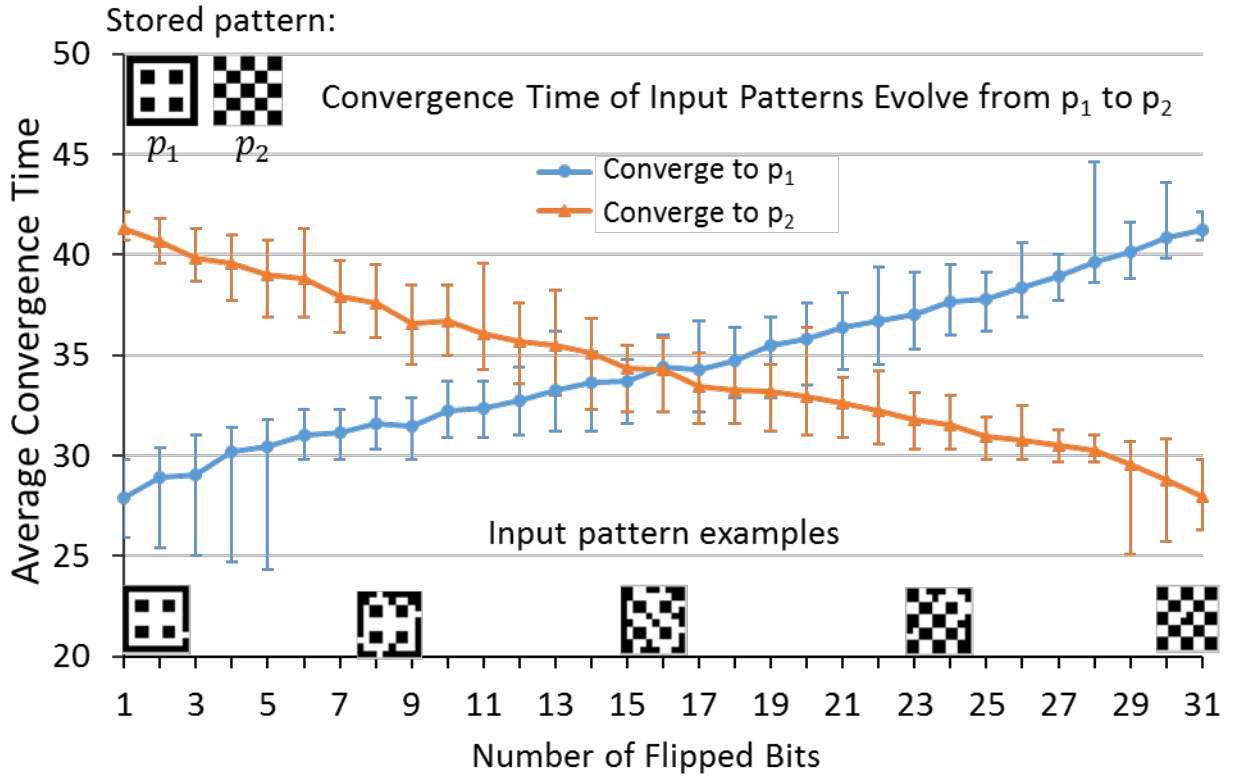


Figure 4.9 The average times of convergence to the stored patterns p_1 (blue line) and p_2 (orange line) obtained in Test 2 as functions of the number of flipped bits. The error bars are obtained as described in Figure 4.7.

In the cross-pattern test shown in Figure 4.9, the size of $p_x p_X$ is less than half of the total number of pixels in the image. If we select $p_1 p_1$ and $p_2 p_2$ with a larger value of $p_x p_X$, the two stored patterns become more similar to each other's mirror pattern and the convergence time should be affected. To demonstrate this point, we perform the cross-pattern test on two different stored patterns where the size of $p_x p_X = 63$. Figure 4.10 shows the images of the two chosen patterns, and the convergence times to both $p_1 p_1$ and $p_2 p_2$ as functions of the number of flipped bits. The latter plot reveals that as the pattern distances continue to increase, the curves are no longer monotonic. The reason for this behavior is due to the presence of the mirror pattern in each network. For example, the convergence time to $p_1 p_1$ increases monotonically as the input patterns become less similar to $p_1 p_1$. However, since the size of $p_x p_X$ is large, after 45 pixels have been flipped, the input patterns become increasingly similar to the mirror pattern of $p_1 p_1$. Therefore, these input patterns actually converge to the mirror pattern of p_1 ; this behavior was also observed in Figure 4.7, the result of Test 1. Importantly, however, even with the interference of the mirror patterns, the two stored patterns can be distinguished from each other because the convergence times are distinct for the two samples, except at a few points (between 30 and 32 flips on the x -axis).

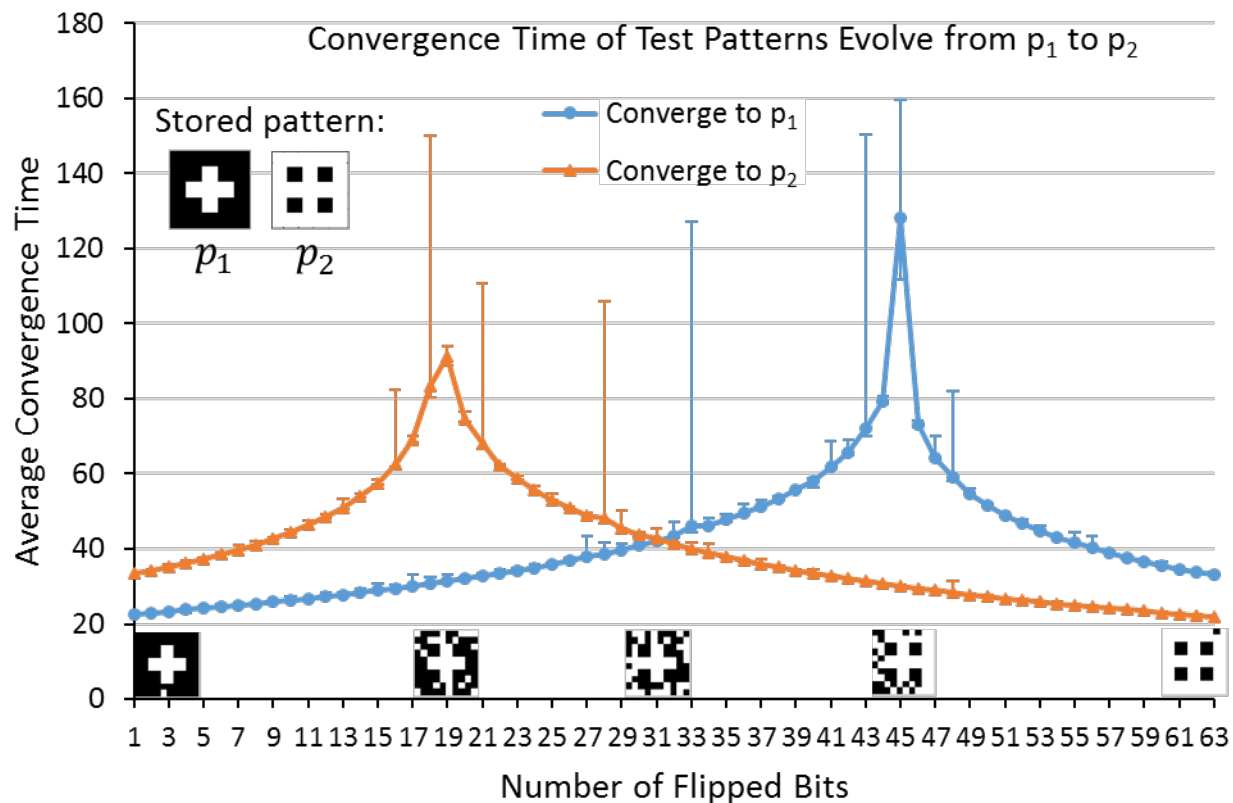


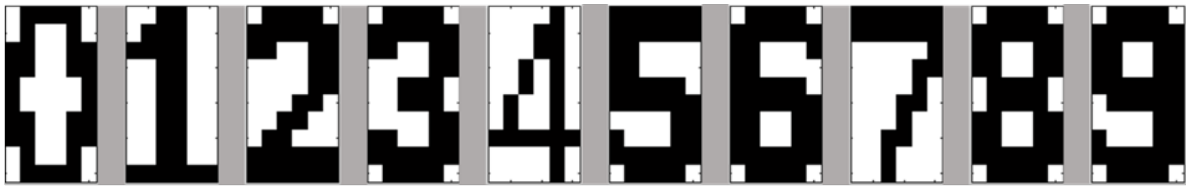
Figure 4.10 The average times of convergence to the stored patterns p_1 (blue line) and p_2 (orange line) obtained in Test 2 as functions of the number of flipped bits. The two stored patterns are more similar to each other's mirror patterns than the stored patterns in **Figure 4.8**. The observed peaks are similar to the one in **Figure 4.6**, the result of Test 1.

4.3.3 Recognition Performance Under Noise

Finally, in Test 3, we examine the performance of our coupled oscillator network on a pattern recognition task that is expanded from the one shown in **Figure 4.5**. Now, the stored patterns are 60 pixel binary images of digits '0' to '9' (see **Figure 4.11**). The input patterns are distorted images of each digit, with noise that is generated by randomly flipping bits. The degree of added noise increases gradually in the recognition tests, as 1, 5, 10, 15, 20, 25, and then 30 pixels are randomly selected and flipped from the original digit images; here we perform 100 simulations for each case. **Figure 4.11** shows not only the stored patterns, but also provides examples of the

input patterns for distorted images of digits ‘3’ (Figure 4.11b) and ‘8’ (Figure 4.11c). In each convergence simulation, we impose an input pattern onto 10 networks of 60 coupled oscillators; each network stores one image of a digit. A network recognizes the input pattern yielding the shortest convergence time, which corresponds to the highest DoM. If the winner is the same digit as the original digit of the noisy input pattern, the recognition is a hit, otherwise it is a miss.

(a) Stored patterns of digits 0~9



(b) Input patterns of ‘3’ with increasing noise



(c) Input patterns of ‘8’ with increasing noise

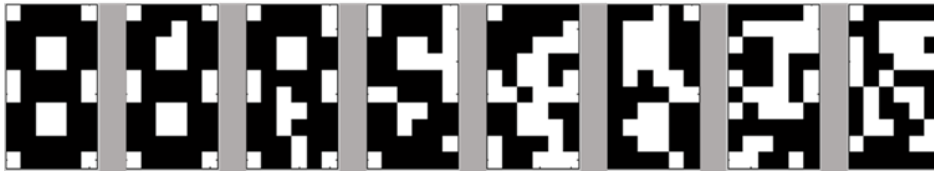


Figure 4.11 The images used in Test 3. The top row (a) shows the 10x6 binary images of the ten digits used as the stored patterns. Rows (b) and (c) show the respective distorted image of the digit ‘3’ and ‘8’ that are obtained by flipping 1, 5, 10, 15, 20, 25, 30 pixels that are randomly selected.

Figure 4.12 is a bar graph of the recognition accuracy for the cases of ten stored digit patterns. As the noise increases, the recognition accuracies decrease. The cases of 30 flipped bits are not shown because when half of the bits are flipped, the recognition accuracies drop to zero. The reason for the latter behavior is that the input patterns for these cases are actually further

from the original digit pattern than they are from the others. Among the four patterns shown here, '3' produces the worst recognition performance because this digitized image is very close to '6', '8', and '9' with very few different pixels.

Further, each column in Figure 4.13 represents the difference between the convergence times for the winner and the runner-up for all the hit cases. The height of the column is a measure of the robustness of the recognition task; the data is plotted for the different degrees of noise. The results indicate that when the degree of noise is increased, the time lag between the runner-up and the winner becomes shorter and hence, it becomes more difficult for the oscillator system to differentiate the correct pattern in an efficient manner.

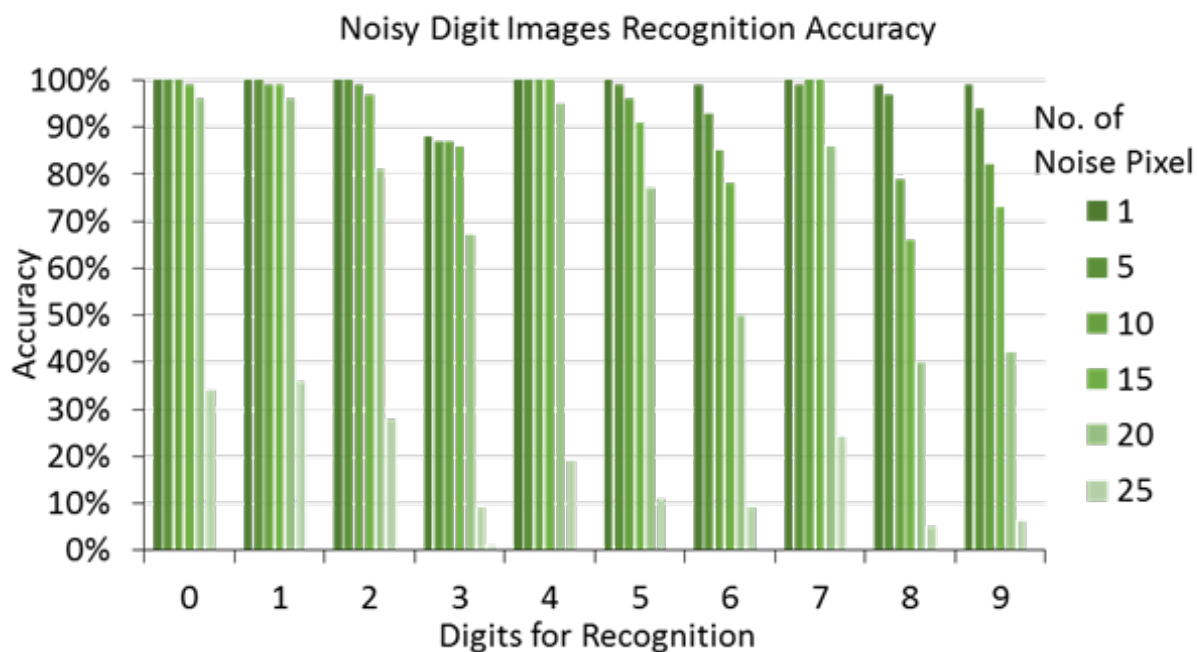


Figure 4.12 The accuracies of the recognition Test 3 for the input patterns of all the digits that are distorted with various levels of noise. The bars are colored according to the noise level. The horizontal axis indicates the input patterns.

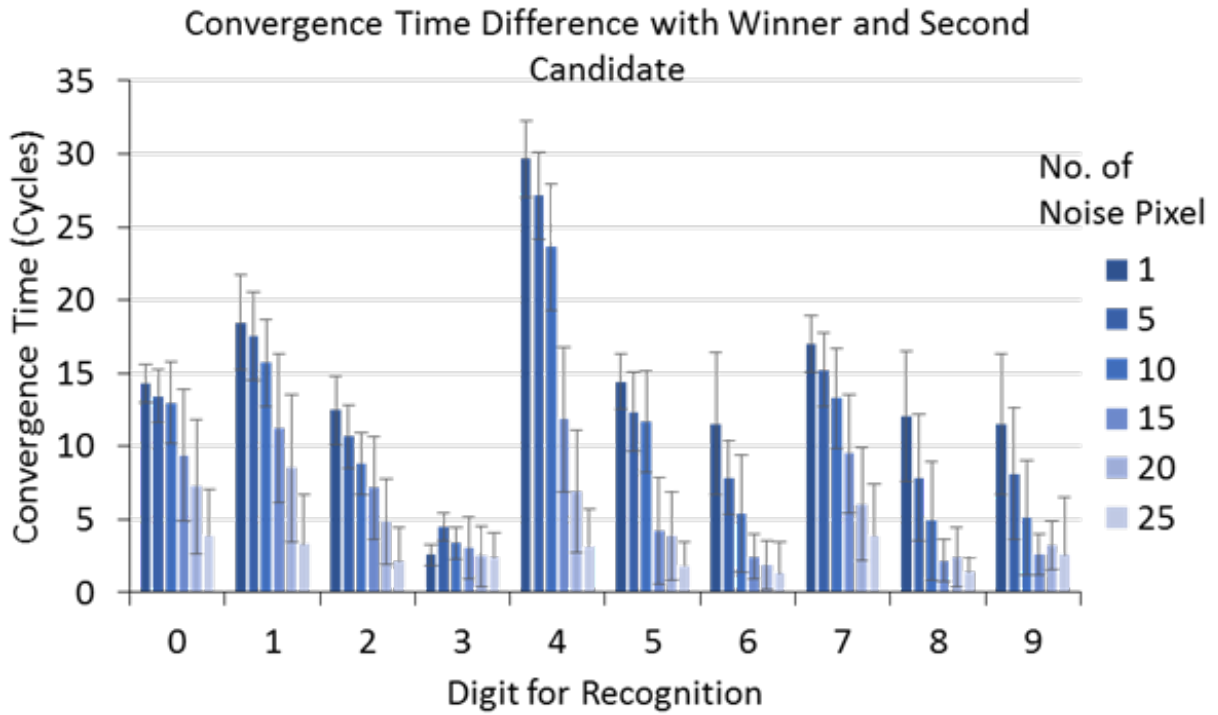


Figure 4.13 The difference between the average convergence times of the winner and of the runner-up in all the hit cases in Test 3 for the digits shown in **Figure 4.12**. The error bars show the standard deviation obtained for each bar. The results indicate how fast the correct, recognized winner leads the runner-up. The other notations are the same as in **Figure 4.12**.

4.3.4 Effect of Gel Heterogeneities on Synchronization

Within our model for the BZ-PZ system, it is assumed that all the BZ-PZ units are chemically and physically identical. The effect of variations in the properties of the individual oscillators, however, can be estimated within the phase dynamics approach. Specifically, we consider a network of BZ-PZ units where the periods of the free-running oscillations vary around T_0 due to heterogeneities among the units. The dynamics of this system is described by the following generalization of (4-8)

$$d\varphi_i/dt = \Delta T_i / T_0 + \kappa H(0) - \kappa n^{-1} \sum_{j=1}^n \varepsilon_i \varepsilon_j H(\varphi_j - \varphi_i) \quad (4-10)$$

where $\Delta T_i = T_i - T_0$ is the detuning of oscillator i . We assume that the relative variation of the period of oscillation, $\Delta T / T_0$, is a uniformly distributed random value within the interval $[-\sigma, \sigma]$, and perform simulations at various values of the distribution width σ . Figure 4.14 shows the results of the simulation for the evolution of the input pattern corresponding to the distorted digit “1” towards the stored pattern “2” (see Figure 4.5, third row) at four values of σ . When σ equals 0.001κ and 0.002κ , the synchronization dynamics is similar to that in the case of the identical oscillators. The only effect of the heterogeneity is a “widening” of the two final states of synchronization, i.e., the phases are grouped within narrow bands around the phase differences 0 and 0.5. A further increase of the distribution width to $\sigma = 0.005\kappa$ makes the recognition problematic, and the recognition is impossible at $\sigma = 0.01\kappa$.

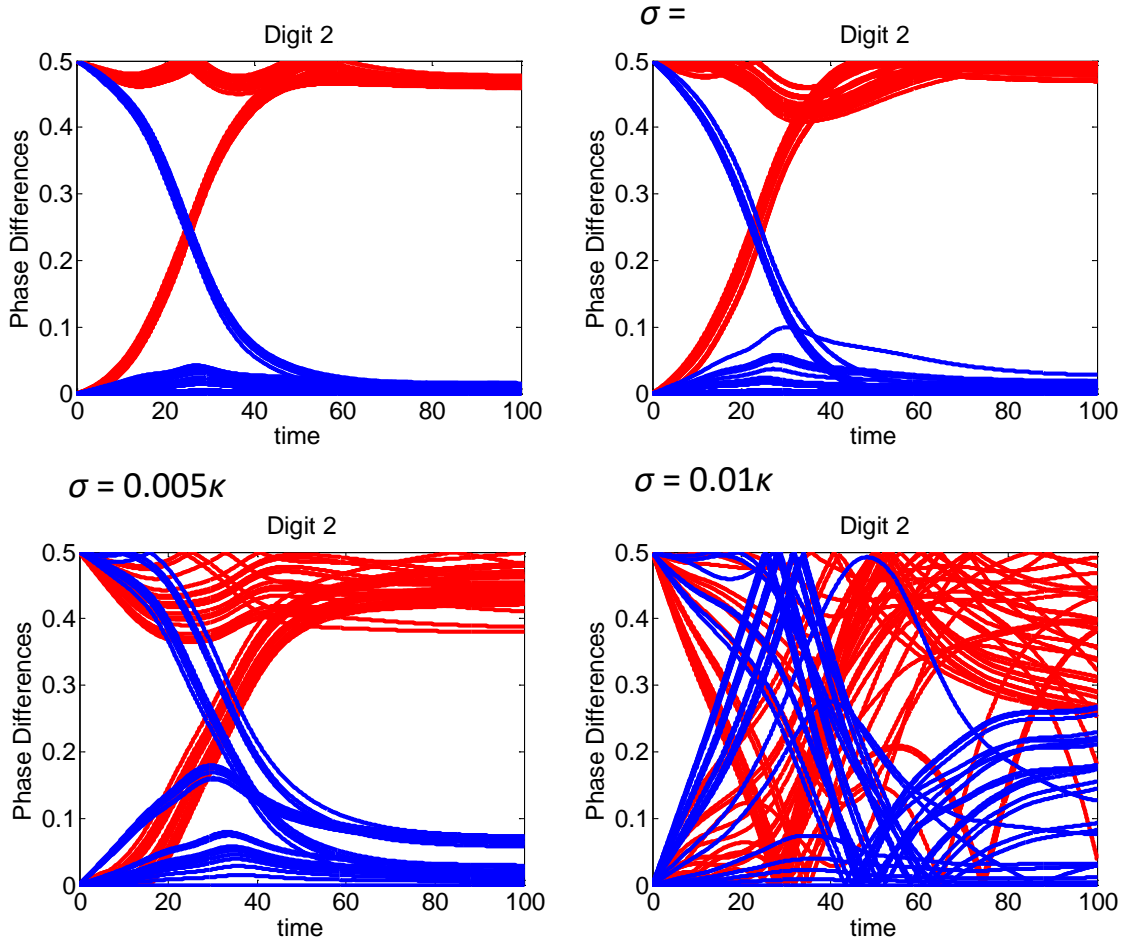


Figure 4.14 The phase dynamics for the uniform distribution $\Delta T/T_0 \in [-\sigma, \sigma]$ for various values of σ .

The criterion of convergence used for the pattern recognition should be adjusted depending on the magnitude of variations in $\Delta T/T_0$. The latter observation is evident from Figure 4.15, which shows an increase in the scattering of the convergence times resulting from an increase in the distribution width σ from $1 \times 10^{-4}\kappa$ to $2 \times 10^{-3}\kappa$. Here, we set the convergence threshold to 0.1 (each oscillator's phase is within 10% of the group average), which is 10 times greater than the value used for the studies described in the main text.

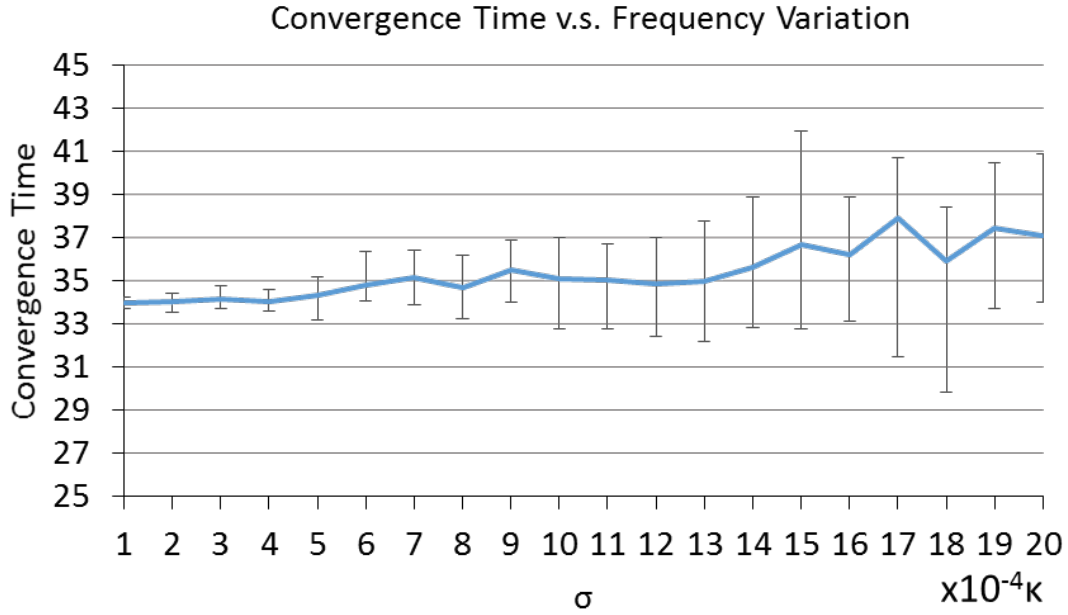


Figure 4.15 The convergence time at random $\Delta T / T_0 \in [-\sigma, \sigma]$ as a function of the distribution width σ . The convergence threshold is 0.1.

4.4 SYNCHRONIZATION MODE STABILITY

In this section, we use the linearization approach to show that the synchronization mode used for the pattern recognition is stable. We consider a system of n serially connected BZ-PZ oscillator units; n_1 of these units have force polarities of $+1$ and the remaining $n_2 = n - n_1$ units have force polarities of -1 . The equation of phase dynamics (4-8), is invariant under a renumbering of the units so we assign the polarity $+1$ to the units $i = 1, 2, \dots, n_1$, and the polarity -1 to the units $j = n_1 + 1, n_1 + 2, \dots, n$. The application of eq. (8) to the two groups of units gives the following equations of phase dynamics:

$$\kappa^{-1} d\varphi_i/dt = H(0) - n^{-1} \sum_{k=1}^{n_1} H(\varphi_k - \varphi_i) + n^{-1} \sum_{l=n_1+1}^n H(\varphi_l - \varphi_i) \quad (4-11)$$

$$\kappa^{-1} d\varphi_j/dt = H(0) + n^{-1} \sum_{k=1}^{n_1} H(\varphi_k - \varphi_j) - n^{-1} \sum_{l=n_1+1}^n H(\varphi_l - \varphi_j) \quad (4-12)$$

We assume that upon synchronization, the oscillators are synchronized in-phase within each group, and that the difference in phase of oscillation between these two groups is ψ . By substituting $\varphi_i = \nu t$ and $\varphi_j = \nu t + \psi$ to eqs. (4-11,12), we obtain the following equations for the constant shift in the frequency of oscillation ν and the phase difference ψ that characterize the state of synchronization:

$$n\kappa^{-1}\nu = n_2[H(0) + H(\psi)] \quad (4-13)$$

$$n\kappa^{-1}\nu = n_1[H(0) + H(1 - \psi)] \quad (4-14)$$

Equation (4-14) is written with taking into account that the connection function $H(\theta)$ is periodic so $H(-\psi) = H(1 - \psi)$. Subtraction of (4-14) from (4-13) yields the equation for the phase difference:

$$(n_2 - n_1)H(0) + n_2 H(\psi) - n_1 H(1 - \psi) = 0 \quad (4-15)$$

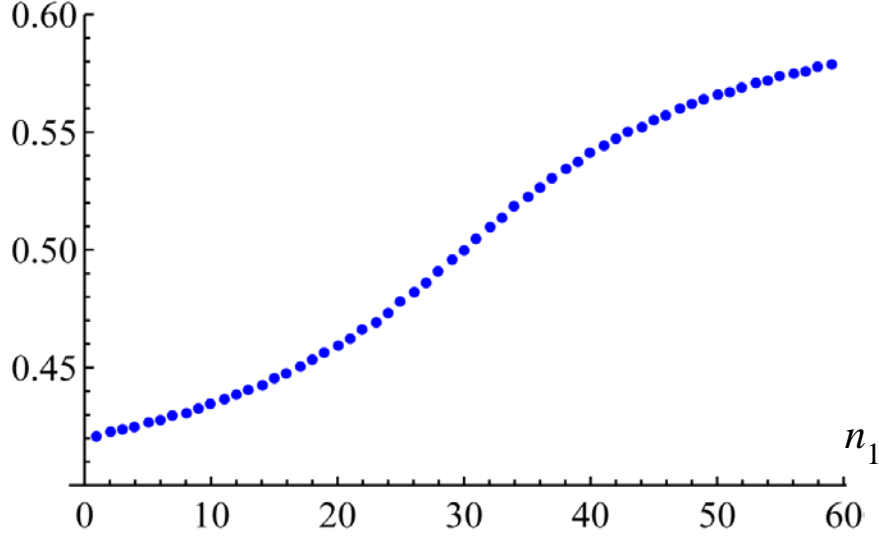


Figure 4.16 The phase difference ψ between the two groups of oscillators obtained by numerical solution of (4-15) at $n=46$.

The connection function $H(\theta)$ is known (see Figure 4.3) so the phase difference ψ can be found by numerical solution of (4-15). Figure 4.16 shows the calculated values of ψ as a function of n_1 at $n = 60$.

In order to study the stability of the synchronization state, we introduce the phase difference between the oscillator $i = 2, \dots, n$ and the oscillator 1, $\theta_i = \varphi_k - \varphi_1$, and use (4-11,12) to obtain the equations for θ_i . For $i = 2, \dots, n_1$, the equation is

$$n\kappa^{-1}d\theta_i/dt = -[H(-\theta_i) - H(\theta_i)] - \sum_{\substack{k=2 \\ k \neq i}}^{n_1} [H(\theta_k - \theta_i) - H(\theta_k)] + \sum_{l=n_1+1}^n [H(\theta_l - \theta_i) - H(\theta_l)] \quad (4-16)$$

and for $j = n_1 + 1, n_1 + 2, \dots, n$, the obtained equation is

$$n\kappa^{-1}d\theta_j/dt = H(-\theta_j) - H(\theta_j) + \sum_{k=2}^{n_1} [H(\theta_k - \theta_j) + H(\theta_k)] - \sum_{\substack{l=n_1+1 \\ l \neq j}}^n [H(\theta_l - \theta_j) + H(\theta_l)] \quad (4-17)$$

Linearization of (4-16,17) around the steady state, $\theta_i = \bar{\theta}_i + \delta\theta_i$, where $\bar{\theta}_i = 0$ for $i = 2, \dots, n$ and $\bar{\theta}_j = \psi$ for $j = n_1 + 1, n_1 + 2, \dots, n$, yields the following two respective equations for the phase perturbations:

$$n\kappa^{-1}d\delta\theta_i/dt = a_1\delta\theta_i \quad (4-18)$$

$$n\kappa^{-1}d\delta\theta_j/dt = a_2\delta\theta_j + b \sum_{k=2}^{n_1} \delta\theta_k - c \sum_{l=n_1+1}^n \delta\theta_l \quad (4-19)$$

In (4-18,19), a_1, a_2, b, c are the numerical coefficients defined as

$$a_1 = n_1 H'(0) - n_2 H'(\psi) \quad (4-20)$$

$$a_2 = n_2 H'(0) - n_1 H'(1 - \psi) \quad (4-21)$$

$$b = H'(0) + H'(1 - \psi) \quad (4-22)$$

$$c = H'(0) + H'(\psi) \quad (4-23)$$

where the prime denotes the derivative of the connection function H with respect to phase. The synchronization state is stable if all the eigenvalues of the matrix \mathbf{M}

$$\mathbf{M} = \begin{bmatrix} \mathbf{A}_1 & \mathbf{0} \\ \mathbf{B} & \mathbf{A}_2 \end{bmatrix} \quad (4-24)$$

are negative. The matrix \mathbf{M} has a block structure, where \mathbf{A}_1 is a $(n_1 - 1) \times (n_1 - 1)$ diagonal matrix, $[\mathbf{A}_1]_{ij} = a_1 \delta_{ij}$, \mathbf{A}_2 is a $(n_2 \times n_2)$ matrix with the elements $[\mathbf{A}_2]_{ij} = a_2 \delta_{ij} - c$, \mathbf{B} is a $n_2 \times (n_1 - 1)$ matrix with all elements equal to b , $[\mathbf{B}]_{ij} = b$, and $\mathbf{0}$ is a $(n_1 - 1) \times n_2$ block filled with zeroes.

Due to the block structure of (4-24) the set of eigenvalues of the matrix \mathbf{M} consists of the eigenvalues of the matrices \mathbf{A}_1 and \mathbf{A}_2 . The matrix \mathbf{A}_1 is diagonal with all the elements equal to a_1 ; hence, all the eigenvalues of \mathbf{A}_1 are equal to a_1 . The matrix \mathbf{A}_2 is a circulant matrix.

The matrix \mathbf{M} has the three distinct eigenvalues $\{a_1, a_2, a_2 - n_2 c\}$, which depend on the connection function H , the number of oscillators in the system n , and on the set of force polarities n_1 and $n_2 = n - n_1$ (4-15~24). Numerical calculations show that all the eigenvalues are negative at $n = 60$ and $n_1 = 1, 2, \dots, 59$. Therefore, the synchronization mode used for the pattern recognition is stable.

4.5 MATERIALS AND FEASIBILITY

4.5.1 BZ Gel Parameters

The connection function $H(\theta)$ shown in Fig. 4.3 was numerically obtained in [51] for the set of materials and model parameters specified below. We assume that the BZ gel is formed from poly(N-isopropylacrylamide) (PNIPAAm) chains containing grafted ruthenium metal-ion catalysts [5]. The model parameters are the same as in [51]. The volume fraction of polymer and the crosslink density in the undeformed BZ gel are $\phi_0 = 0.16$ and $c_0 = 4 \times 10^{-4}$, respectively. The interaction parameter χ^* , which accounts for the hydrating effect of the oxidized catalyst, is $\chi^* = 0.105$. The undeformed gel size is $h_0 = 0.5 \text{ mm}$. The values of λ_{\perp} and of the offset λ^* are $\lambda_{\perp} = \lambda^* \approx 1.65$, which corresponds to the steady-state value for the isotropic (unrestricted) swelling of the BZ gel [51].

4.5.2 Piezoelectric Cantilever Parameters

The coefficients m_{11} , m_{12} , and m_{22} in (4-4,5) that describe the behavior of a bending piezoelectric bimorph plate are given by the following equations [56]:

$$m_{11} = \frac{(L_p / h_p)^3}{2w_p E} \quad (4-25)$$

$$m_{12} = \frac{3}{4} d_{31} (L_p / h_p)^2 \quad (4-26)$$

$$m_{22} = 2w_p \varepsilon_{33} (1 - k^2 / 4) (L_p / h_p) \quad (4-27)$$

Here, L_p , w_p , and h_p are the respective length, width, and layer thickness of the piezoelectric bimorph plate; E , d_{31} , and ε_{33} are the Young's modulus, piezoelectric constant, and dielectric constant of the piezoelectric material, respectively. Finally, $k = (d_{31}^2 E / \varepsilon_{33})^{1/2}$ is the electromechanical coupling factor characterizing the piezoelectric material.

The piezoelectric bimorph plate dimensions are taken to be $L_p = w_p = 1\text{ mm}$, and $h_p = 10\text{ }\mu\text{m}$. The plate is assumed to be fabricated from polarized Lead-Zirconate-Titanate (PZT) ceramics. A typical PZT ceramic has a Young's modulus of $E = 50\text{ GPa}$; typical values for the other parameters are $d_{31} = -1.5 \times 10^{-10}\text{ mV}^{-1}$ and $\varepsilon_{33} = 1.8 \times 10^3 \varepsilon_0$, where $\varepsilon_0 = 8.85\text{ pFm}^{-1}$ is the dielectric constant of the vacuum [57]. In our calculations, we use the latter values of E and ε_{33} , and a twofold greater value for the piezoelectric constant (setting $d_{31} = -3 \times 10^{-10}\text{ mV}^{-1}$), which can be achieved in PZT through sophisticated processing methods [58][59].

We assume that the piezoelectric cantilevers are fabricated using advanced processing methods [58][59], which yield a two-fold increase in the piezoelectric constant relative to a typical PZT. At the model parameter values used for the calculations, the strength of coupling is $\kappa \approx 0.206$. For the chosen model parameters, the period of oscillation of the un-coupled oscillators is $T_0 \sim 1 \text{ min}$ [51].

4.5.3 Feasibility of System Fabrication

Recent advances in the fabrication of hybrid gel-piezoelectric systems indicate the feasibility of creating the BZ-PZ oscillator networks described here. In particular, studies have demonstrated that the deformation of a humidity-responsive polymer network on a piezoelectric film could generate measurable voltages [60]. It has also been shown that arrays of millimeter-sized piezoelectric actuator-sensor systems, which are laminated on soft biological materials, could monitor the mechanical properties of the underlying material [61]. Hence, current state-of-art manufacturing techniques allow researchers to fabricate millimeter-sized gel-piezoelectric elements, which generate strong electric signals.

4.6 DISCUSSION

In summary, we designed a materials system that can sense, actuate, communicate and compute in a self-organized manner. This functionality is enabled by the unique properties of the BZ gels, which do not require external power sources to drive their oscillatory motion. Moreover, these BZ gels are responsive to mechanical input from the overlying piezoelectric materials. The

piezoelectrics also play a crucial and distinctive role through their inter-conversion of mechanical and electrical energy, with the deformation of the cantilevers providing the voltage that flows through the system. We then employed these hybrid gel-piezoelectric units to couple local chemo-mechanical oscillations over long distances through electrical connections. This coupling allowed the oscillations of BZ-PZ units to become synchronized; in a network where the units are connected in series, the units with the same force polarity are synchronized in-phase and the ones with opposite force polarities are synchronized out-of-phase. Taking advantage of the distinct synchronization behavior of these chemo-mechanical networks, we leveraged concepts from oscillator-based computing in order to utilize our coupled BZ-PZ oscillators in performing pattern recognition tasks. In particular, we imposed a collection of input patterns onto different BZ-PZ networks, where each network encompassed a distinct stored pattern. The network encompassing the stored pattern closest to the input pattern exhibited the fastest convergence time to the stable synchronization behavior and could be identified as the “winner”. In this way, the networks of coupled BZ-PZ oscillators achieved pattern recognition. We demonstrated that the convergence time to the stable synchronization provides a robust measure of the degree of match between the input and stored patterns. Through these studies, we laid out fundamental and experimentally realizable design rules for creating “materials that compute”.

5.0 MULTIPLE BZ-PZ NETWORKS IN PARALLEL

A single BZ-PZ network can only perform pattern matching on black and white images (binary patterns). This limitation arises from storing patterns by setting binary values of the force polarities, ± 1 , in the device. To store and process richer images, such as colored patterns, we employ several BZ-PZ networks simultaneously as depicted in Figure 5.1, so that one pattern is encoded by multiple binary vectors and processed using different “channels”.

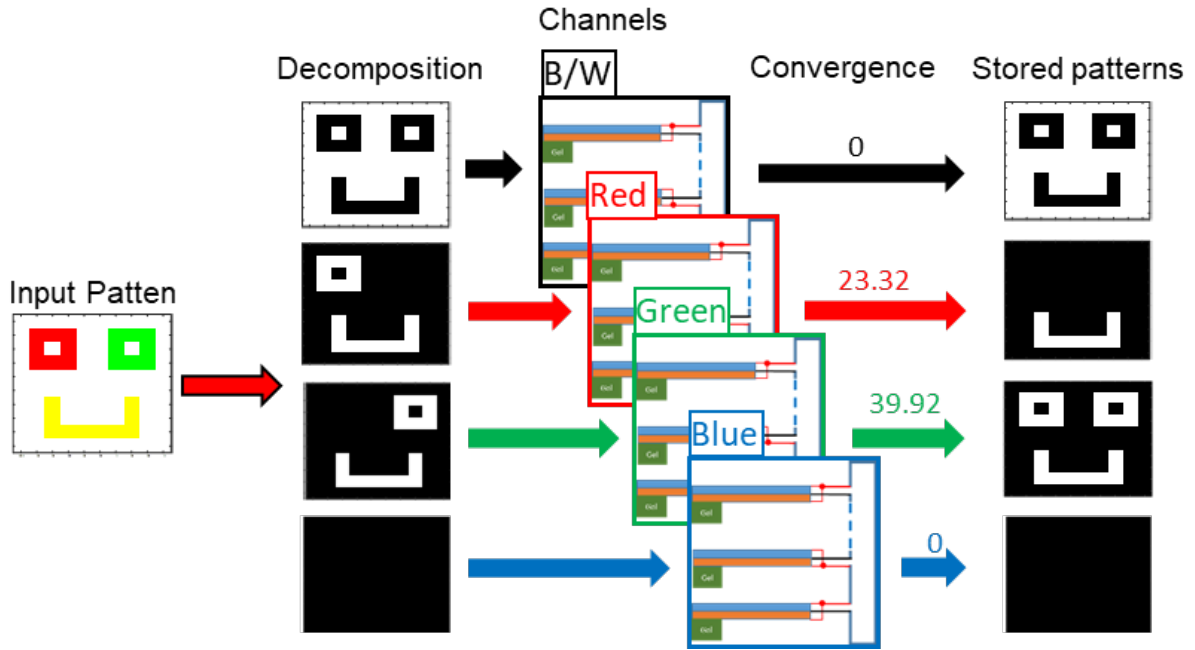
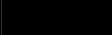









Figure 5.1 Schematics of the four BZ-PZ networks used for recognition of colored patterns. After decomposition of input image, the networks perform simultaneous matching operations in the corresponding information channels. The convergence time (given in number in cycles) is determined for each channel separately.

5.1 MULTI-CHANNEL BZ-PZ NETWORKS

The patterns that we consider here contain up to eight colors, which are represented in terms of the red-green-blue (RGB) color scheme [62]. As shown in Table 5.1, these eight colors are encoded into four binary value channels; the Red, Green, and Blue are the three fundamental color channels. The colors yellow, cyan and magenta are generated as combinations of the basic colors in RGB. Note that black and white could also be represented by RGB channels as (0,0,0) or (1,1,1) respectively. We, however, set these two colors as an independent channel to describe the shape of the pattern. In the original RGB model, any color can be obtained from the addition of different degrees of the RGB components. Because our color channel is binary and we assume that “0” and “1” represent the respective “none” and “full degree” of color, we are limited to eight colors in this case. Other colors can, however, be obtained with additional channels. For example, if the yellow, cyan, and magenta are defined as separate channels, more colors can be represented by through the combination of six, instead of three channels.

Table 5.1 Channel Representation of Color

Color	Name	Channels			
		Black/ White	Red	Green	Blue
	Black	0	0	0	0
	White	1	0	0	0
	Red	0	1	0	0
	Green	0	0	1	0
	Blue	0	0	0	1
	Yellow	0	1	1	0
	Cyan	0	0	1	1
	Magenta	0	1	0	1

To encode a specific color image (see Figure 5.1), we decompose the pattern into four binary vectors; each binary vector is stored in a single channel and there are four channels in total. In the black and white (B/W) channel, the pixel value is 1 only if the pixel is white. Namely, this channel marks the white background. For the remaining RGB channels, a value of ‘1’ indicates that the corresponding color component is present in the pixel. For example, yellow is the combination of red and green; hence, it is coded as (0,1,1,0).

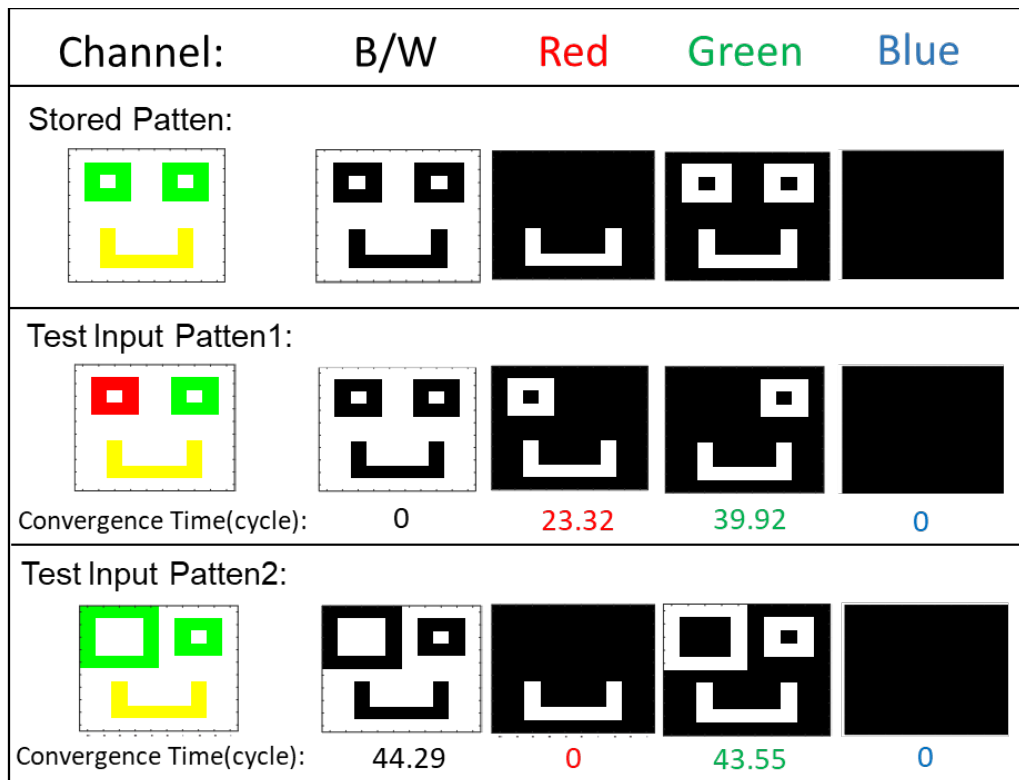


Figure 5.2 Pattern matching in color channels with multiple BZ-PZ networks. The first row shows the colored “smiley face” as the stored pattern, and its decomposed binary pattern images in the B/W, Red, Green and Blue channels, respectively. The second and third rows present the two test input patterns with different types of image variation, and their decomposed patterns in each channel. On the bottom of each row, the convergence time for each channel is shown.

Each of the four channels in Figure 5.1 is a network of serially coupled BZ-PZ oscillators. The first BZ-PZ network represents the B/W channel, and the second, third and

fourth networks represent the Red, Green, and Blue channels, respectively. Figure 5.1 illustrates the decomposition of a stored pattern into these four networks. In Figure 5.1, the stored pattern is a colored version of the “smiley face”, which now has two green “eyes” and a yellow “mouth”. The vector patterns in each of the different channels are displayed as binary, black and white images. Figure 5.2 shows the comparable decomposition of two sample input patterns (For convenience, we repeat the decomposition of the stored pattern as the first row of Figure 5.2).

These different channels capture different visual features of the original color pattern. For example, the network associated with the B/W channel discriminates the color pixels from the background. The pixels representing the green “eyes” are captured in the decomposed pattern in the Green channel, while the pixels representing the yellow “mouth” appear in both the Red and Green channels.

The two examples of test input patterns shown in the second and third rows of Figure 5.2 are deliberately designed to demonstrate two types of variations on the stored pattern. The first test pattern shows a variation in color; one of the green “eyes” in the stored pattern is switched to red. The location and total number of colored pixels remain unchanged, and thus, the shape of the “smiley face” is the same as the stored pattern. These features are effectively reflected in the decomposed patterns (Figure 5.2, second row). The decomposed pattern in the B/W channel still remains the same, but the “left eye” is moved from the Green channel to the Red channel, representing the color change. The second test pattern displays the same color scheme as the stored pattern, but the size of the left eye is enlarged. Namely, the shape of objects in the image is distorted. This change in image is captured in the decomposed patterns of both the B/W channel and the Green channel.

The pattern matching is performed simultaneously by the four BZ-PZ oscillator networks (i.e., the different channels). The networks contain the stored pattern according to the scheme in the top row of Figure 5.2. As in the previous example, the input patterns are used to initialize the phase of the oscillators in the network, following the scheme in row 2 or 3 of Figure 5.2. Once the BZ networks are initialized in this way, the decomposed binary images of the test pattern synchronize to the respective decomposed stored image.

As expected, the convergence time is sensitive to any defect or variation between the input and stored images in the corresponding channel. When the first input pattern is imposed on the network, the convergence time in the B/W and Blue channels are both 0 (see Figure 5.2). The fact that the convergence time is 0 in the B/W channel indicates that the geometric shape of the input and stored patterns are the same. The convergence time of the Green and the Red channels, however, are non-zero, thus indicating a variation in color between the input and stored patterns.

In the case involving the second test pattern, the non-zero convergence time in the B/W channel indicates that shape of the input and stored pattern are no longer identical. Of the color channels, it is only the Green one that exhibits a non-zero convergence time. Taken together, the information reveals that the variation in shape occurs in the green pixels. Hence, the measurements not only indicate a disparity in the shape of the test and stored patterns, but also pinpoint the region where the disparity is localized.

To gain further insight into the effect of defects on the convergence time in multiple channels, we perform another two tests on the same stored pattern, as illustrated in Figure 5.3. In these two tests, a series of input patterns are generated by replacing the green pixels of the “right eye” one by one with blue pixels (Figure 5.3(a)) or with white pixels (Figure 5.3(b)), until all the pixels of the right eye are turned into blue (in (a)) or made to disappear (in (b)). In the former

case, we illustrate the effect of modifying color, while in the latter case we illustrate the effect of modifying the shape of the image. In Figure 5.3(c)-(e), we plot the convergence times in networks corresponding to the respective Blue, Green, and B/W channels. Consider the situation for case (a) where the green pixels are turned to blue. Here, the number of blue pixels increases, while the number of green pixels decreases relative to the stored pattern. Notably, the convergence times increase in both the blue and green channels. This increase in convergence time is correlated to the increase in the number of “defective” pixels, which depends on the difference between the decomposed patterns of the input pattern and stored pattern. Namely, the Hamming distance between input and stored patterns increases as the number of green bits are flipped to another color and hence, the image becomes more “defective”. This result confirms our prior conclusion [15] that the convergence time of a BZ-PZ oscillator network can serve as distance metric between input and stored binary patterns.

The above conclusion also applies to case (b), where the convergence times in the Blue and the B/W channels are seen to increase. Again, the increase in convergence time is due to the accumulation of defects as the green pixels are replaced by white sites and the Hamming distance between the decomposed input and stored increases.

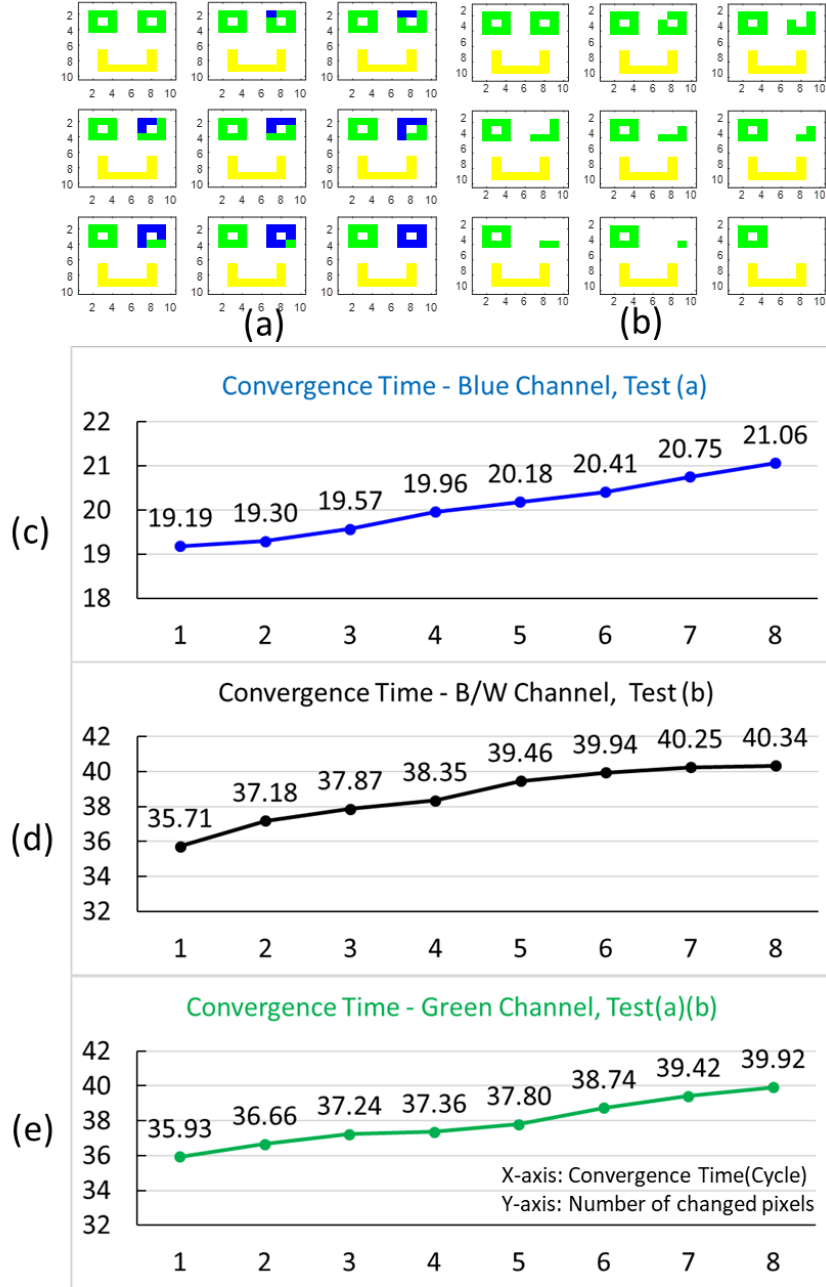


Figure 5.3 Pattern matching with varying input patterns. (a) Nine color image patterns show the process of turn green “left eye” into blue pixel by pixel. The first one is the stored pattern, and the rest eight patterns are the input patterns; (b) Similar test with the process that remove “left eye” object. We plot convergence time in each channel as a function of the number of changed pixels. (c) Convergence time in Blue channel in test (a). (d) Convergence time in B/W channel in test (b). (e) Convergence times in Green channel for both test (a) and (b). Note that the green channel responds in exactly the same manner to test (a) and (b), resulting in the same plot of the convergence time (e).

5.2 DETECTING DEFECTS IN QR CODE

We now apply our system to an important practical application: the pattern matching of a Quick Response (QR) code. QR codes are the two-dimensional barcodes used to label a tremendous range of consumer goods. Read by a barcode scanner or cell phone, the label allows merchandise to be readily identified, tracked and marketed [21]. QR codes are also used to store sensitive information such as bank account numbers or credit card information, and can be used to make automatic payments. Hence, being able to distinguish a legitimate QR code from a counterfeit image is of significant commercial importance.

A typical QR code pattern consists of a matrix of black and white pixels. Square patches, or “anchors”, fixed at three corners of the image are used to locate and center the position of the pattern. The pixels in the remainder of the image are arranged in a specific order to encode the desired information. We first generate a 21×21 sized QR pattern that encodes the text phrase “Hello World”. (The message is encoded with standard QR code algorithm.) We then convert this black and white image into a colored pattern by randomly converting all the black pixels into the colors in Table 2 to form a new pattern. Such a colored QR pattern can also be correctly decoded by a QR code scanner (if the grayscale threshold is set properly). Here, the encoded color pattern can be used to inscribe additional information [63]. Similar to the previous tests, we store the color QR pattern in four BZ-PZ oscillator networks, as illustrated in Figure 5.4. The network for each channel has the same number of BZ-PZ units as the number of pixels ($21 \times 21 = 441$).

In the next step, we introduce defect pixels in the input patterns by randomly altering the colors in a number of pixels in the stored pattern. In this test, we add 1, 10, 20, 30, 40, 50 defect pixels in sequence and for each case, we repeat the simulation of pattern matching 100 times,

with different randomized defects in the input patterns. Figure 5.4 shows the stored QR pattern and an example of an input pattern with 10 defect pixels. The results from the simulations are plotted as bar graphs that contain averaged, minimum and maximum convergence times. The error bars for the minimum and maximum convergence times display a relatively broad range for the cases with one “defective” pixel; this is due to the large variations associated with the random selection and color change of just one pixel. Changing the colors of pixels into yellow, cyan, or magenta involves two channels and thus brings larger variations in the convergence time in cases that involve just a few defect pixels. These variations in convergence time are reduced as the number of defect pixels is increased.

Importantly, the simulation results shown in Figure 5.4 indicate that the matching operation is very sensitive to the presence of defects, with even one defect producing an obvious delay in synchronization (above 30 oscillation cycles) as compared to perfect matching between the input and stored patterns. With respect to using the device for encryption or devising a security system, the test QR code information “Hello World” can be viewed as the “plain code”, while the codes in the RGB channels serve as a “password” (or a “watermark”) in the different “layers”. In other words, the password is encrypted in multiple channels. In this case, any test pattern where a colored pixel has been flipped from the original colorized pattern (on the left in Figure 5.4) would fail the verification test, even though the test image carries the correct plain code for a QR scanner. Hence, this QR code test exhibits the potential of our system to be applied in cryptography or steganography. In the latter case, our system can hide an encrypted message, where even if the encrypted message is deciphered (in this case the black and white QR code), the hidden message (encoded in the colored pattern) is not seen.

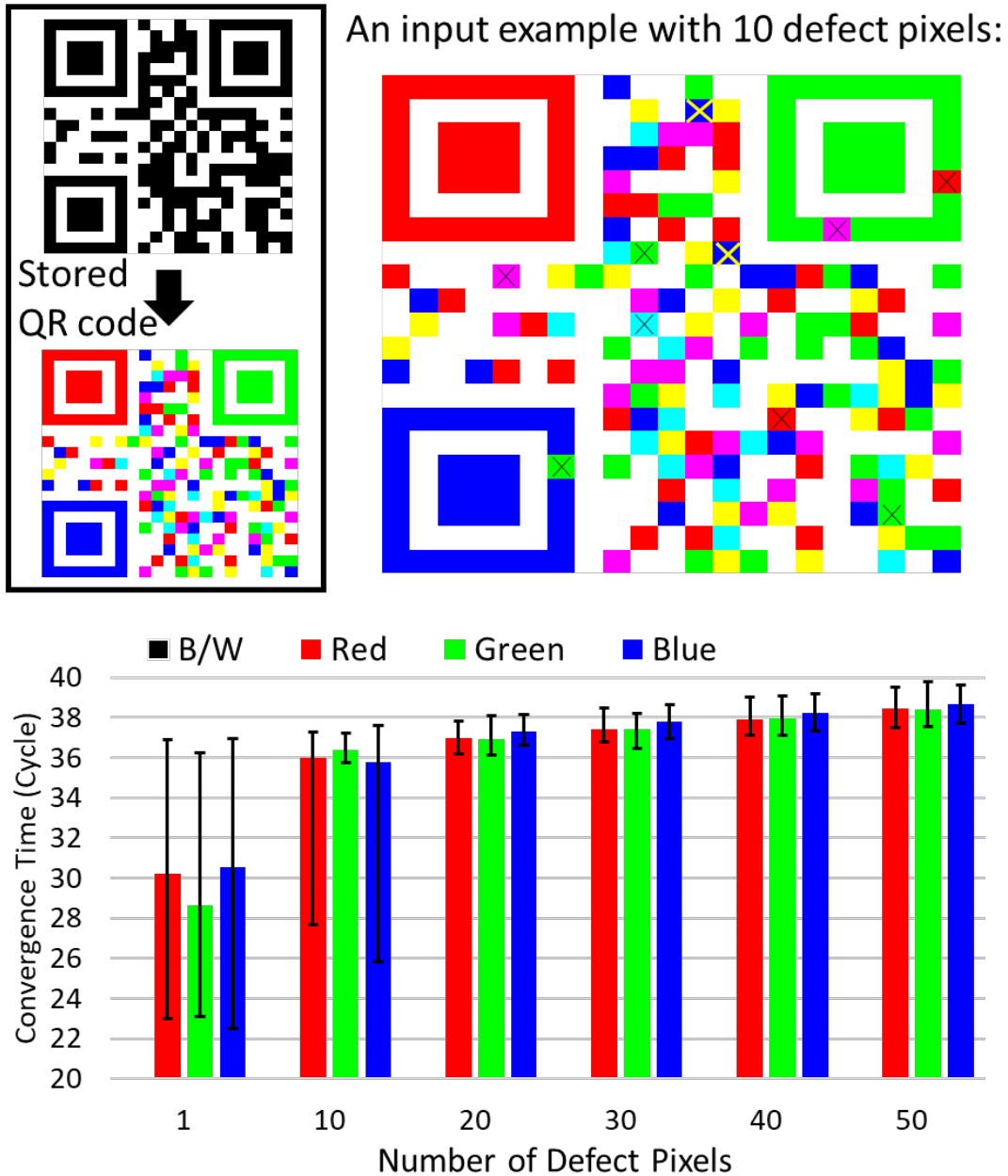


Figure 5.4 Pattern matching of QR code in multiple color channel. The black/white binary QR code pattern of “Hello World” and randomly colored version as stored pattern are shown in black frame. An example of test input patterns with 10 defect pixels (marked with “x”) are placed on the top right. The bar graph on the bottom gives the averaged convergence time of the repeated simulation of matching operations. The error bars give the maximum and minimum. Each input pattern is labeled at x-axis according to its number of defect pixels, with the three color bars corresponding to convergence time in RGB channels. Note that B/W channel detects no channel in this test and its convergence time is 0, which is not shown.

5.3 DISCUSSION

Our overarching goal is to design a materials system where the inherent properties of the different components enable the system to perform a computational task: pattern recognition. This task is enabled by combining the unique behavior of self-oscillating BZ gels and piezoelectric (PZ) films in a system that undergoes continuous oscillations without external electrical input. We also built on advances in computer science to utilize the synchronization of oscillators to perform computation. In essence, the properties of the material and the computing paradigm are ideally matched.

A particularly challenging task for these “materials that compute” is to detect defects in an input pattern relative to a stored image that encompasses information in both the shape and the color of the pattern. In effect, the device must encode and recognize a significant amount of specific structural detail. Here, we addressed this problem by employing a single BZ-PZ network as a distinct “channel” and utilizing multiple channels at once. By decomposing a colored image into sets of binary vectors, we used each channel to store distinct information about the color of the pattern and the shape of the image. By using multiple networks, we captured the spatial features of the entire image in this multi-channel system.

Our simulations reveal that the proposed multi-channel BZ-PZ device can detect remarkably subtle differences in spatial features between the input and stored patterns. In particular, the device can detect a change in the color of just one pixel or a small change in the shape of an object in the image. We also applied our system to the task of recognizing a colored QR code and thereby showed its potential in cryptography or steganography.

The multiple BZ-PZ oscillator networks recognize patterns by detecting the shortest convergence time among the networks [13]. The convergence time is a measure of how long it

takes for a set of oscillators to become phase-locked (i.e., synchronized to the final stable states). In the simulations, the latter condition is met if the phase differences among the units lie below a specified threshold value. In a physical realization of this system, peripheral circuitry would be necessary to detect the state of synchronization and measure the convergence time. Such synchronization detection circuits have been designed and implemented in prior studies of neuromorphic and oscillator-based computing [26][64][65].

It is worth emphasizing that the BZ gels are sensitive to light, pressure and chemical stimuli, and hence, the input pattern can be imposed onto the network through a number of physical or sensory means. In other words, the devices are responsive to external cues and thus, can be used to detect environmental changes. By using multi-channel BZ-PZ devices, we can significantly expand the functionality of these “materials that compute” since we can encode and recognize patterns with richer information content. Hence, the devices are practically suitable for pattern matching or recognition of images that encrypt information at different “layers” or spatial levels. Thus, the device can prove to be particularly valuable for security applications that require detection of counterfeit information, encoding of hidden information, and verification of multi-attribute passwords.

In this section, we extend the information representation in our system by organizing multiple BZ-PZ network and encode complex patterns with basic binary patterns that can be processed in single BZ-PZ network. Despite the advantages we exploit in such a multi-network design, the limit of information capacity in a single network is not improved yet in this case. In the next chapter, we demonstrate a new method to enrich the information representation in a single BZ-PZ network.

6.0 BZ-PZ OSCILLATOR NETWORK WITH CAPACITORS

One limitation of the previously proposed BZ-PZ oscillator network is that it can either only process patterns composed of binary values or need multiple networks for information representation. This restriction is due to the limited number of phase differences between groups of oscillators attained at steady state. The phase difference between oscillators in a given synchronization mode is determined by the direction of the polarization of the PZ cantilevers in the network. These polarities can only have one of two directions (labeled +1 or -1) and result in either in-phase or anti-phase synchronization between oscillators.

In this chapter, we present a method for increasing the amount of information that can be represented by a given BZ-PZ network. We accomplish this task by introducing capacitors into the system (Figure 6.1) and using the capacitors to modify the interactions between the BZ-PZ units. We demonstrate that the introduction of capacitors alters the system dynamics and creates additional, stable synchronization modes. The availability of these new modes allows the BZ-PZ system to store additional information and thus, expands the utility of the device.

Our inspiration for adding capacitors to the BZ network comes from the behavior of biological neural systems, where synapses, or neuronal junctions, play a vital role in the formation of memory. The strength of a synapse is determined by the strength of the coupling between neurons and facilitates the storage of information [66]. For decades, computer scientists model neural systems with artificial neural networks, where the synaptic strength between nodes

is represented by weight parameters [67]. By adjusting the weights with various learning algorithms [68], these artificial neural networks can be made to store information. In recent research on neuromorphic computing, which mimics neuro-biological architectures in a computing hardware platform, the function of synapses can be implemented by introducing devices that display variable states, such as variable capacitance and resistance [69][70][71].

In the BZ-PZ oscillator network, information about a particular pattern is stored by programming the coupling strength between BZ-PZ units (i.e., the binary values of the force polarities). We now show how this dynamical behavior can be controlled and augmented by the introduction of the appropriate passive components, i.e., the capacitors. As detailed herein, the capacitors effectively redistribute the charge and force within the system and thereby modify the strength of the interactions among the units. This modification in turn alters the system dynamics. Hence, these findings give fundamental insight into how certain physical factors affect the behavior of dynamical systems and how these factors can be used to tailor the functionality of the system.

I. BZ-PZ Oscillator Network with Capacitors

Figure 6.1 shows that the capacitors are connected in parallel to the BZ-PZ units. Without the capacitors, the network is capable of storing binary patterns because the two different force polarities within the system give rise to in-phase and anti-phase oscillation upon synchronization. To augment the information storage capabilities of the BZ-PZ oscillator network, we must modify the system so that it can access a greater number of stable synchronization modes. As discussed below, the addition of capacitors to the network provides an expedient means of achieving the latter goal.

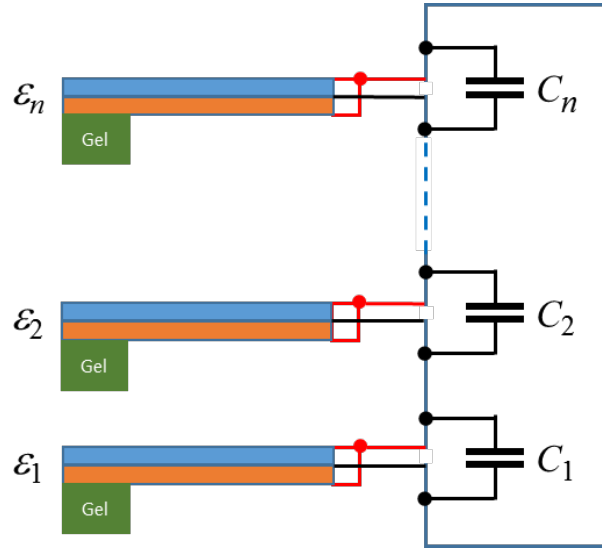


Figure 6.1 Schematics of the BZ-PZ oscillator network with capacitors connected to each unit.

There are a few other reasons of choosing capacitors as the additional component in the network. First, the entire BZ-PZ system is self-powered; the chemical energy from the reaction fuels the pulsations of the gel and the PZ provides a means of transducing energy from the chemo-mechanical domain into the electrical domain. The ability to operate in a self-sustained manner is a distinctive feature of the system that can play a vital role in designing robotic systems performing in a relatively autonomous manner. To maintain this advantageous feature, we focused on the components that operate with the need of an external power supply; this constraint ruled out utilizing active devices like transistors. Second, resistors dissipate heat and thus, would decrease the energy efficiency of the device. Third, other passive device such as inductors might not provide the desired modifications to the system dynamics due to the large impedance of low frequency signals. Given Eq. (6-1), which describes the relationship between charge and voltage, we hypothesized that capacitors could serve as useful components, especially because they are passive devices that can be used to store and redistribute charge. In this section,

we derive the dynamical behavior and a phase model of BZ-PZ oscillator networks that contain capacitors. Using an analytical approach, we then determine the stability of the system.

6.1 MODIFIED PHASE MODEL

The effect of introducing capacitors on the interactions between the BZ-PZ units can be determined by following similar steps as discussed in previous section, using the same notation. The frequency of the gel's chemo-mechanical oscillations is on the order of 0.01 Hz, which is much lower than the eigenfrequency of a PZ cantilever (~ 10 kHz). Hence, the behavior of PZ cantilevers that are modified with capacitors connected in parallel (as shown in Figure 6.1) can be described by the quasi-static equations. The deflection of the PZ plate in unit i , ξ_i , the electric charge on this plate, $Q_i^{(1)}$, and the electric charge of the capacitor, $Q_i^{(2)}$, are related to the force, F_i , applied to the cantilever and the electric potential difference (voltage), U_i , between the electrodes through the following equations:

$$\xi_i = m_{11} F_i + \varepsilon_i m_{12} U_i$$

$$Q_i^{(1)} = \varepsilon_i m_{12} F_i + m_{22} U_i \tag{6-1}$$

$$Q_i^{(2)} = C_i U_i$$

Here, m_{11} , m_{12} , and m_{22} are the coefficients determined by the properties of the piezoelectric material and the cantilever dimensions [51]. The parameter ε_i is the force polarity. It specifies the polarity of the generated voltage, U_i , and depends on the relative direction between the polarization of the PZ materials and the bending force applied on the tip of

cantilever. If the polarization and force lie in the same direction, $\varepsilon_i = +1$; otherwise, $\varepsilon_i = -1$.

Finally, C_i is the capacitance of the capacitor connected in parallel to the PZ plate (Figure 6.1).

In order to derive the equations governing the behavior of the BZ-PZ network with capacitors, we re-write Eqs. (6-1) in the following form:

$$F_i = F_i^{(0)} - m_{11}^{-1} m_{12} \varepsilon_i U_i \quad (6-2)$$

$$Q_i = m_{12} \varepsilon_i F_i^{(0)} + (C_0 + C_i) U_i \quad (6-3)$$

Here, $F_i^{(0)} = m_{11}^{-1} \xi_i$ is Hooke's law for the cantilever without accounting for the effect of piezoelectricity, $Q_i = Q_i^{(1)} + Q_i^{(2)}$ is the total electric charge on the PZ plate and capacitor connected in parallel, and $C_0 = m_{22}(1 - \zeta^2)$ is the capacitance of the PZ plate. In the latter equation, $\zeta^2 = m_{12}^2 (m_{11} m_{22})^{-1}$ is a dimensionless parameter that depends on the electromechanical coupling of the PZ material and does not depend on the PZ plate dimensions [51]. For the model parameters used in our previous calculations [51], $\zeta \approx 0.413$ and the capacitance of the PZ plate is $C_0 \approx 2.96 \text{ nF}$. As all the BZ-PZ units modified with the capacitors are connected in series, $Q_i = Q$ and $\sum_{i=1}^n U_i = 0$. From Eq. (6-3), we determine the electric charge Q

$$Q = m_{12} N^{-1} \sum_{j=1}^n \varepsilon_j z_j F_j^{(0)} \quad (6-4)$$

where

$$z_i = (1 + C_i / C_0)^{-1} \quad , \quad N = \sum_{l=1}^n z_l \quad . \quad (6-5)$$

It is convenient to measure capacitance in units of C_0 , so $C_i / C_0 \rightarrow C_i$ in what follows below. Finally, using Eq. (6-3) and (6-4), we find the voltage U_i and then substitute this expression into Eq. (6-2) to obtain

$$F_i = F_i^{(0)} + \kappa \left(z_i F_i^{(0)} - N^{-1} \varepsilon_i z_i \sum_{j=1}^n \varepsilon_j z_j F_j^{(0)} \right) \quad (6-6)$$

where $\kappa = \zeta^2(1 - \zeta^2)^{-1}$.

Eq. (6-6) is a generalization of Eq. (4-6) in Section II. Note that the effect of capacitor is eliminated (i.e., the capacitor is removed) if $C_i = 0$ in Eq. (6-10). If $C_i = 0$ for all $i = 1, 2, \dots, n$, then Eq. (6-6) is identical to Eq. (4-6).

Because the coupling between the oscillating BZ-PZ units is weak, we can use the phase dynamics approach to describe the interactions between these oscillators in terms of the time-dependent deviation of the phase of each oscillator, $\varphi_i(t)$. This description of the system dynamics reduces the complexity of the problem and provides a tractable means of determining the time-dependent behavior of the weakly coupled oscillators [46]. In Section 4.1.3, we formulated the phase description for the BZ-PZ networks with no capacitors. We note that Eq. (4-6) is a generalization of the respective equation for the network at $C_i = 0$ (no capacitors) to the network at $C_i \geq 0$ (with or without capacitors), and the only difference between the two equations is in the numerical prefactors in front of the forces $F_j^{(0)}$. Therefore, the phase dynamics equation derived in Section 4.1.3 can be immediately generalized to the case of $C_i \geq 0$ simply by changing the corresponding numerical coefficients and hence, we obtain

$$\kappa^{-1} d\varphi_i / dt = z_i H(0) - N^{-1} \varepsilon_i z_i \sum_{j=1}^n \varepsilon_j z_j H(\varphi_j - \varphi_i) \quad (6-7)$$

Here, the function $H(\varphi_j - \varphi_i)$ is referred to as the “connection function”, and characterizes the rate of the phase shift of oscillator i due to its interaction with the oscillator j at a phase difference $\varphi_j - \varphi_i$. The phases of oscillation in Eq. (6-7) are normalized such that $0 \leq \varphi_i \leq 1$, $1 \leq i \leq n$. The connection function $H(\theta)$ is periodic at $\theta \in [0,1]$. Figure 6.2(a) shows the connection function $H(\theta)$ determined numerically in [51]. The plot demonstrates that the phase response of a BZ-PZ oscillator to an external action is quite complex. The interaction between a pair of oscillators can cause both positive and negative phase shifts depending on the phase difference (because $H(\varphi_j - \varphi_i)$ can be positive or negative depending on the phase difference $\varphi_j - \varphi_i$), and on the force polarities of the two oscillators, i.e., on the sign of $\varepsilon_i \varepsilon_j$.

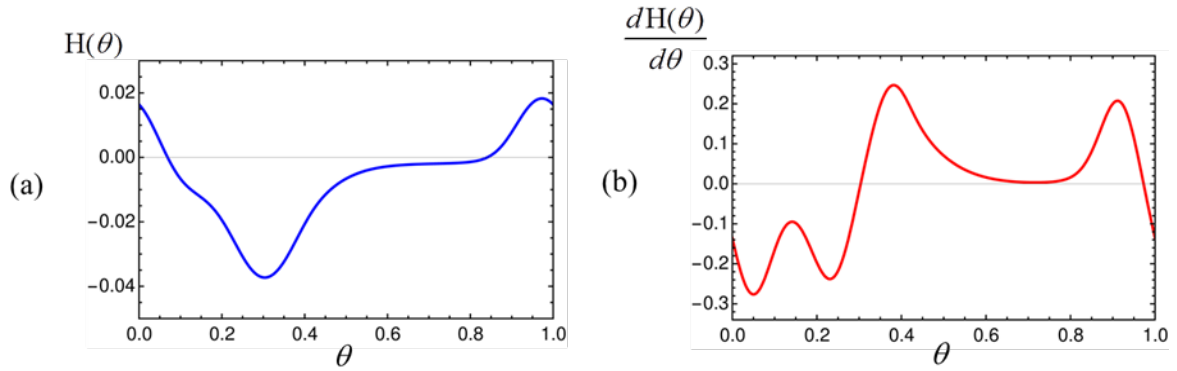


Figure 6.2 Connect Function and its derivative; (a) The connection function $H(\theta)$ in phase model of BZ-PZ oscillator networks, Eq. (6-7). The function is periodic at $\theta \in [0,1]$. (b) The plot of the derivative of $H(\theta)$ in one period.

The functional form of Eq. (6-7) indicates that the capacitors modify the coupling strength between the BZ-PZ units i and j because the prefactor $z_i z_j$ depends on the

capacitances C_i and C_j according to Eq. (8). Therefore, introduction of the capacitors into the BZ-PZ network could be used to create a controllable hierarchy of interactions within the network. Note also that $z_i \leq 1$ and decreases with an increase in C_i , i.e., the capacitors weaken the interaction between the BZ-PZ units. The latter behavior is not surprising because some part of the electrostatic energy generated by the PZ cantilevers is now spent on charging the capacitors. The limit $C_i \rightarrow \infty$ ($z_i \rightarrow 0$ in this case) corresponds to shorting unit i , so it does not interact with other BZ-PZ units. Below, we discuss how the introduction of the capacitors affects the synchronization behavior of the BZ-PZ networks [13].

6.2 THEORETICAL ANALYSIS

Numerical solution of Eq. (6-7) reveals that the capacitors can induce qualitative changes in the synchronization behavior of the BZ-PZ networks. To demonstrate this point, we consider a system that consists of 100 serially connected BZ-PZ units, where 50 units have the force polarity +1 and another 50 units have the force polarity -1. For convenience, we label the oscillators in the first group with $1 \leq i \leq 50$, and the second group is labeled with $51 \leq i \leq 100$. We solve Eq. (6-7) at random initial phases, and plot the values $\varphi_i - \varphi_1$, $2 \leq i \leq 100$, as functions of time t measured in the number of cycles (Figure 6.3).

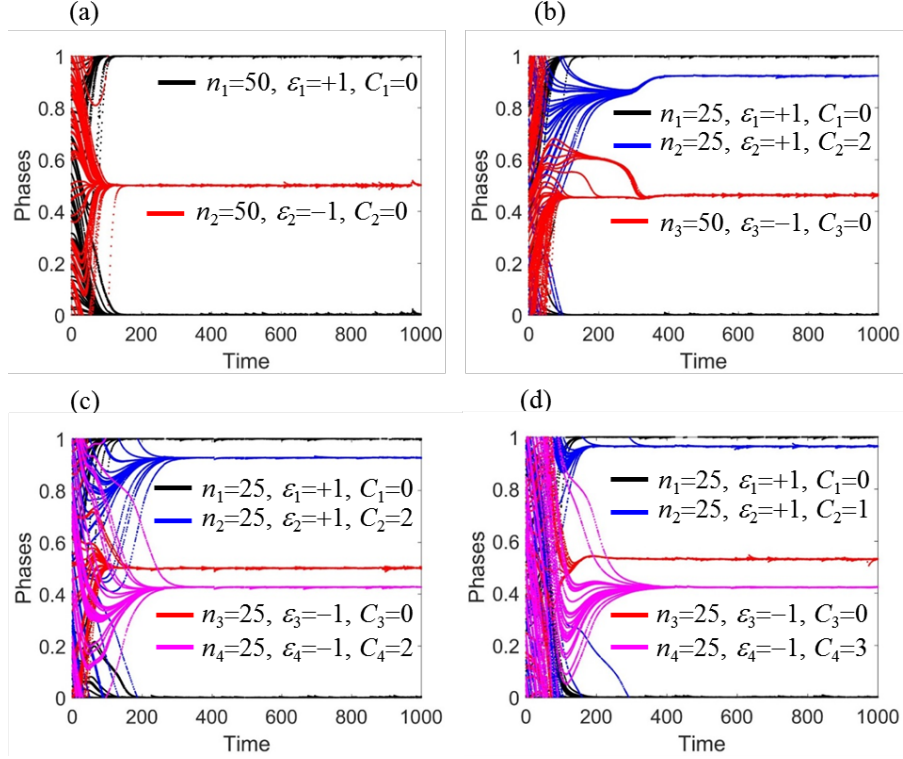


Figure 6.3 The evolution of phase differences between all the BZ-PZ units and the first reference unit, initialized with random phases. The legends of plot show the colors that represent different group of units with corresponding parameters (a) original BZ-PZ network with no capacitors; (b)-(d) BZ-PZ networks consist of multiple groups of units with different capacitance.

Without capacitors, the two groups of oscillators become synchronized anti-phase (Figure 6.3a) as reported previously (Section 4.2). As seen in Figure 6.3a, the BZ-PZ units with the same force polarity exhibit the in-phase synchronization, whereas the units with opposite polarities are synchronization with the phase difference 0.5.

We then consider a network in which 25 units with $\varepsilon_i = +1$ ($26 \leq i \leq 50$) are modified with capacitors having a capacitance of $C_i = 2$. Hence, the network now consists of three distinct groups of BZ-PZ oscillators. We denote the network configuration as $\{n_\alpha\} = \{25, 25, 50\}$, $\{\varepsilon_\alpha\} = \{+1, +1, -1\}$, and $\{C_\alpha\} = \{0, 2, 0\}$, where n_α , ε_α , and C_α are the respective number of units, force polarity and capacitance for group α ; here, $\alpha = 1, 2, 3$. Figure 6.3b shows that after

initialization with random phases, the network achieves the state of synchronization that is different from the one in Figure 6.3a. The addition of the capacitors results in splitting the units having the polarity +1 into two groups, which are synchronized with a phase difference. Specifically, groups 1 and 2 (polarity +1, without and with capacitors) are synchronized with a phase difference of about 0.1 (see the black- and blue-colored curves in Figure 6.3b). The groups 1 and 3 (polarities +1 and -1, no capacitors) are synchronized with the phase difference of about 0.5, i.e., exhibit the synchronization behavior similar to that in Figure 6.3a (compare the black- and red-colored curves in Figure 6.3ab).

Further modification of the network by adding the capacitors to some units with the polarity -1 leads to splitting the latter oscillators into two groups, which are synchronized with a phase difference. Figure 6.3c shows the phase dynamics of the network with configuration $\{n_\alpha\} = \{25, 25, 25, 25\}$, $\{\varepsilon_\alpha\} = \{+1, +1, -1, -1\}$, and $\{C_\alpha\} = \{0, 2, 0, 2\}$. The units in groups 3 and 4, which have the force polarity -1, are now synchronized with the phase difference about 0.1 (the red- and magenta-colored lines in Figure 6.3c), i.e., their synchronization behavior is similar to that of the groups 1 and 2 (the black- and magenta-colored lines in Figure 6.3c).

The value of the phase difference between the oscillation of units that have the same force polarity and differ due to the presence of capacitors depends on the capacitance. Figure 6.3d shows the synchronization behavior of the BZ-PZ network that has the same $\{n_\alpha\}$ and $\{\varepsilon_\alpha\}$ as those in Figure 6.3c but with different $\{C_\alpha\}$, namely $\{C_\alpha\} = \{0, 1, 0, 3\}$. Upon synchronization, the phase difference between groups 1 and 2 is smaller than that between groups 3 and 4, i.e., the phase difference increases with an increase in capacitance.

Thus, the results of the calculations presented in Figure 6.3 clearly demonstrate that the introduction of capacitors, and the subsequent changes to the strength of interaction between the

individual units, leads an enrichment of the phase synchronization behavior of the system. Below, we analyze stability of the synchronization modes induced by the capacitors.

6.2.1 Stability Analysis

To validate the stability of the synchronization modes that encompass multiple phase differences, we apply the linear stability analysis to the system of equations, Eq. (6-7). Specifically, we analyze the BZ-PZ networks that contain three groups of units as in Figure 6.3b.

We consider a system of n connected BZ-PZ oscillator units that are separated into three groups, so the network configuration is $\{n_\alpha\} = \{n_1, n_2, n_3\}$, where $n_1 + n_2 + n_3 = n$, $\{\varepsilon_\alpha\} = \{\varepsilon_1, \varepsilon_2, \varepsilon_3\}$, and $\{C_\alpha\} = \{C_1, C_2, C_3\}$. The units are labeled with the index i such that $1 \leq i \leq n_1$, $n_1 + 1 \leq i \leq n_1 + n_2$, and $n_1 + n_2 + 1 \leq i \leq n$ correspond to the respective groups 1, 2 and 3. The application of Eq. (6-7) to the three groups of units gives the following equation for the phase dynamics group α , where $\alpha = 1, 2, 3$:

$$N\kappa^{-1}d\varphi_i/dt = N z_\alpha H(0) - z_\alpha \varepsilon_\alpha \left[z_1 \varepsilon_1 \sum_{p=1}^{n_1} H(\varphi_p - \varphi_i) + z_2 \varepsilon_2 \sum_{q=n_1+1}^{n_1+n_2} H(\varphi_q - \varphi_i) + z_3 \varepsilon_3 \sum_{r=n_1+n_2+1}^n H(\varphi_r - \varphi_i) \right] \quad (6-8)$$

Here, $z_\alpha = (1 + C_\alpha)^{-1}$ and N are defined according to Eq. (8).

We assume that the trajectories of the equations approach a steady state where each group has a fixed phase, as we observed in numerical simulations. We set the phase of the first group as the reference 0, so the equilibrium point in terms of the phase differences is $\{0, \psi_1, \psi_2\}$. The parameters ψ_1 and ψ_2 give the differences in the phase of oscillation between the first group and

the other two groups. The following nonlinear equations for ψ_1 and ψ_2 are obtained from Eq. (6-8) and can be solved numerically:

$$\begin{aligned} & [z_1 z_2 (n_1 - n_2) + z_3 n_3 (z_2 - z_1)] H(0) - z_1 z_2 \varepsilon_1 \varepsilon_2 [n_1 H(-\psi_1) - n_2 H(\psi_1)] \\ & - n_3 z_3 \varepsilon_3 [z_2 \varepsilon_2 H(\psi_2 - \psi_1) - z_1 \varepsilon_1 H(\psi_2)] = 0 \end{aligned} \quad (6-9)$$

$$\begin{aligned} & [z_1 z_3 (n_1 - n_3) + z_2 n_2 (z_3 - z_1)] H(0) - z_1 z_3 \varepsilon_1 \varepsilon_3 [n_1 H(-\psi_2) - n_3 H(\psi_2)] \\ & - n_2 z_2 \varepsilon_2 [z_3 \varepsilon_3 H(\psi_1 - \psi_2) - z_1 \varepsilon_1 H(\psi_1)] = 0 \end{aligned} \quad (6-10)$$

Assuming that ψ_1 and ψ_2 are known, we carry out a linearization of Eq. (6-8) around the equilibrium point for the phase differences $\theta_i \equiv \varphi_i - \varphi_1$, $2 \leq i \leq n$. Namely, we take $\theta_i(t) = \bar{\theta}_i + \delta\theta_i(t)$, where $\bar{\theta}_i = 0$ for group 1, $\bar{\theta}_i = \psi_1$ for group 2, and $\bar{\theta}_i = \psi_2$ for group 3, and $\delta\theta_i(t)$ is a small perturbation. This operation yields the following respective equation for the phase perturbations of oscillators in group α , where $\alpha = 1, 2, 3$:

$$N\kappa^{-1} d\delta\theta_i/dt = a_\alpha \delta\theta_i + b_\alpha \sum_{p=2}^{n_1} \delta\theta_p + c_\alpha \sum_{q=n_1+1}^{n_1+n_2} \delta\theta_q + d_\alpha \sum_{r=n_1+n_2+1}^n \delta\theta_r \quad (6-11)$$

In the above equation, the numerical coefficients are $a_\alpha = \sum_{\beta=1}^3 h_{\alpha\beta} n_\beta$ for $\alpha = 1, 2, 3$, $b_1 = c_1 = d_1 = 0$, and $b_\alpha = h_{11} - h_{\alpha 1}$, $c_\alpha = h_{12} - h_{\alpha 2}$, $d_\alpha = h_{13} - h_{\alpha 3}$ for $\alpha = 2, 3$; the values $h_{\alpha\beta}$ are the elements of the following matrix:

$$\|h_{\alpha\beta}\| = \begin{bmatrix} z_1^2 H'(0) & z_1 z_2 \varepsilon_1 \varepsilon_2 H'(\psi_1) & z_1 z_3 \varepsilon_1 \varepsilon_3 H'(\psi_2) \\ z_1 z_2 \varepsilon_1 \varepsilon_2 H'(-\psi_1) & z_2^2 H'(0) & z_2 z_3 \varepsilon_2 \varepsilon_3 H'(\psi_2 - \psi_1) \\ z_1 z_3 \varepsilon_1 \varepsilon_3 H'(-\psi_2) & z_2 z_3 \varepsilon_2 \varepsilon_3 H'(\psi_1 - \psi_2) & z_3^2 H'(0) \end{bmatrix},$$

where $H'(\theta)$ is the first derivative of the connection function shown in Figure 6.3b.

The synchronization state is stable with respect to small perturbations if all $\delta\theta_i$ decay, which occurs when all eigenvalues of the coefficient matrix \mathbf{M} on the right-hand side of Eq. (6-11) have negative real parts. The coefficient matrix has the following block structure:

$$\mathbf{M} = \begin{bmatrix} \mathbf{A}_1 & \mathbf{0} & \mathbf{0} \\ \mathbf{B}_2 & \mathbf{A}_2 & \mathbf{D}_2 \\ \mathbf{B}_3 & \mathbf{C}_3 & \mathbf{A}_3 \end{bmatrix} \quad (6-12)$$

Here, \mathbf{A}_1 is a $(n_1 - 1) \times (n_1 - 1)$ diagonal matrix, $[\mathbf{A}_1]_{ij} = a_1 \delta_{ij}$, \mathbf{A}_2 is a $n_2 \times n_2$ matrix with the elements $[\mathbf{A}_2]_{ij} = a_2 \delta_{ij} + c_2$, and \mathbf{A}_3 is a $n_3 \times n_3$ matrix with the elements $[\mathbf{A}_3]_{ij} = a_3 \delta_{ij} + d_3$. Further, \mathbf{B}_2 and \mathbf{D}_2 are the respective $n_2 \times (n_1 - 1)$ and $n_2 \times n_3$ blocks filled with b_2 and d_2 , \mathbf{B}_3 and \mathbf{C}_3 are $n_3 \times (n_1 - 1)$ and $n_3 \times n_2$ blocks filled with b_3 and c_3 , respectively. Finally, $\mathbf{0}$ denotes the blocks filled with zeros.

The eigenvalues of the block matrix \mathbf{M} can be determined analytically. This matrix has five distinct eigenvalues, namely,

$$\lambda_k = a_k, \quad k = 1, 2, 3; \quad \lambda_{4,5} = (B \pm \sqrt{D}) / 2, \quad (6-13)$$

where

$$B = a_2 + n_2 c_2 + a_3 + n_3 d_3,$$

$$D = (a_2 + n_2 c_2 - a_3 - n_3 d_3)^2 + 4n_2 n_3 c_3 d_2.$$

The eigenvalues λ_k with $k = 1, 2, 3$ have a respective multiplicity of $(n_k - 1)$. All eigenvalues depend on the number of units, force polarity, capacitance, the derivative of the connection function for the given phase differences. Note that the eigenvalues with $k = 1, 2, 3$ could be associated with the respective groups of units since $\lambda_k = a_k$. The eigenvalues with

$k = 4, 5$ could be associated with the interaction between the second and third groups of oscillators because only numerical coefficients with the indices $\alpha = 2, 3$ contribute to $\lambda_{4,5}$.

In the next section, we numerically solve Eqs. (6-9) and (6-10) to determine the phase differences in the state of synchronization at various model parameters, and numerically evaluate the eigenvalues to characterize the stability.

6.2.2 Synchronization in the Three-group Networks

To analyze further how the number of units in the groups, the force polarity, and the value of capacitance affect the synchronization mode in the BZ-PZ networks, we apply the stability analysis of the three-group case described in the previous section. Specifically, we consider the network having the configuration $\{n_i\} = \{n_1, n_2, 50\}$ with variable n_1 and n_2 , $\{\varepsilon_i\} = \{+1, +1, -1\}$, and $\{C_i\} = \{0, C_2, 0\}$ with variable C_2 .

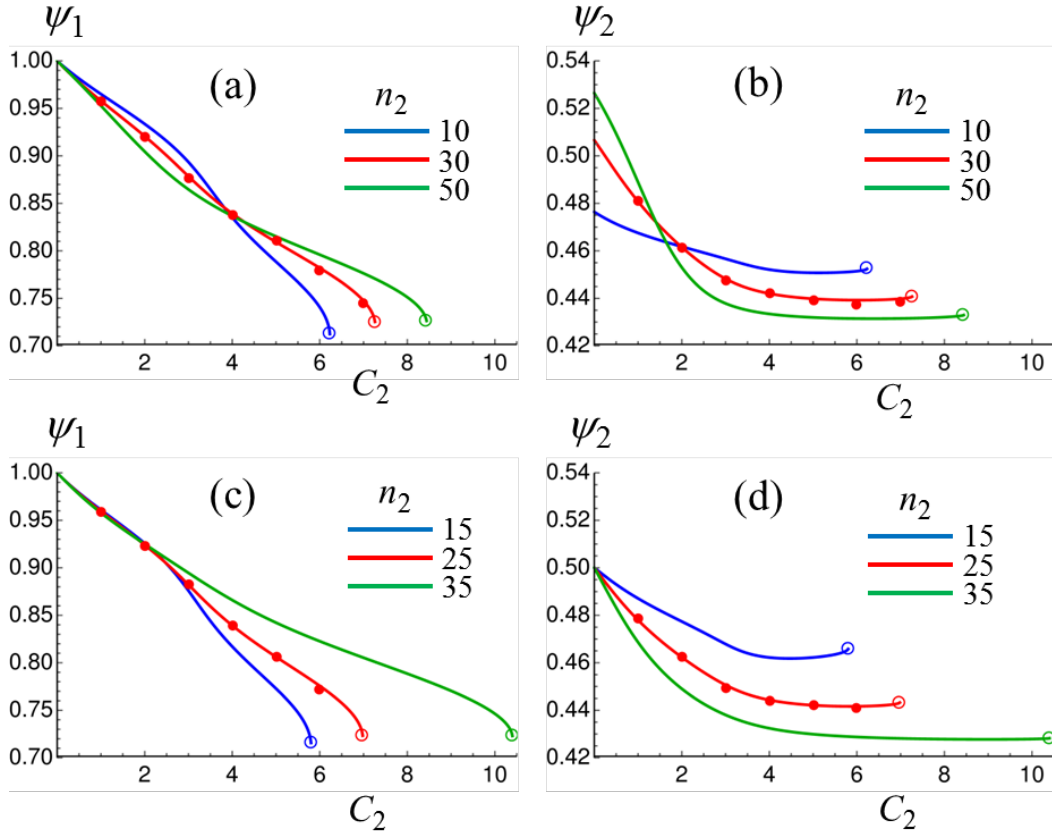


Figure 6.4 Plots of final stable state ψ_1 and ψ_2 against C_2 at $n_2 = 10, 30$, and 50 represented in colors shown in plot legend. (a)(b): fixed $n_1 = 25$ (c)(d): $n_1 = 50 - n_2$. The filled disk marks denote the stable state values obtained by the numerical simulations using the phase model, Eq. (6-11). The circle marks at the end of each curve indicate the boundary of the synchronization domain.

First, we consider the networks at $n_1 = 25$, $n_3 = 50$, and various n_2 , i.e., the number of oscillators in the groups with no capacitors (n_1 and n_3) is constant while the number of oscillators having the capacitors is varied. Figure 6.4ab show the respective phase differences ψ_1 and ψ_2 as functions of the capacitance C_2 at $n_2 = 10, 30$, and 50 . The curves in Figure 6.4ab are obtained through numerical solution of Eqs. (6-9) and (6-10), and represent the stable synchronization states, i.e., the real parts of all five eigenvalues of matrix \mathbf{M} , Eq. (6-12), are negative at each point of the curves. Recall that the units in groups 1 and 2 have the same force

polarity ($\varepsilon_1 = \varepsilon_2 = +1$) and oscillate in phase if the group 2 units have no capacitor, so $\psi_1 = 1$ at $C_2 = 0$ as seen in Figure 6.4a. At $C_2 > 0$, the units in groups 1 and 2 oscillate with a phase difference, ψ_1 , which increases with an increase in C_2 until the synchronization mode ceases to exist at some value of C_2 , as marked by the open circles at the ends of each curve in Figure 6.4a. The upper limit of C_2 depends on n_2 , the number of units in group 2, and increases from $C_2 \approx 6$ to 8.5 with an increase in n_2 (see Figure 6.4a).

Simultaneous with splitting the phase of oscillation into two groups in units having the same force polarity, the introduction of the capacitors affects the phase difference between oscillations of the units having the opposite force polarities. Figure 6.4b shows that the value of ψ_2 changes with an increase in C_2 , and that the variation is greater in networks with more units having the capacitor, i.e., at greater n_2 . Note that the effect of capacitors on ψ_2 is weaker than that on ψ_1 . As C_2 increases, the maximal variation of ψ_2 is observed at $n_2 = 50$ and is about 0.1 (Figure 6.4b), whereas the variation of ψ_1 at $n_2 = 50$ is about 0.28 (Figure 6.4a).

The effects of the capacitors on the synchronization in the BZ-PZ networks discussed above were investigated at a variable number of the units that are modified by the capacitors (n_2) and a constant number of the non-modified units (n_1 and n_3). We now consider the three-group networks with the configuration $\{n_i\} = \{50 - n_2, n_2, 50\}$, $\{\varepsilon_i\} = \{+1, +1, -1\}$, $\{C_i\} = \{0, C_2, 0\}$, where n_2 and C_2 are varied but the total number of units having the force polarity $+1$ is fixed, $n_1 + n_2 = 50$, and is equal to that of the units with the force polarity -1 , $n_3 = 50$. For these networks, the phase differences ψ_1 and ψ_2 as functions of C_2 are displayed in the respective Figure 6.4c and 5d for $n_2 = 15, 25$, and 35. Comparison of Figure 6.4ab with Figure 6.4cd

shows that the effect of capacitors on the two networks is qualitatively similar. Figure 6.4cd show that at $C_2 = 0$ (no capacitors), the units having the force polarity $+1$ are synchronized in-phase between themselves, $\psi_1 = 1$, and anti-phase with the units having the force polarity -1 , $\psi_2 = 0.5$. At $C_2 > 0$, the groups 1 and 2 oscillate with a phase difference ψ_1 that increases with an increase in C_2 (Figure 6.4c), and the effect of capacitors on ψ_2 is weaker than that on ψ_1 . The only notable difference in the synchronization behavior of the two types of networks (Figure 6.4a,b versus Figure 6.4c,d) is seen at sufficiently high values of n_2 . Namely, the second network exhibits stable synchronization at the values of the capacitance C_2 exceeding the synchronization domain of the first network (compare the green-colored curves in Figure 6.4c,d with the red-colored curves in Figure 6.4a,b).

Figure 6.4 reveals that the results of the analysis of the stable synchronization modes are in agreement with the numerical solutions of the phase dynamics equations, Eq. (6-8). Specifically, the red points at $n_2 = 30$ in Figure 6.4a,b and at $n_2 = 25$ in Figure 6.4c,d are obtained by solving Eq. (6-8) for ψ_1 and ψ_2 at several values of the capacitance C_2 . The fact that the red points line directly on the red lines indicates the agreement between the phase dynamics calculations and the stability analysis (Eqs. (6-9,10,11)). Thus, Eqs. (6-9,10,11) provide an effective approach to determine the phase differences and stability of synchronization modes exhibited by the BZ-PZ networks for various configurations.

6.2.3 Co-existence of Three-group Synchronization Modes

The synchronization behavior discussed in the previous section exists at $C_2 = 0$ and evolves continuously as C_2 increases. This stable mode of synchronization is characterized by the phase differences ψ_1 and ψ_2 , and our calculations show that the mode is unique at sufficiently low values of C_2 . To demonstrate the latter observation, we plot the solutions of Eqs. (6-9) and (6-10) for the configuration $\{n_\alpha\} = \{25, 25, 50\}$, $\{\varepsilon_\alpha\} = \{+1, +1, -1\}$, $\{C_\alpha\} = \{0, 1, 0\}$ as the lines in coordinates ψ_1 and ψ_2 (Figure 6.5a). The intersections of these two lines correspond to the steady states of the system. Figure 6.5a shows that the system exhibits four steady states, and the displayed streamlines reveal that only one of them, $\psi_1 = 0.96$ and $\psi_2 = 0.48$, is stable (see also Figure 6.4).

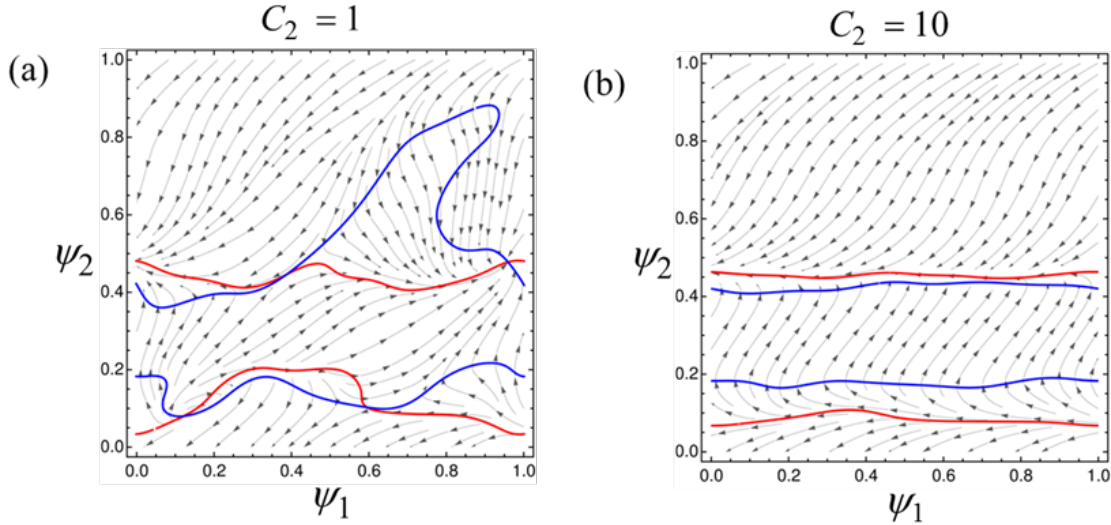


Figure 6.5 Solutions of Eq. (6-9) and (6-10) plotted as the respective blue- and red-colored lines in coordinates ψ_1 and ψ_2 at $\{n_\alpha\} = \{25, 25, 50\}$, $\{\varepsilon_\alpha\} = \{+1, +1, -1\}$, and (a) $C_2 = 1$ and (b) $C_2 = 10$. The streamlines are displayed in grey. At point $\{\psi_1, \psi_2\}$, the streamline shows direction of the vector $\{\Phi_1(\psi_1, \psi_2), \Phi_2(\psi_1, \psi_2)\}$, where Φ_1 and Φ_2 are the left-hand-sides of Eqs. (6-9) and (6-10), respectively.

At high values of C_2 , when the interaction between the units modified with capacitors and the rest of the network is weak, the three-group synchronization does not exist. As an example, Figure 6.5b shows that at $\{n_\alpha\} = \{25, 25, 50\}$, $\{\varepsilon_\alpha\} = \{+1, +1, -1\}$, and $\{C_\alpha\} = \{0, 10, 0\}$, Eqs. (6-9) and (6-10) do not have a solution as the two lines do not intersect.

Further inspection of Eqs. (6-9) and (6-10) at elevated values of C_2 and various $\{n_\alpha\}$ revealed the existence of another stable mode of the three-group synchronization in addition to that discussed above. This new (second) synchronization mode exists only within a narrow interval of C_2 , and the latter interval strongly depends on the number of units having the capacitors, n_2 , as shown in Figure 6.6. Stability of the second mode of synchronization was verified by calculating the eigenvalues as described above; all of the eigenvalues were found to have negative real parts within the mode existence domain.

Figure 6.6a presents the phase differences ψ_1 and ψ_2 for the two stable modes of synchronization obtained by solving Eqs. (6-9) and (6-10) at $\{n_\alpha\} = \{25, 1, 50\}$ and $\{\varepsilon_\alpha\} = \{+1, +1, -1\}$, i.e., when only one BZ-PZ unit contains a capacitor. The solid lines correspond to the stable synchronization mode, which exists at $C_2 = 0$ and evolves continuously with an increase in C_2 until the maximal value of $C_2 \approx 6$ is reached, then the mode disappears. The second synchronization mode, which is shown by the dashed lines, exists only within the interval of capacitance $5 < C_2 < 6.6$ (Figure 6.6a). Note that the domains of the two modes of synchronization overlap, i.e., they co-exist within a certain interval of capacitance ($5 < C_2 < 6$).

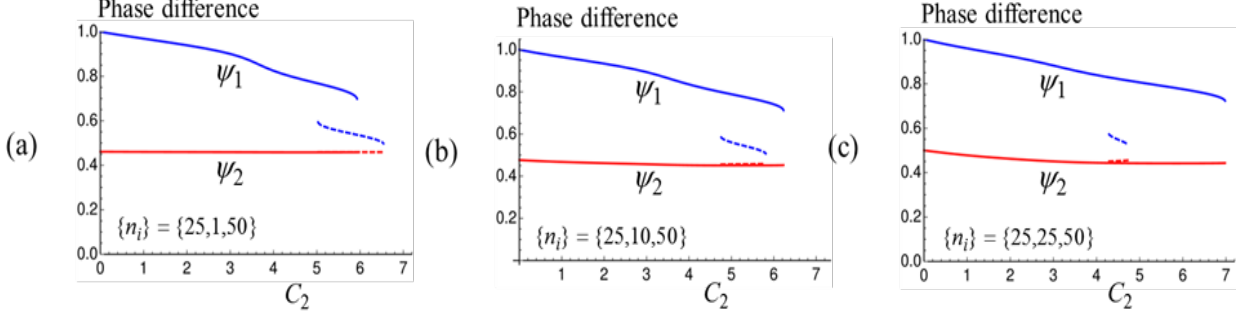


Figure 6.6 The two co-existing stable modes of synchronization in the three-group system with the number of the BZ-PZ units containing the capacitors (a) $n_2 = 1$, (b) $n_2 = 10$, and (c) $n_2 = 25$. The first mode (solid lines) is typically found when Eq. (6-8) is solved under random initial conditions. The second mode (dashed lines) is found when the initial conditions for Eq. (6-8) are chosen in the vicinity of the synchronization state **Figure 6.7**.

Adding more BZ-PZ units with capacitors to the system reduces the interval of C_2 where the second mode of synchronization exists. The latter behavior is shown in Figure 6.6b and c for $n_2 = 10$ and 25, respectively. Figure 6.6b and c also show that the second mode domain (dashed lines) is now located within the first mode domain (solid lines).

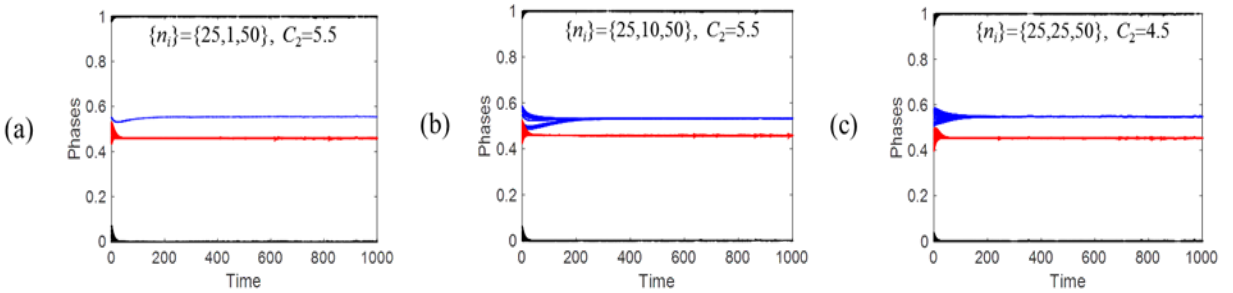


Figure 6.7 Evolution of the three-group system towards the second mode of synchronization as obtained by solving Eq. (6-8) with the initial conditions corresponding to the synchronization state perturbed by adding a random phase shift within $[-0.1, 0.1]$. As in **Figure 6.6**, the number of the BZ-PZ units containing the capacitors (a) $n_2 = 1$, (b) $n_2 = 10$, and (c) $n_2 = 25$.

We confirmed that the second stable mode of synchronization found by solving the steady state equations, Eqs. (6-9) and (6-10), could also be obtained by solving the phase

dynamics equations, Eq. (6-8). Specifically, we took ψ_1 and ψ_2 for the second mode obtained from the steady state equations, and solved Eq. (6-8) using $0, \psi_1, \psi_2$ with added random noise (within $[-0.1, 0.1]$) as the initial conditions for units in the respective groups 1, 2, 3. Figure 6.7a-c show the phase dynamics for the same network configurations as in Figure 6.6a-c, respectively, at the values C_2 indicated in the individual figures. It is seen in Figure 6.7 that the considered systems evolve towards the stable state of synchronization with the final phase differences corresponding to the second mode.

6.2.4 The Rate of Synchronization

Besides the phase differences, the synchronization modes are also characterized by the rate of convergence of an initial state of the network to the final stable steady state (rate of synchronization). We begin the analysis of the effects of the configuration of the BZ-PZ network on the rate of synchronization by considering the situation when the initial state is only slightly different from the steady state. In this case, the rate of synchronization can be estimated using the eigenvalues calculated in the course of the stability analysis, Eq. (6-13), because the value $T_k = |\text{Re}(\lambda_k)|^{-1}$ is the relaxation time of the relaxation mode k , $k = 1, 2, \dots, 5$.

Figure 6.8 shows the relaxation times T_k as functions of the capacitance C_2 for the three-group networks with the configuration $\{n_\alpha\} = \{25, n_2, 50\}$, $\{\varepsilon_\alpha\} = \{+1, +1, -1\}$, and $\{C_\alpha\} = \{0, C_2, 0\}$ at $n_2 = 1, 10$, and 25 . In order to calculate T_k , we used Eq. (6-13) and the phase differences ψ_1 and ψ_2 as functions of C_2 presented in Figure 6.6. Figure 6.8 indicates that with an increase in the capacitance C_2 starting from $C_2 = 0$, the two relaxation times, $k = 2$

(solid red) and 4 (solid green), increase drastically, whereas other relaxation times ($k = 1, 3, 5$) exhibit very weak or no dependence on C_2 . Hence, the introduction of the capacitors into the system slows down the relaxation of the network towards the state of synchronization.

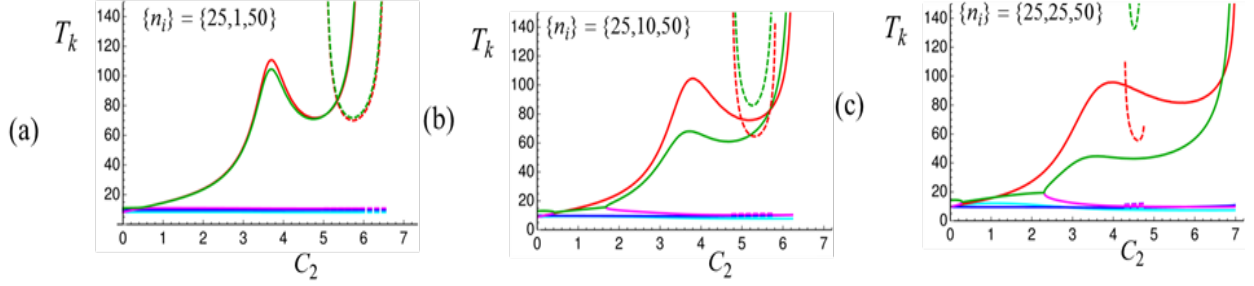


Figure 6.8 The relaxation times T_k , $k = 1, 2, \dots, 5$, as functions of the capacitance C_2 for the three-group networks with the number of BZ-PZ units containing the capacitors (a) $n_2 = 1$, (b) $n_2 = 10$, and (c) $n_2 = 25$. The solid and dashed lines mark the two modes of synchronization. The line colors label the relaxation modes: $\{T_k\} = \{\text{cyan, red, blue, green, magenta}\}$.

The increase in the relaxation times T_2 (solid red) and T_4 (solid green) with an increase in C_2 is not monotonic as seen in Figure 6.8. Namely, these two largest relaxation times exhibit local maxima, which are more pronounced at fewer numbers of the BZ-PZ units having the capacitors. Note also that T_2 and T_4 are very close to each other at $n_2 = 1$ (Figure 6.8a) and $T_2 > T_4$ if several units contain the capacitors (Figure 6.8b and c).

It was demonstrated in the previous section that the networks containing capacitors might have two co-existing synchronization modes. In Figure 6.8, the dashed lines show the relaxation times for the second synchronization mode, which exists only within specific intervals of the capacitance C_2 . Similar to the first synchronization mode, the relaxation times T_2 (dashed red) and T_4 (dashed green) are greater than other relaxation times, $k = 1, 3, 5$. As functions of C_2 , T_2

and T_4 for the second synchronization mode have a minimum in the middle of the interval of C_2 where it exists, and increase close to the ends of the interval. Finally, unlike the first mode, the relaxation time T_4 is greater than T_2 for the second mode (see the green- and red-colored dashed lines in Figure 6.8).

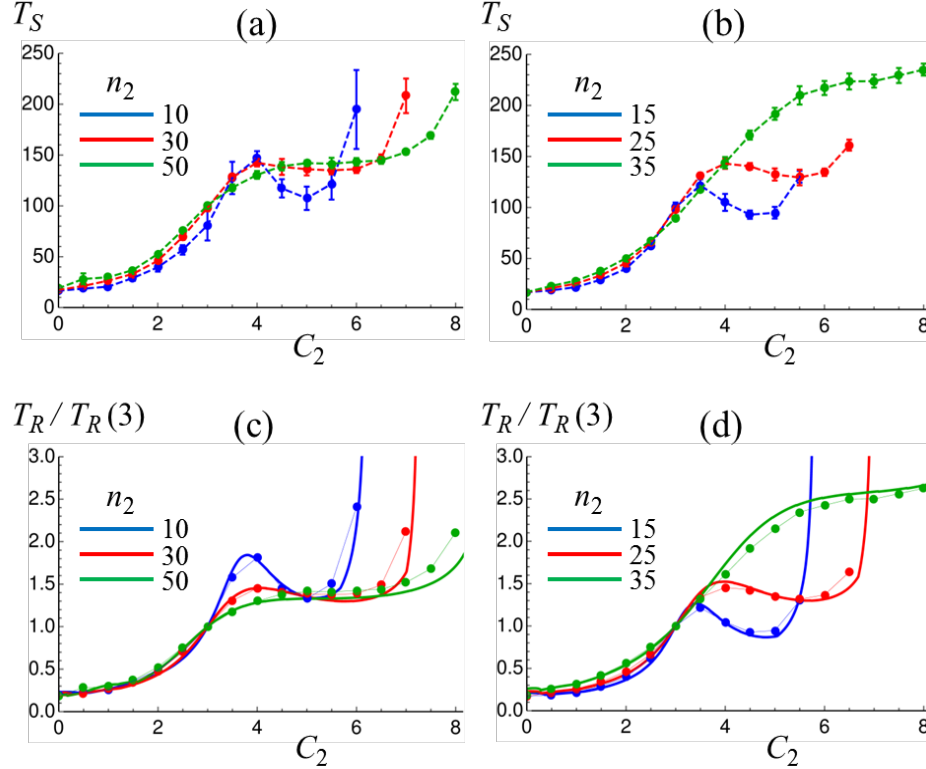


Figure 6.9 The times of synchronization as functions of C_2 obtained by simulations of the three-group networks with the configuration (a) $\{n_\alpha\} = \{25, n_2, 50\}$, (b) $\{n_\alpha\} = \{50 - n_2, n_2, 50\}$. In all cases, $\{\varepsilon_\alpha\} = \{+1, +1, -1\}$, $\{C_\alpha\} = \{0, C_2, 0\}$. (c) and (d): The normalized relaxation times (lines) and synchronization times (symbols) for the same network configurations as in (a) and (b), respectively.

The characterization of the rate of synchronization based on calculating the eigenvalues is, strictly speaking, applicable only to the case of small deviations from a known state of synchronization. The more practical but computationally expensive way to probe the

synchronization behavior of a network of coupled oscillators is to run multiple simulations of the phase dynamics starting from random initial phases. The network is said to be synchronized if the phases of all oscillators (calculated relative to that of some reference unit) evolve to the state where they change only within a narrow range; the width of this range is taken 0.02 in our studies. The time to converge to a state of synchronization, T_S , is taken as the measure of the rate of synchronization.

We applied the above computational procedure to determine the synchronization time, T_S , for the three-group networks discussed in Section IIIB. Namely, we varied the number of the BZ-PZ units that contain the capacitors, n_2 , in the configurations $\{n_\alpha\} = \{25, n_2, 50\}$ and $\{n_\alpha\} = \{50 - n_2, n_2, 50\}$ with the distributions of force polarities $\{\varepsilon_\alpha\} = \{+1, +1, -1\}$ and that of capacitors $\{C_\alpha\} = \{0, C_2, 0\}$. For each network configuration, we performed 100 simulations starting from the random initial phases, and the averaged results are plotted for the two types of networks in the respective Figure 6.9a and b. It is important to note that the simulations according to the applied procedure detected only the mode of synchronization presented in Figure 6.4 and did not detect the synchronization mode presented in Figure 6.6 by the dashed lines.

Figure 6.9a and b show that the synchronization time, T_S , increases tremendously with an increase in capacitance C_2 , and that the latter increase is not monotonic in the networks having fewer units modified with the capacitors. It is remarkable that T_S depends on the capacitance C_2 in a qualitatively similar manner as the relaxation times T_2 and T_4 plotted with the solid lines in Figure 6.8. Furthermore, we demonstrated that after a proper normalization, a quantitative similarity could be established between T_S and the results of linear stability

analysis. For this purpose, we defined the relaxation time as the maximal T_k , $T_R = \max(\{T_k\})$, and normalized both T_S and T_R by their respective values at $C_2 = 3$. As shown in Figure 6.9c and d, after the normalization, the data on T_S presented in the respective Figure 6.9a and b are in a qualitative agreement with the relaxation times, T_R . Therefore, the linear stability analysis could be used to assess the rate of synchronization. Note that the choice of C_2 for normalization is quite arbitrary. It is only required that at the chosen C_2 , some T_k is distinctively greater than all other.

6.2.5 States of Partial Synchronization

We discussed above how the introduction of capacitors affects the existence and properties of the states of perfect synchronization, when all the BZ-PZ units oscillate with some phase differences, which do not change with time. We showed that an increase in the capacitance weakens the interactions between the units with and without capacitors, so the state of perfect synchronization does not exist if the capacitance is greater than the threshold value specific for the network configuration.

Here, we briefly discuss the phase dynamics in the BZ-PZ networks with no the perfect synchronization. For this purpose, we first consider the network configuration $\{n_\alpha\} = \{25, 25, 50\}$, $\{\varepsilon_\alpha\} = \{+1, +1, -1\}$, and $\{C_\alpha\} = \{0, C_2, 0\}$ at $C_2 = 10$. As shown in Figure 6.5b, the perfect synchronization does not take place in this system since the steady state equations, Eqs. (6-9) and (6-10), do not have a solution. Instead, the phase dynamics of this network converges to the state of partial synchronization. Figure 6.10a shows the phase dynamics obtained from a single run of simulations starting from the random phases. In this figure, all phases are shown relative to the

phase of the oscillator with $i=1$, i.e., the values $\varphi_i(t) - \varphi_1(t)$ are plotted with $2 \leq i \leq 50$. It is seen in Figure 6.10a that the oscillators belonging to group 1 (black lines) and group 3 (red lines) are synchronized with the phase difference of about 0.5, whereas the units containing the capacitors (group 2, blue lines) are desynchronized from the latter two groups. The blue-colored lines in Figure 6.10a have a negative slope meaning that the phases of the group 2 units progressively lag behind that of groups 1 and 3.

The phase dynamics pattern shown in Figure 6.10a is not the only one observed in this network. Under some realizations of the random initial conditions, the BZ-PZ units in group 3 (force polarity -1 , no capacitors) form two unequal groups of units that are synchronized with a phase difference between themselves as shown by the red-colored lines in Figure 6.10b. As indicated in Figure 6.10b, one of the latter groups contains most of the units with $\varepsilon_i = -1$ (48 in the shown case), and they are synchronized with the group 1 at the phase difference of about 0.5. The second group of contains only a few units with $\varepsilon_i = -1$ (2 in the shown case) and is synchronized with the group 1 at the phase difference of about 0.7.

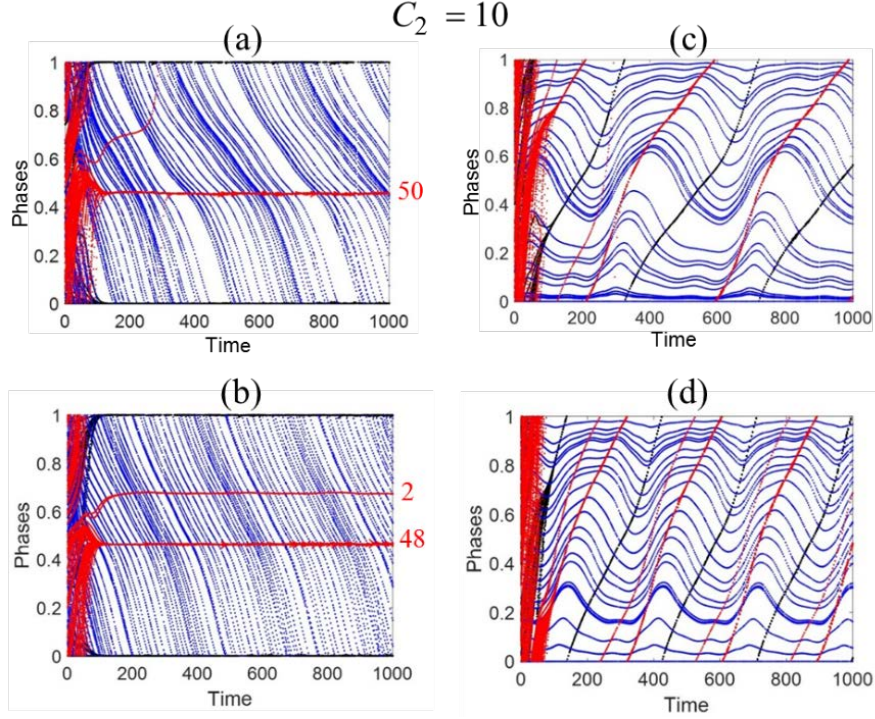


Figure 6.10 The two types of partial synchronization behaviors observed in the numerical simulations of the network with configuration $\{n_\alpha\} = \{25, 25, 50\}$, $\{\varepsilon_\alpha\} = \{+1, +1, -1\}$, and $\{C_\alpha\} = \{0, 10, 0\}$. In (a) and (b), all phases are plotted relative to the unit 1, $\varphi_i(t) - \varphi_1(t)$. In (c) and (d), all phases are plotted relative to the unit 26, $\varphi_i(t) - \varphi_{26}(t)$.

After the initial fast dynamics, the phases of groups 1 and 3 in Figure 6.10a and b (see the black- and red-colored lines) look time-independent at later times. A closer inspection of the presented data revealed that the latter phases exhibit long time periodic deviations. To demonstrate this observation, we plot the phases relative to the phase of oscillator $i = 26$, i.e., relative to the first unit in group 2 (force polarity +1, with capacitors). It is seen in Figure 6.10c and d that the slopes of the black- and red-colored lines, which represent the respective groups 1 and 3, slowly vary. The phases of units in group 2 (blue lines) also exhibit a periodic long-time dynamics. The observed long-time dynamics in the state of partial synchronization is the result

of the interaction between the units with and without capacitors that is sufficiently strong to affect the dynamic patterns.

Finally, at some network configurations, the partial synchronization behavior was observed to co-exist with the state of perfect synchronization. As an example, Figure 6.11 presents one instance of simulations of the phase dynamics for the same network configuration as in Figure 6.10 but with the capacitance $C_2 = 6.5$. Similar to Figure 6.10c and d, Figure 6.11 shows that group 2 (force polarity +1, with capacitors) is desynchronized from groups 1 and 3, and that group 3 (force polarity -1, no capacitors) is split in two. Note that at $C_2 = 6.5$, the state of perfect synchronization also exists in this system as shown in Figure 6.6c.

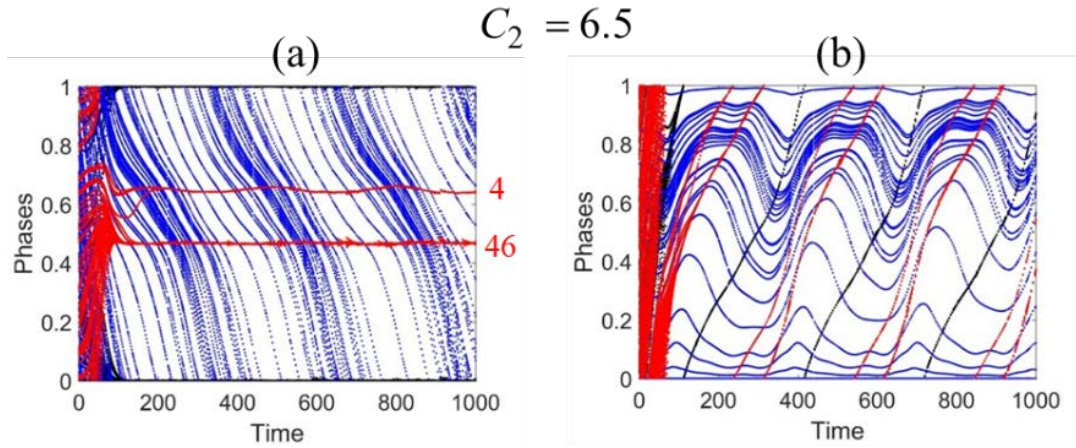


Figure 6.11 The state of partial synchronization observed in the numerical simulations of the network with configuration $\{n_\alpha\} = \{25, 25, 50\}$, $\{\varepsilon_\alpha\} = \{+1, +1, -1\}$, and $\{C_\alpha\} = \{0, 10, 0\}$. In (a) and (b), all phases are plotted relative to the unit 1, $\varphi_i(t) - \varphi_1(t)$. In (c) and (d), all phases are plotted relative to the unit 26, $\varphi_i(t) - \varphi_{26}(t)$.

6.3 PATTERN RECOGNITION

6.3.1 Pattern Matching Experiments on Grayscale Images

Beside the phase relations in the synchronization mode, we are also interested in how fast the synchronization can be achieved in the evolution of a BZ-PZ network. In Section 4.3.1, we define the convergence time of synchronization as the number of time units, $\kappa^{-1}T_0$, needed for the coupled oscillators to reach the stable state of synchronization. Such a measurement can serve as the distance metric to measure the difference between the input pattern represented by the initial phase and the store pattern represented by the final synchronization mode (Section 4.2).

In our previous simulations, we noticed that the BZ-PZ units with capacitor spent longer time to reach the stable state than those units without capacitors. This can be well explained by Eq. (6-11). For an arbitrary BZ-PZ unit, the increase of C_i will decrease z_i and scale down $d\phi_i/dt$ all the time, regardless of the phase and the value of connection function. However, we wonder how the group of units with capacitors influence the overall convergence time of a BZ-PZ network initialized with a given pattern. Hence, we conduct more experiments to explore the impact of capacitors on the convergence time. Figure 6.12 illustrates a pattern matching operation with a BZ-PZ network. We use the four-group network configuration, which is $\{n_1 = n_2 = n_3 = n_4 = 25\}$, $\{\varepsilon_1 = \varepsilon_2 = +1, \varepsilon_3 = \varepsilon_4 = -1\}$, $\{C_1 = 0, C_2 = 4, C_3 = 0, C_4 = 4\}$. Here we assume the store pattern is a 100-pixels four-level grayscale image that consists of four 25-pixel blocks in different color (black, dark gray, white, light gray). The selection of colors is designed for the convenience of demonstration but not limited to these four colors. These blocks are

respectively represented by the four groups of BZ-PZ units (G1, G2, G3, G4) with different parameters. Each unit represents one pixels. Table 6.1 summary the relations between the pixels of store pattern and different groups. As we expect, the network will synchronize into the stable state with the corresponding phase relations we note in the plot of Figure 6.12. The input pattern with two distorted pixels determine the initial phase of each BZ-PZ unit based on the grayscale level of each pixel. The initial phases of color of (G1, G2, G3, G4) is assigned by $(\varphi_1, \varphi_2, \varphi_3, \varphi_4)$, shown in Figure 6.12. The method of introducing distortion into a pattern here is to flip the color of pixels, between black and white, light gray and dark gray. The convergence time of G2 and G3 are respectively 75 and 424, due to these two noise pixels.

Table 6.1 Configuration and Representation of Different Groups of BZ-PZ units

Group	G1	G2	G3	G4
Force Polarity ε	+1	+1	-1	-1
Capacitance C	0	4	0	4
Color represented	Black	Dark Gray	White	Light Gray
Phases (Stable State)	0	0.83	0.5	0.33

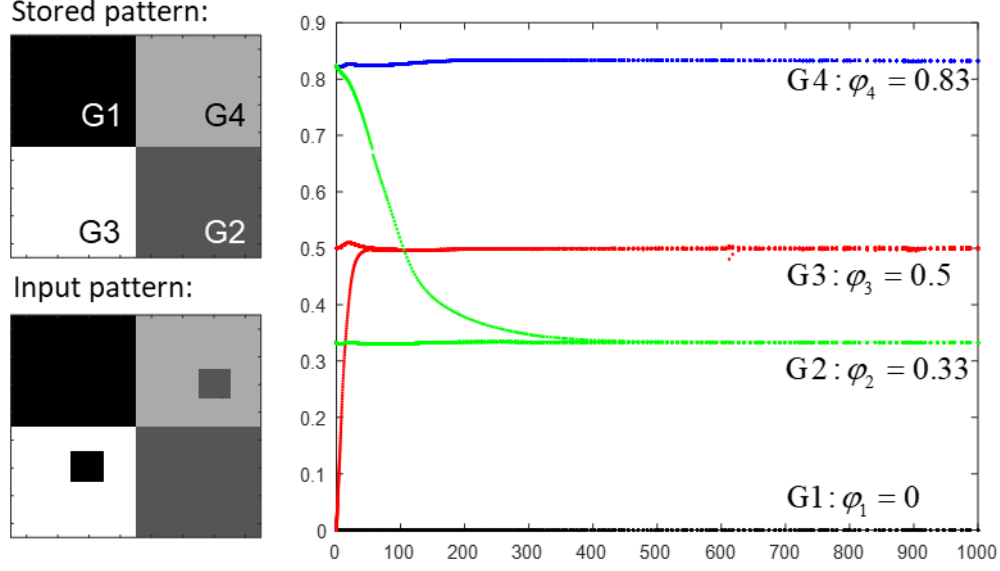


Figure 6.12 Matching operation of grayscale image pattern by using a BZ-PZ network with capacitors.

In order to observe how the group with BZ-PZ units affect the convergence of the group of units without capacitors, we perform the experiment in the following method. In the first experiment, for the store patterns, we only keep the black and white blocks (n_1, n_3) fixed, 30 pixels for each of them, while, the number of pixels in dark and shallow gray blocks (n_2, n_4) gradually increases from 1 to 30 as the extra pixels of the pattern. On the other hand, for the input pattern, we increasingly flip the color of pixels inside the black and white blocks but keep the gray blocks intact. This means there exists intra-group mismatch of initial phases of units in G1 and G3 because of the flipped pixels, while the phases of units in G2 and G4 remain consistent all along the evolution of the system. Thus, only G1 and G3 contribute to the convergence time of network. in this experiment. The increase of the flipped pixels in black and white blocks in the input pattern and the enlarge of gray blocks in the stored pattern are independent, thus generate different combination. We run 100 simulations for each combination

by randomly pick the pixels to be flipped. The average convergence times in these simulations are given in Figure 6.13.

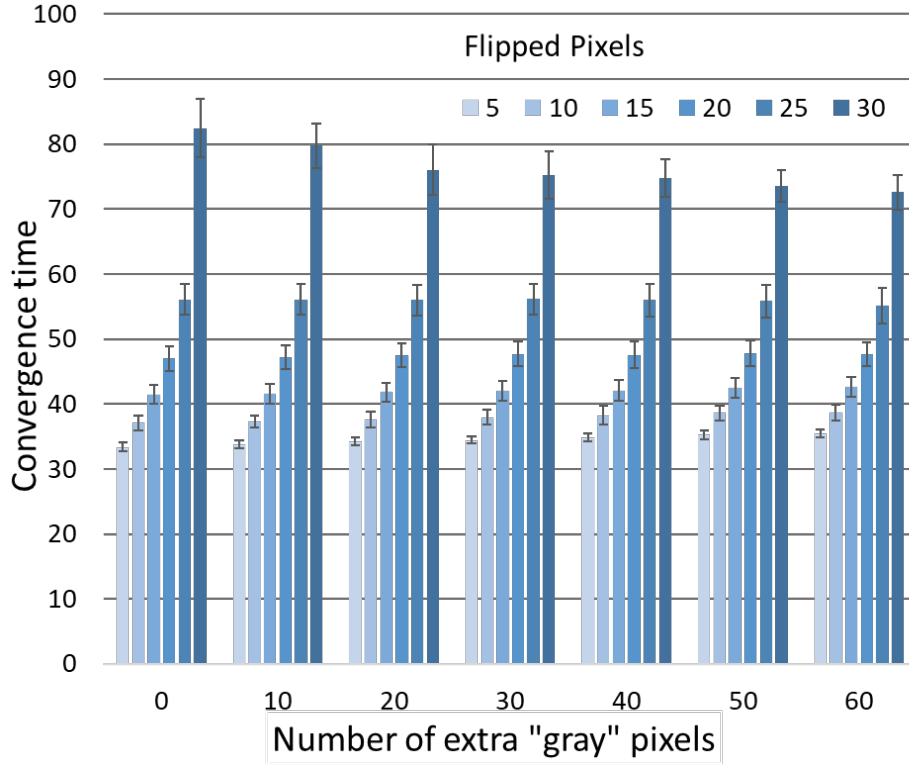


Figure 6.13 Average convergence time of the BZ-PZ network that perform pattern matching on the distorted black/white image pattern with extra gray pixels.

In the second experiment, conversely, we repeat the process of the first experiment but switch the roles of the black/white blocks and the gray blocks. In this situation, the sizes of gray blocks are fixed in the store pattern while the black/white blocks are added as extra pixels. Also, the flipped pixels are selected from the gray blocks in the input pattern. In the BZ-PZ network, convergence time are yielded from G2 and G4, which are the two groups with capacitors. The statistics of convergence times are shown in Figure 6.14.

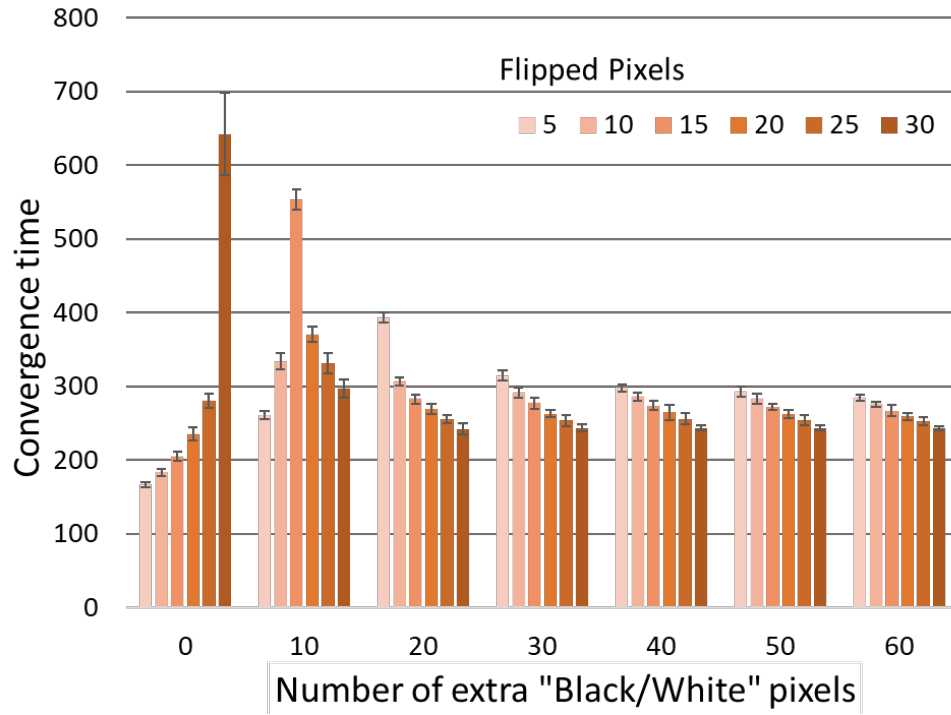


Figure 6.14 Average convergence time of the BZ-PZ network that perform pattern matching on the distorted gray image pattern with extra black white pixels.

From the two experiments above, we first notice that the convergence time of the groups without capacitors (experiment 1) is shorter than the groups with capacitors (experiment 2), as we expected. Additionally, the overall convergence time are both reduced as the total number of unit increases. Second, the increases as the number of flipped pixels increases for the first experiments, due to the difference between input pattern and stored pattern enlarges. This is consistent as we observed in the pattern matching operation of the BZ-PZ network without capacitors. The introduction of more units with capacitors does not influence such a trend. However, in the experiment 2, the increase of flipped pixels in gray image pattern does not result in longer convergence time when enough extra black/white pixels are introduced. This means that the units without capacitors speed up the rate of synchronization of the unit with capacitors. Although these groups of units (G1, G3) keep an intra-group synchronization state, their

common phase still vary during the evolution process of the network. Thus, we can draw the conclusion that when the capacitors are introduced into the BZ-PZ network, the global convergence time of the network cannot be used as the distance metric to measure the difference between input patterns and stored patterns any more.

6.3.2 Pattern Recognition Test on COIL Dataset

Based on our theoretical analysis and numerical simulations in the previous sections, we note that the BZ-PZ oscillator networks with capacitors have complicated dynamical behaviors and rich phases in the synchronization modes that result in the mismatch between the convergence time and the chosen distance measurement of input and output patterns. Therefore, the global convergence time might not be a useful metric used for pattern recognition tasks. In this section, we propose another method to evaluate the distance metric of patterns. We apply our system to a practical recognition task, which is the classification of grayscale images that contain real objects. We still use the similar four-group BZ-PZ networks with capacitors for experiments; however, instead of using the global convergence time, we measure the convergence time of each group of oscillators and use the sum of convergence times as the criterion for classification. As we discussed in Section 6.2, different groups of BZ-PZ oscillators have different configurations and exhibit convergence times that are distinct from each other. Nevertheless, these convergence times depend on the variation between the input pattern and stored pattern. Thus, we conjecture that they might serve as the distance metric of different channels that are similar to the multi-network systems we discussed in Chapter 5.0 Note, however, that such a distance metric is also highly data dependent. To demonstrate the capability of our system in

grayscale image pattern matching, we select an image dataset that contains object categories that are quite different from each other.

The dataset we use is the COIL (Columbia Object Image Library), which contains many grayscale images for different objects in which the background has been discarded (and each picture consists of the smallest square that contains the object) [72]. For each object, 72 pictures are taken from all perspectives by rotating the object 360 degrees. We pick ten objects from the dataset for our pattern recognition task and their images are shown in Figure 6.15.

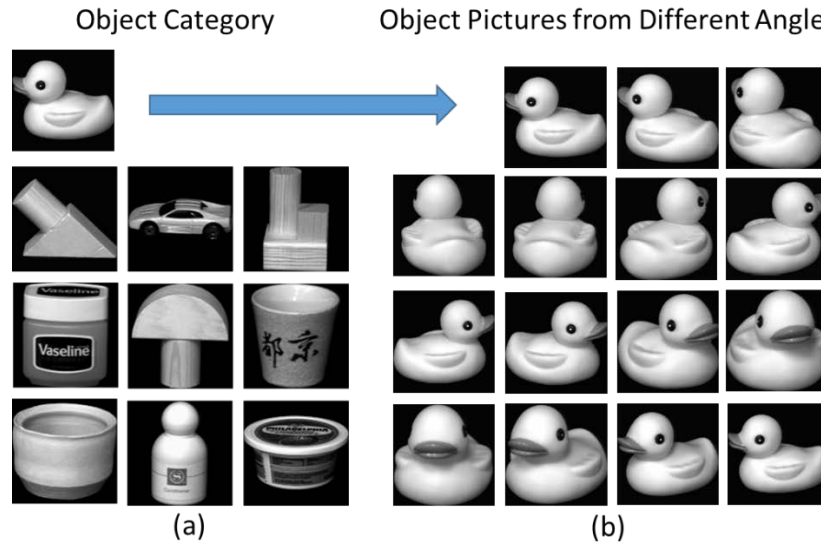


Figure 6.15 Images of objects selected from COIL dataset. (a) Ten object categories; (b) Example images of one object. The grayscale images are pictures taken after every 5-degree rotation. Each object has 72 pictures.

Before the storage or input of the COIL image with BZ-PZ oscillator networks, we perform several steps of preprocessing, shown in Figure 6.16. First, we resize all the images from 128x128 to 40x40. Second, since the synchronization mode of the network we use has four levels of phase, we quantize the grayscale of images from 8-bit (256 scales) to 2-bit (four scales). Finally, we separate an image into four 20x20 quadrant patches and use one BZ-PZ oscillator

network to store one patch. Hence, a pattern matching operation of one image requires four networks. The segmentation of images is performed to reduce the convergence time of the pattern matching process since this allowed us to use multiple small BZ-PZ networks and decrease the number of capacitors in each network. The entire preprocessing steps for pattern storage are illustrated in Figure 6.16.

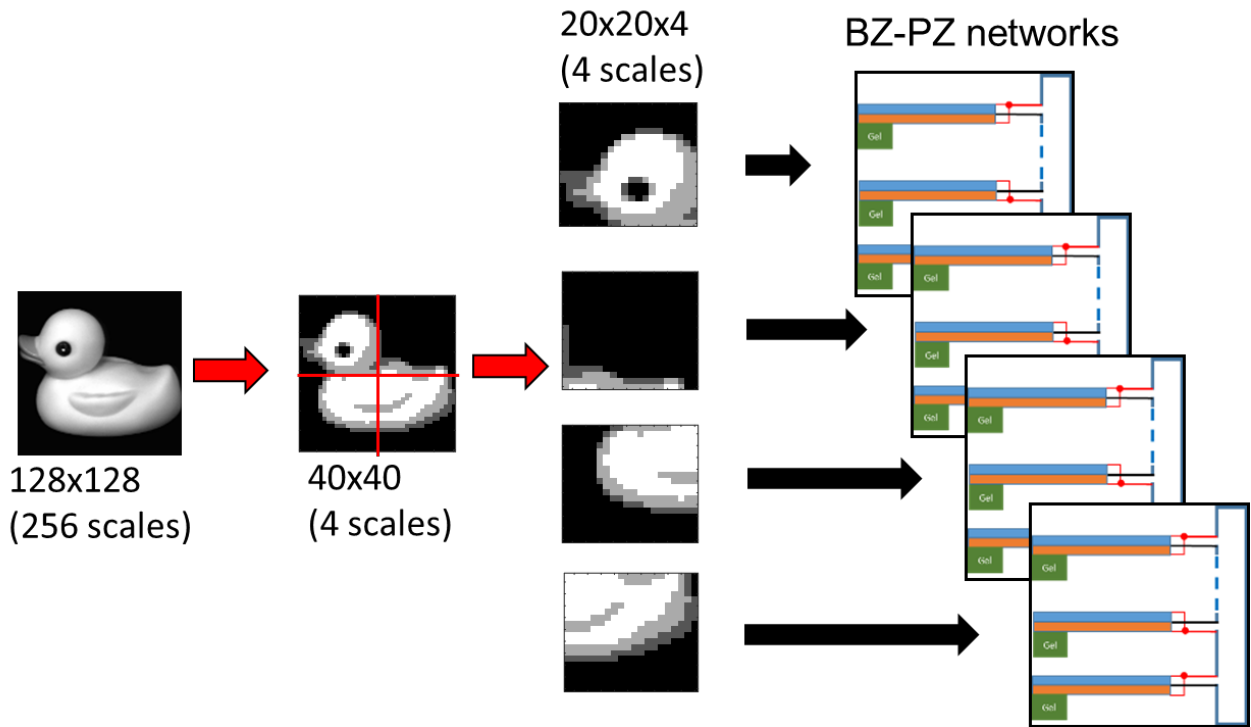


Figure 6.16 The preprocessing stages for pattern storage

For the pattern recognition task, we set the unrotated first image of each object as the stored pattern for one category. As we described above, the stored pattern is segmented into four patches and stored in four independent BZ-PZ networks with the configuration given in Table 6.1, except setting capacitance $C=1$. Therefore, we have ten grayscale image patterns stored in 40 BZ-PZ oscillator networks with 400 units in each network.

In the recognition stage, we use a similar configuration as in Section 4.3.3. For one run of the recognition operation, we select ten images of different categories as the test input pattern and broadcast them to all the networks (Figure 6.17). In other words, each input pattern will be compared to 10 stored patterns and there are a total of 100 pattern-matching operations (10×10) in one run. For these 100 operations, we measure the sum of the convergence times of each one and plot them in a 10×10 color matrix (Figure 6.17). In Figure 6.17, the x-axis is the label of the stored pattern and the y-axis represents the input pattern. Thus, each row of a convergence time matrix gives the degree of match between one input pattern and ten stored patterns equal to the sum of the convergence times in each pattern matching operation, indicated by colors that vary from blue to red. The correct recognition is on the diagonal of the matrix, where the input pattern and stored pattern are the same objects. Meanwhile, the incorrect recognition is labeled by the red triangle, which has the lowest convergence time on the row, but deviates from the diagonal.

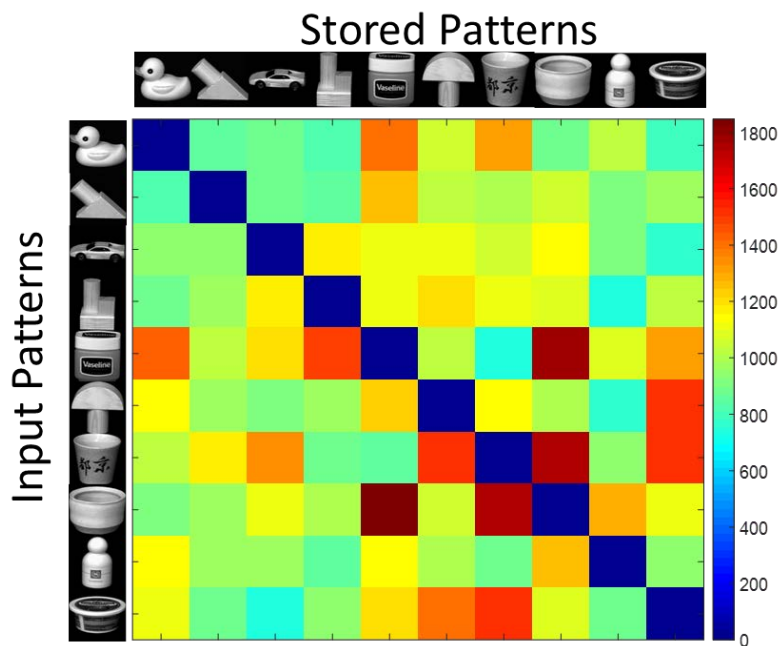


Figure 6.17 The convergence time matrices of pattern matching on COIL dataset.

In the first test, we make the input pattern and the stored patterns precisely the same images. Figure 6.17 illustrates the convergence matrix in such a scenario; the diagonal elements of the convergence time matrix are all zero (dark blue), in contrast to the other elements with a much higher value of convergence time. The results shown in Figure 6.17 indicate that the sum of the convergence times of different oscillator groups can effectively discriminate the stored patterns in this test.

In the following three tests, we select the test images in the same object categories but demonstrate rotations of objects as the input patterns. The rotations of objects are respectively 15° , 25° , 50° in each test. The convergence matrices of these tests are plotted in Figure 6.18(a)(b)(c). We notice that as the variation of pattern (rotation) increases, the values of the non-diagonal elements of each row become closer to the diagonal elements. As the input patterns increasingly differ from the correct template patterns the difficulty of pattern recognition increases and eventually results in errors in the case of the 25° and 50° rotations. This trend is observed through the color distribution in each matrix in Figure 6.18.

The results and observations in this section are similar to the results shown in Figure 4.12 of Section 4.3.3. Thus, we demonstrate that the BZ-PZ networks with capacitors are capable of performing pattern recognition on grayscale images, providing the sum of the convergence times of each oscillator groups as a distance metric.

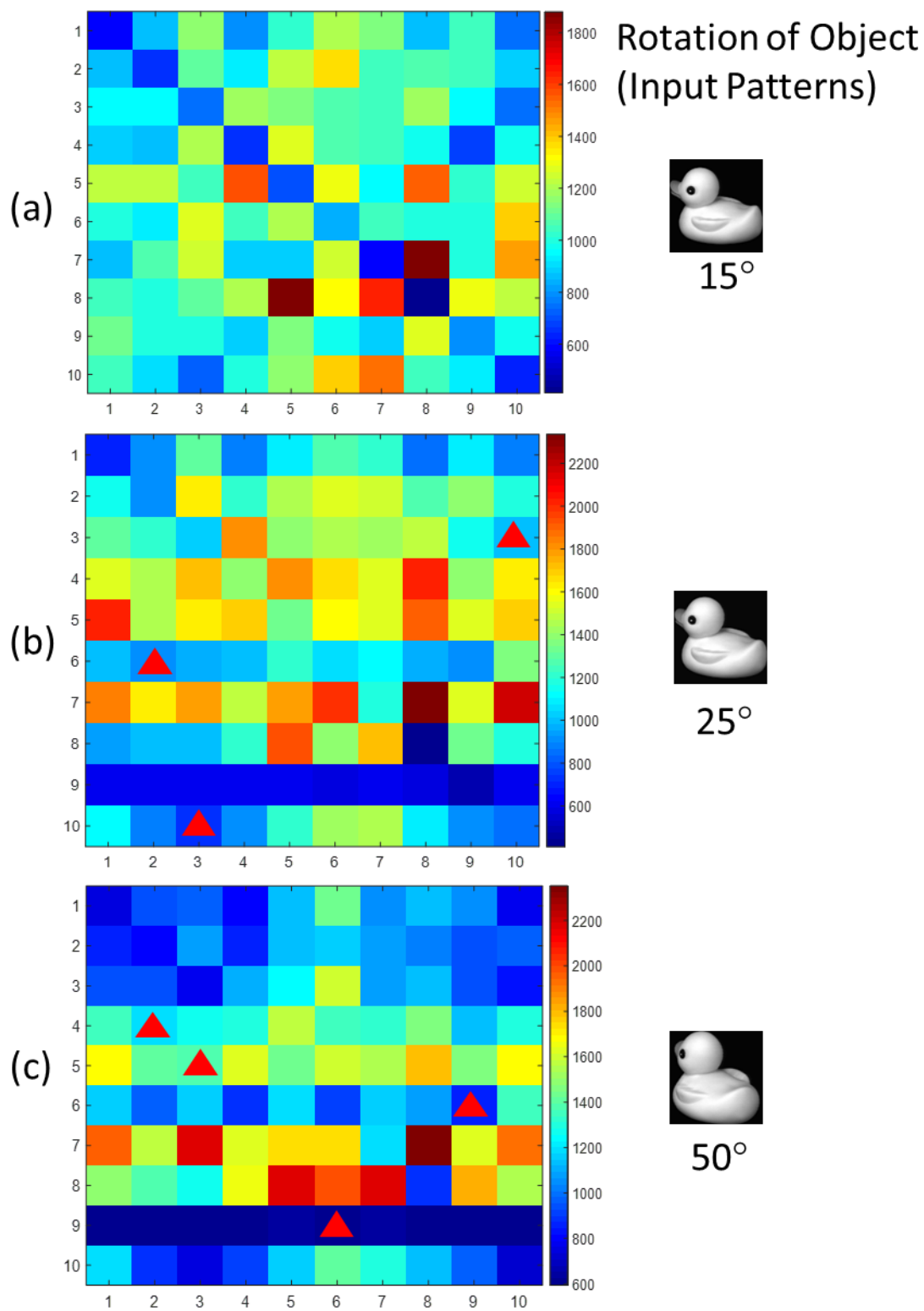


Figure 6.18 The convergence time matrices of pattern matching on COIL dataset with object rotation. Objects are rotated in the input patterns for (a) 15° , (b) 25° , (c) 50° respectively.

6.4 DISCUSSION

Overall, our study in this chapter reveals the rich dynamical behavior that can be achieved by combining responsive materials so that each component can harness the distinctive properties of the other (e.g., the oscillating properties of the BZ gels and the electromechanical properties of the PZ cantilevers) to perform such functions as sensing and actuation. For the BZ-PZ system, the network of interacting materials units can also communicate and achieve synchronization. The modes of synchronization represent a means of coding and storing information in the system. In our previous studies of the BZ-PZ system, the oscillators in the network showed two distinct modes of synchronization. To enrich the level of information that could be stored in the device, we introduced capacitors in parallel to the PZ plates. We focused on capacitors because they are passive units that still enable the system to operate in a relatively self-sustained, autonomous manner (converting chemical energy from the BZ reaction into the mechanical motion in the system). Moreover, by deriving Eq. (7) and (8), we found that the capacitors will lead to a redistribution of charge in the system and alteration of the force acting on the PZ cantilevers. Hence, the capacitors modify the strength of coupling between the oscillators in the network. We hypothesized that the changes in the coupling strength would affect the modes of synchronization and potentially lead to the appearance of additional stable states.

To test the above hypothesis, we formulated the phase dynamics equations to analyze the synchronization modes in this new system, where groups of oscillators encompass the capacitors. With this phase dynamics approach, we varied the number and capacitance of the capacitors in the system and performed detailed studies to analyze the rich dynamical behavior in the system. In particular, through numerical simulation and analytical calculations, we determined the impact of the capacitors on the existence of the synchronization modes, their stability, and the rate of

synchronization within the networks. We validated our conjecture that the introduction of capacitors can split a single mode of synchronization into two distinct modes and thus, augment the information storage capabilities of the device. The extent of level splitting can be significantly enhanced by considering networks that encompass four or more distinct groups (where the capacitors in the different groups can take on different values of capacitance). Hence, the information storage can be significantly enriched with the introduction of more complex configurations.

Importantly, we also showed that the rate of synchronization can be estimated using the eigenvalues calculated in the course of the stability analysis and thereby showed a non-monotonic dependence between the synchronization rate and the value of the capacitance in certain configurations of the network. This non-monotonic dependence hints at the complexity that is inherent in these weakly coupled systems.

More generally, the findings also provide insight into the complex dynamics that can be exhibited by weakly coupled oscillators and how these dynamics can be tuned by tailoring the strength of interaction between the oscillators. Notably, there is an increasing demand for “robotic materials” that harness the intrinsic properties of the materials to perform such functions as sensing, actuation and information storage. Ideally, these robotic materials should be lightweight and compliant so that they could be worn or be readily interfaced with human activities. Hence, it becomes important to design materials systems whose inherent behavior provides a route to the “robotic” activities and to establish means to expand the functionality of these materials.

7.0 CONCLUSION AND FUTURE WORK

In this chapter, we first present a summary of this dissertation and present essential conclusions we can draw from this research. Finally, in the section of future work, we introduce some remaining problems in this area and a few ideas to extend our work.

7.1 SUMMARY

In this dissertation, we propose the new concept of “materials that compute”. We explore this topic by designing and modeling new computing systems based on coupled hybrid material oscillators, which are composed of self-oscillating gels and piezoelectric films. Here, we summarize our work in this dissertation.

In [Chapter 2](#), we provide the theoretical background for this dissertation. We explore the previous work on oscillator-based computing. In particular, we examine the computing paradigm in visual pattern matching. We also briefly discuss oscillator neural networks, which inspired our design in this work. Then we give a short introduction to BZ gels and provide relevant mathematic models.

In [Chapter 3](#), we study the phase models of coupled oscillators that can be used to describe the oscillation behavior and speed up the simulation of oscillator-based systems. We demonstrate three methods to obtain the phase response curve or connection function of coupled

oscillators and use CMOS ring oscillators as examples. Then we simulate three oscillator-based computing paradigms with phase models and show the acceleration in the simulation.

In [Chapter 4](#), we describe the design of our new material computing system in detail, including the hybrid PZ-BZ oscillator and coupled networks of these units. We present a new method for storing patterns in coupled oscillator networks and initialization of input patterns and how the pattern recognition is performed. We provide design guidelines and simulation results that show the system performance and robustness. Finally, we analyze the stability of the synchronization modes and the feasibility of fabricating these devices.

In [Chapter 5](#), we present the architecture of multiple BZ-PZ Networks in parallel and the encoding channels of colored patterns. We discuss how the colored patterns are decomposed in multiple channels and processed by BZ-PZ networks. We use a simple colored pattern to demonstrate the detection of defects in different channels and then apply the proposed system to the detection of defects in colored QR-codes.

In [Chapter 6](#), we propose the BZ-PZ oscillator networks with capacitors. We illustrate the structure of this modified network and derive the dynamical equations for the force acting on the units in the network. Then, we derive the corresponding equations in the phase domain and demonstrate the splitting of phases in the final stable state. By using the phase equation, we find the equilibrium solution for the system and perform linear stability analysis to verify the existence of synchronization modes and the rate of synchronization. We take the BZ-PZ oscillator networks with three groups of configurations as an example and compare the theoretical analysis and numerical simulation. Through the investigation, we found the co-existence of synchronization modes and the states of partial synchronization. Finally, we test the proposed network in the pattern recognition task with COIL, a dataset of grayscale pictures.

7.2 CONCLUSIONS

Based on the research described herein, a set of important conclusions can be drawn:

- Phase models are effective and efficient in predicting the frequency or phase of coupled oscillator systems with small errors compared to the direct simulation of the oscillator model. The key element of the phase model is the phase response curve, or connection function, which represents the intrinsic properties of the coupling between oscillators. Phase models can reduce the computation cost of simulation and are particularly suitable for simulation and analysis for oscillator-based applications, such as pattern matching, segmentation, and convolution.
- BZ-PZ hybrid material system can sense, actuate, communicate, and compute in a self-organized manner. The self-oscillating BZ gel can serve as both actuator and sensor. Its chemo-mechanical oscillation can be sensed and perturbed through the overlaying piezoelectric film. The piezoelectric film serves as an efficient interface for the coupling BZ oscillators and enabling the information processing capabilities of the system. These properties and the feasibility of fabrication make the BZ-PZ oscillator a good candidate for “materials that compute”.
- The oscillation of coupled BZ-PZ oscillators synchronizes either in-phase or anti-phase, depending on the force polarizes. Therefore, a binary pattern can be stored in a BZ-PZ oscillator network by configuring the force polarizes. The synchronization of BZ-PZ units in the oscillator network performs a pattern matching operation.
- The convergence time represents the rate of synchronization and can be used as a distance metric to measure the difference between stored pattern and input patterns. BZ-

PZ oscillator networks can perform a nearest neighbor search by comparing the convergence time and achieve pattern recognition.

- We can process more complicated patterns than binary vectors by utilizing multiple BZ-PZ networks in parallel. This can be achieved through employing a single BZ-PZ network as a distinct “channel” and decomposing patterns into sets of binary vectors.
- Multiple BZ-PZ networks can detect subtle defects in an input pattern relative to a stored image that encompasses information in different features.
- The proposed multi-channel network system can also be applied in cryptography or steganography. For example, the device can be used as an authentication system with a plain code and a multi-level password, or for storing images pattern with hidden information.
- To enrich the level of information that could be stored in the BZ-PZ network, we can introduce capacitors in parallel to the PZ plate of each unit. The modes of synchronization represent a means of coding and storing information in the system. The capacitors modify the strength of coupling between the oscillators in the network and thus, affect the modes of synchronization, resulting in additional stable states.
- In the group of BZ-PZ oscillators with the same force polarity, adding capacitors to some oscillators results in the splitting of final phases and the slowing down of the synchronization. The phases in the final stable state depend on the number of oscillators, force polarity, and capacitance.
- Equilibria in phase equations and linear stability analysis can be used to predict the synchronization modes efficiently and to estimate the rate of synchronization near the stable state.

- It is challenging to locate all the synchronization modes in a BZ-PZ network that consists of multiple groups of oscillators with various configurations due to the complex dynamic behaviors, co-existence of synchronization modes, and the states of partial synchronization. It is equally challenging to determine the rate of synchronization from an arbitrary initial state; this leads to the failure of measuring distance between stored patterns and input patterns by using the convergence time.
- Although the global convergence time is no longer useful for evaluation of the degree of match (DoM), according to our experiments, the sum of convergence times of each oscillator group still works for the grayscale pattern recognition task on the COIL dataset.

7.3 FUTURE WORK

My PhD research work in “materials that compute” is an initial exploration of this new topic.

Here, we list some thoughts and ideas for potential future work:

- The current design of BZ-PZ networks with capacitors is relatively inefficient in pattern recognition task, mostly because the introduction of capacitors increases the convergence time and complicates the dynamical behavior of systems. One direction of future innovation could be new computing paradigms that do not rely on the convergence time as the critical measurement. We may borrow ideas and concepts from other unconventional computing paradigms, such as brain-inspired/neuromorphic computing. For example, using spikes as the information representation, instead of phases. In such a case, we might design an event-based computing system built on our materials.

- Another idea for future work would be introducing stochastic properties into our computing system, considering that most of our applications are focused on computer vision and machine learning. One potential direction is the stochastic oscillation of the BZ gel and the other direction would be the signal sensed from the external environment, which randomly perturbs the oscillation of gels.
- Based on the ideas we mention, we can introduce light as a new input to our system since the gel is sensitive to the light in oscillating frequency. Using light as the input or controlling signal, we can change the way of information processing in our system. However, this might require new structures of BZ-PZ networks.
- Designing new interfaces between BZ-PZ units is another possible future work. The current design of the connection is merely two electrodes that convey both input and output signals. It has the advantage of energy conservation, but also limits the new design of network architectures. Namely, for synchronization, the BZ-PZ oscillators can only be connected in a serial loop. Designing circuits of new interfaces may address this problem and might a route for providing external power for signal amplification.

BIBLIOGRAPHY

- [1] “Emerging research devices, international technology roadmap for semiconductors”, (2011) <http://www.itrs.net>.
- [2] G.I. Bourianoff, J.E. Brewer, R.K. Cavin, J.A. Hutchby and V.V. Zhirnov, “Boolean logic and alternative information-processing devices”, *Computer*, Vol. 41, Issue 5, pp. 38- 46, May 2008.
- [3] M. A. McEvoy, N. Correll, “Materials that couple sensing, actuation, computation, and communication”, *Science* 347, 1261689 (2015).
- [4] Y. Fang, C. N. Gnegy, T. Shitbata, D. Dash, D. M. Chiarulli, S. P. Levitan, “Non-Boolean associative processing: Circuits, system architecture, and algorithms”, *IEEE J. Explor. Solid State Comput. Devices Circuits* 1, 95–103 (2015).
- [5] R. Yoshida, T. Takahashi, T. Yamaguchi, and H. Ichijo, “Self-oscillating gel”, *J. Am. Chem. Soc.*, 118 (1996) 5133-5135.
- [6] R. Yoshida, "Self-oscillating gels driven by the belousov–zhabotinsky reaction as novel smart materials", *Advanced Materials* 22, no. 31 (2010): 3463-3483.
- [7] V.V. Yashin, S. Suzuki, R. Yoshida, and A.C. Balazs, “Controlling the Dynamic Behavior of Heterogeneous Self-Oscillating Gels”, *Journal of Materials Chemistry*, 22 (2012) 13625-13636.
- [8] V.V. Yashin, A.C. Balazs, “Pattern Formation and Shape Changes in Self-Oscillating Polymer Gels”, *Science*, 314 (2006) 798-801.
- [9] O. Kuksenok, P. Dayal, A. Bhattacharya, V.V. Yashin, D. Deb, I.C. Chen, K.J. Van Vliet, and A.C. Balazs. "Chemo-responsive, self-oscillating gels that undergo biomimetic communication." *Chemical Society Reviews* 42, no. 17 (2013): 7257-7277.
- [10] P. Dayal, O. Kuksenok, and A.C. Balazs, “Using Light to Guide the Self-Sustained Motion of Active Gels”, *Langmuir*, 25 (2009) 4298-4301.
- [11] V.V. Yashin, O. Kuksenok, P. Dayal, and A.C. Balazs, "Mechano-chemical waves in reactive gels", *Reports on Progress in Physics*, 75 (2012) 066601, 40 pages.

- [12] V.V. Yashin, K.J. Van Vliet, A.C. Balazs, “Controlling Chemical Oscillations in Heterogeneous BZ Gels via Mechanical Strain”, *Physical Review E*, 79 (2009) 046214, 12 pages.
- [13] Y. Fang, V. V. Yashin and A. C. Balazs, “Pattern recognition with ‘materials that compute.’” *Science Advance* **2**, 1601114 (2016).
- [14] Y. Fang, V. V. Yashin, B. B. Jennings, D. M. Chiarulli, Steven P. Levitan, “A simplified phase model for simulation of oscillator based computing systems,” *ACM Journal on Emerging Technologies in Computing Systems*, Vol. 13, Issue. 2, Article No. 14, (Dec, 2016).
- [15] Y. Fang, V. V. Yashin, S. J. Dickerson, A. C. Balazs, “Detecting Spatial Defects in Colored Patterns with Coupled Self-Oscillating Gels”, *Journal of Applied Physics*, 2018 (accepted)
- [16] Y. Fang, V. V. Yashin, S. J. Dickerson, A. C. Balazs, “Tuning the Synchronization of a Network of Weakly Coupled Self-oscillating Gels via Capacitors”, *Chaos*. 2018 (accepted)
- [17] J.A. Hutchby, R. Cavin, V. Zhirnov, J. E. Brewer, and G. Bourianoff, “Emerging nanoscale memory and logic devices: a critical assessment,” *Computer*, vol. 41, no. 5, pp. 28–32, 2008.
- [18] M.R. Pufall, W. H. Rippard, S. Kaka, T. J. Silva, S. E. Russek, “Frequency modulation of spin-transfer oscillators”, *Applied Physics Letters*, 86(8), 082506-082506, 2005.
- [19] N. Locatelli, V. Cros and J. Grollier, “Spin-torque building blocks” *Nature materials*, 13(1), 11-20 (2014).
- [20] D. Weinstein, and S.A Bhawe, “The resonant body transistor”. *Nano letters*, 10(4), 1233-1237, (2010).
- [21] N. Shukla, “Synchronized charge oscillations in correlated electron systems”. *Scientific Reports*, (2014), 3.
- [22] M. J. Cotter, Y. Fang, S. P. Levitan, D. M. Chiarulli, and V. Narayanan, (2014, July). “Computational architectures based on coupled oscillators.” In *VLSI (ISVLSI), 2014 IEEE Computer Society Annual Symposium on* (pp. 130-135).
- [23] F. C. Hoppensteadt, and E.M.Izhikevich, (2000). Pattern recognition via synchronization in phase-locked loop neural networks. *IEEE Transactions on Neural Networks*, 11(3), 733-738.
- [24] D. Wang, and D. Termani, (1995). Locally excitatory globally inhibitory oscillator networks. *IEEE Transactions on Neural Networks*, 6(1), 283-286.

- [25] S. P. Levitan, Y. Fang, D. H. Dash, T. Shibata, D. E. Nikonov and G. I. Bourianoff, (2012). "Non-Boolean associative architectures based on nano-oscillators." In *Cellular Nanoscale Networks and Their Applications (CNNA)*, 13th IEEE International Workshop on (pp. 1-6).
- [26] T. Shibata, R. Zhang, S.P. Levitan, D. E. Nikonov and G. I. Bourianoff, (2012). "CMOS supporting circuitries for nano-oscillator-based associative memories." In *Cellular Nanoscale Networks and Their Applications (CNNA)*, 13th IEEE International Workshop on (pp. 1-5).
- [27] G. Csaba, and W. Porod, (2013). "Computational Study of Spin-Torque Oscillator Interactions for Non-Boolean Computing Applications." *IEEE Transactions on Magnetics*, 49(7), 4447-4451.
- [28] M. Kabir, and M. Stan, (2014, June). "Computing with Hybrid CMOS/STO Circuits." In *Proceedings of the The 51st Annual Design Automation Conference on Design Automation Conference* (pp. 1-6). ACM.
- [29] A. Krizhevsky, I. Sutskever, and G. E. Hinton, (2012). "Imagenet classification with deep convolutional neural networks." In *Advances in neural information processing systems* (pp. 1097-1105).
- [30] T. Serre, and M. Riesenhuber, "Realistic modeling of simple and complex cell tuning in the HMAX model, and implications for invariant object recognition in cortex," CBCL Paper 239/AI Memo 2003-017, Massachusetts Inst. of Technology, Cambridge, 2003.
- [31] F.C Hoppensteadt and E.M. Izhikevich, "Synaptic Organizations and Dynamical Properties of Weakly Connected Neural Oscillators: I. Analysis of Canonical Model," *Biological Cybernetics*, Vol. 75 pp. 129-135, 1996
- [32] J.J. Hopfield, "Neural Networks and Physical Systems with Emergent Collective Computational Abilities", *Proceedings of the National Academy of Sciences*, Vol. 79, No.8, pp. 2553-2558, 1982.
- [33] C.C. Foster, *Content Addressable Parallel Processors*, New York, NY: John Wiley & Sons, Inc. 1976.
- [34] D. Fan, S. Maji, K. Yogendra, M. Sharad, and R. Roy, (2015). "Injection-Locked Spin Hall-Induced Coupled-Oscillators for Energy Efficient Associative Computing." *IEEE Transactions on Nanotechnology*, 14(6), 1083-1093.
- [35] X. Lai, and J. Roychowdhury, (2005, September). "Analytical equations for predicting injection locking in LC and ring oscillators." In *Custom Integrated Circuits Conference, 2005. Proceedings of the IEEE 2005* (pp. 461-464).
- [36] D. M. Chiarulli, B. B. Jennings, Y. Fang, A. Seel, S. P. Levitan, (2015, July.) "A computational primitive for convolution based on coupled oscillator arrays". *2015 IEEE Computer Society Annual Symposium on VLSI (ISVLSI'15)*.

- [37] Y. Fang, M. J. Cotter, D. M. Chiarulli and S. P. Levitan, (2014, July). "Image segmentation using frequency locking of coupled oscillators." In *Cellular Nanoscale Networks and their Applications (CNNA), 2014 14th International Workshop on* (pp. 1-2). IEEE.
- [38] B. P. Belousov, "A periodic reaction and its mechanism." In *Collection of short papers on radiation medicine for 1958*, Med. Publ., Moscow, 1959.
- [39] A. M. Zhabotinsky, "Periodical oxidation of malonic acid in solution (a study of the Belousov reaction kinetics)", *Biofizika*, 9, 306-11 (1964).
- [40] R. J. Field, and M. Burger, *Oscillations and traveling waves in chemical systems*. Wiley, New York, 1985.
- [41] I. R. Epstein, and J. A. Pojman, *An introduction to nonlinear chemical dynamics: oscillations, waves, patterns, and chaos*. Oxford University Press, New York, 1998.
- [42] J. J. Tyson, P. C. Fife, "Target patterns in a realistic model of the Belousov–Zhabotinsky reaction." *J. Chem. Phys.* 73, 2224–2237 (1980).
- [43] V.V. Yashin, O. Kuksenok, A.C. Balazs, "Computational design of active, self-reinforcing gels", *J. Phys. Chem. B* 114, 6316–6322 (2010).
- [44] S. Hirotsu, "Softening of bulk modulus and negative Poisson's ratio near the volume phase transition of polymer gels". *J. Chem. Phys.* 94, 3949–3957 (1991).
- [45] A. Demir, A. Mehrotra & J. Roychowdhury, J. "Phase noise in oscillators: A unifying theory and numerical methods for characterization." *IEEE Transactions on Circuits and Systems I: Fundamental Theory and Applications*, 47(5), 655-674. (2000)
- [46] E.M. Izhikevich, Synchronization, Chapter 10 in *Dynamical systems in neuroscience*. MIT press. (2007).
- [47] Y. Kuramoto, *Chemical oscillations, waves, and turbulence*. Springer (1984).
- [48] A. T. Winfree, "Biological rhythms and the behavior of populations of coupled oscillators." *Journal of theoretical biology*, 16(1), 15-42 (1967).
- [49] P. Maffezzoni, "Synchronization analysis of two weakly coupled oscillators through a PPV macromodel.", *IEEE Transactions on Circuits and Systems I: Regular Papers* 57.3: 654-663 (2010).
- [50] Y. LeCun, L. Bottou, Y. Bengio, and P. Haffner. "Gradient-based learning applied to document recognition." *Proceedings of the IEEE*, 86(11):2278-2324, (1998).
- [51] V.V. Yashin, S.P. Levitan, A.C. Balazs, "Achieving synchronization with active hybrid materials: Coupling self-oscillating gels and piezoelectric films" *Sci. Rep.* 5, 11577 (2015).

- [52] I. C. Chen, O. Kuksenok, V. V. Yashin, A. C. Balazs, K. J. Van Vliet, "Mechanical resuscitation of chemical oscillations in Belousov-Zhabotinsky gels." *Adv. Funct. Mater.* 22, 2535–2541 (2012).
- [53] V. V. Yashin, A. C. Balazs, "Modeling polymer gels exhibiting self-oscillations due to the Belousov-Zhabotinsky reaction." *Macromolecules* 39, 2024–2026 (2006).
- [54] V. V. Yashin, A. C. Balazs, "Theoretical and computational modeling of self-oscillating polymer gels." *J. Chem. Phys.* 126, 124707 (2007).
- [55] V. V. Yashin, S. P. Levitan, A. C. Balazs, "Modeling the entrainment of self-oscillating gels to periodic mechanical deformation." *Chaos* 25, 064302 (2015).
- [56] R. G. Ballas, *Piezoelectric Multilayer Beam Bending Actuators: Static and Dynamic Behavior and Aspects of Sensor Integration*. Springer, New York, (2007).
- [57] A. Preumont, *Mechatronics: Dynamics of Electromechanical and Piezoelectric Systems* Springer, Dordrecht, (2006).
- [58] S. H. Baek, et. al. "Giant piezoelectricity on Si for hyperactive MEMS." *Science* 334, 958–961 (2011).
- [59] S.-H. Baek, M. S. Rzchowski, V. A. Aksyuk, "Giant piezoelectricity in PMN-PT thin films: Beyond PZT." *MRS Bull.* 37, 1022–1029 (2012).
- [60] M. Ma, L. Guo, D. G. Anderson, R. Langer, "Bio-inspired polymer composite actuator and generator driven by water gradients". *Science* 339, 186–189 (2013).
- [61] C. Dagdeviren, et al. "Conformal piezoelectric systems for clinical and experimental characterization of soft tissue biomechanics." *Nat. Mater.* 14, 728–736 (2015).
- [62] C. Poynton, *Digital video and HD: Algorithms and Interfaces*. (Elsevier, Amsterdam, 2012).
- [63] A. Grillo, A. Lentini, M. Querini and G. F. Italiano, "High capacity colored two dimensional codes." *Proceeding of 2010 International Multiconference on Computer Science and Information Technology*, 709 (2010).
- [64] D. Vodenicarevic, N. Locatelli, J. Grollier and D. Querlioz, "Synchronization detection in networks of coupled oscillators for pattern recognition." In *Proceeding of IEEE 30th International Joint Conference on Neural Networks*, pp. 2015-2022. (2016, July).
- [65] C. K. Volos, et al. "Memristor: A new concept in synchronization of coupled neuromorphic circuits." *Journal of Engineering Science and Technology Review*, 8(2), 157-173, (2015).
- [66] M. A. Lynch, "Long-term potentiation and memory." *Physiological reviews*, 84(1), 87-136, (2004).

- [67] S. Haykin, *A Comprehensive Foundation: Neural Networks*, (Princeton Hall, NJ, 2007).
- [68] Y. LeCun, Y. Bengio, and G. Hinton, Deep Learning, *Nature* **521**, 436 (2015).
- [69] G. Indiveri, et al. "Neuromorphic silicon neuron circuits." *Frontiers in Neuroscience* **5**, 73 (2011).
- [70] S. P. Adhikari, et al. "Memristor bridge synapse-based neural network and its learning." *IEEE Transactions on Neural Networks and Learning Systems* **23**, 1426 (2012).
- [71] D. Kuzum, R. G. Jeyasingh, B. Lee, and H. S. P. Wong. "Nanoelectronic programmable synapses based on phase change materials for brain-inspired computing", *Nano Letters* **12**, 2179 (2011).
- [72] S. A. Nene, S. K. Nayar and H. Murase, "Columbia Object Image Library (COIL-20)," Technical Report CUCS-005-96, February 1996.